

ALMA MATER STUDIORUM UNIVERSITA' DI BOLOGNA

Dottorato di Ricerca in Scienze Biomediche e Neuromotorie
XXXIV Ciclo

Settore concorsuale: 05/E3 BIOCHIMICA CLINICA E BIOLOGIA
MOLECOLARE CLINICA

Settore scientifico disciplinare: BIO/12 BIOCHIMICA CLINICA E BIOLOGIA
MOLECOLARE CLINICA

**Development of functional MRI protocols in the
study of neurodegenerative diseases:
MRI study in patients with REM sleep behavior
disorder, idiopathic Parkinson's disease and
multisystem atrophy.**

Presentata da: Fiorina Bartiromo

Coordinatore Dottorato: Prof Matilde Follo

Supervisore: Prof Caterina Tonon

Esame finale: anno 2022

Contents

Introduction	6
1. The role of iron in brain ageing and neurodegenerative disorders ...	10
1.1 Peripheral iron uptake: regulation of cellular iron.....	10
1.2 Brain iron metabolism.....	11
2. MRI Biomarkers of neurodegeneration	
2.1 Quantitative Susceptibility Mapping	14
2.1.1 Magnetic Susceptibility χ in the Human Body	15
2.1.2 Magnetic Field and Tissue Magnetization	15
2.1.3 Magnetic Materials: dia-, para- and ferromagnetic conditions.....	18
2.1.4 Susceptibility Sources in Human Body.....	21
2.2 Susceptibility and MRI Imaging	25
2.2.1 Gradient Echo Sequence	26

2.2.2 Raw Data Processing: Phase Unwrapping and Background Field Removal	27
2.2.3 Susceptibility Weighted Imaging: SWI	28
2.2.5 Quantitative Susceptibility Mapping: QSM.....	31
2.3 Susceptibility Mapping and Clinical Applications	32
2.3.1 Iron in neurons: neurodegenerative diseases	33
2.3.2 Iron in macrophages and microglia: neuroinflammatory diseases	36
2.3.3 Iron in red blood cells: oxygen consumption and hemorrhage	38
2.3.4 Iron deficiency	40
2.3.5 Calcium	40
3 Study Introduction	41
4 Materials and Methods	
4.1 Study Population.....	45
4.2 Clinical Evaluation.....	46
4.3 Brain MR Image Protocol Acquisition.....	47
4.4 QSM: Sequence processing and optimisation	47
4.4.1 Nigrosome-1 Detection in Quantitative Susceptibility Mapping: Contrast Optimization with 64-channel Coil	51
4.5 Image analysis	51

4.5.1 Qualitative visual assessment	51
4.5.2 Quantitative imaging processing and analysis.....	59
4.6 Statistical analysis.....	63
5. Results	
5.1 Study population.....	65
5.2 Conventional imaging evaluation results.....	67
5.3 Qualitative brain imaging results.....	68
5.3.1 Imaging features of nigrosome score between three groups	68
5.3.2 SWI putaminal analysis.....	72
5.4 Quantitative brain imaging results.....	76
5.5 Clinical correlations	82
6. Discussion	84
7. Future directions	91

Abstract

In the central nervous system, **iron** in several proteins is involved in many important processes such as oxygen transportation, oxidative phosphorylation, mitochondrial respiration, myelin production, and the synthesis and metabolism of neurotransmitters. Abnormal iron homeostasis can induce cellular damage through hydroxyl radical production, which can cause the oxidation and modification of lipids, proteins, carbohydrates, and DNA, lead to neurotoxicity. Any mismatch in the demand and regional temporal distribution of iron may result in neurological and/or mental dysfunction.

On the other hand, increased levels of iron are harmful and iron accumulations are typical hallmarks of brain ageing and several **neurodegenerative disorders** particularly PD.

Numerous studies on post mortem tissue report on an increased amount of total iron in the substantia nigra in patients with PD also supported by large body of in vivo findings from Magnetic Resonance Imaging (MRI) studies. The importance and approaches for in vivo brain iron assessment using multiparametric MRI is increased over last years.

Quantitative **MRI** may provide useful **biomarkers** for brain integrity assessment in iron-related neurodegeneration. Particularly, a prominent change in iron-sensitive T2* MRI contrast within the sub areas of the SN overlapping with nigrosome 1 were shown to be a hallmark of Parkinson's Disease with high diagnostic accuracy. Moreover, differential diagnosis between Parkinson's Disease (**PD**) and atypical parkinsonian syndromes (**APS**) remains challenging, mainly in the early phases of the disease. Advanced brain MR imaging enables to detect the pathological changes of nigral and extranigral structures at the onset of clinical manifestations and their during the course of the disease.

The Nigrosome-1 (N1) is a substructure of the healthy Substantia Nigra pars compacta enriched by dopaminergic neurons; their loss in Parkinson's disease and atypical parkinsonian syndromes is related to the **iron** accumulation. N1 changes are supportive MR biomarkers for diagnosis of these neurodegenerative disorders, but its detection is hard with conventional sequences, also using high field (3T) scanner. Quantitative susceptibility mapping (**QSM**), an iron-sensitive technique, enables the direct detection of Neurodegeneration.

Key words: iron, MRI, biomarkers, QSM, PD, APS.

INTRODUCTION

Iron is essential for a proper CNS function. It plays an important role as cofactor of numerous enzymes and is involved in ATP production, myelination and synthesis of DNA, RNA, proteins, and neurotransmitters. In the brain, variations in iron levels correlate with its structural integrity (Jahanshad N et al., 2013), and there is no other organ but the CNS that is in such a constant need for readily available iron (Thompson KJ et al., 2001). Any mismatch in the demand and regional temporal distribution of iron may result in neurological and/or mental dysfunction. Iron deficiency, for example, is a well-established cause for impaired motor and cognitive development (Bastian TW et al., 2016, Pivina L et al. 2019, Shafir T et al. 2008, Wurzinger B et al. 2016). On the other hand, increased levels of iron are harmful and iron accumulations are typical hallmarks of brain ageing and several neurodegenerative disorders particularly Parkinson Disease (PD) (Gerlach M et al., 2010, Hare D et al., 2013, Jomova K. et al., 2010, Qian Z et al. 1997, Ward RJ et al. 2014). Various factors have been suggested to account for increased iron accumulation in the SN (substantia nigra) of patients with PD such as, for example, dysfunction of the blood–brain barrier, altered cellular iron transport, an increased pro-inflammatory state and mutations in genes of iron transport, storage and binding (Borie C et al. 2002, Conde JR et al. 2006, Mastroberardino PG et al. 2009). However, all these processes will differently affect different cell populations. Still, the local accumulation of iron in the SN in patients with PD remains a controversial issue. Numerous studies on post mortem tissue report on an increased amount of total iron in the SN (Dexter DT et al.1989, Earle KM et al. 1968, Mann VM et al. 1994) also supported by large body of in vivo findings from Magnetic Resonance Imaging (MRI) (Blazejewska AI et al. 2013, Cosottini M et al. 2014, Kwon DH et al 2012). The increasing importance and approaches for in vivo brain iron assessment using multiparametric MRI is featured in a review by Moeller et al. (Möller H et al 2019). Quantitative MRI may in fact provide useful biomarkers for brain integrity

assessment in iron-related neurodegeneration. Particularly, a prominent change in iron-sensitive T2* MRI contrast within the sub areas of the SN overlapping with nigrosome 1 were shown to be a hallmark of PD with high diagnostic power. Other studies failed to detect any disease-related differences ([Gałazka-Friedman J et al. 1996](#), [Loeffler DA et al. 1995](#), [Uitti RJ et al. 1989](#)). Of note, more in depth knowledge on whether changes in intracellular iron pools preferentially affect neurons or glial cells is limited by the lack of quantitative analytical techniques with sufficient spatial resolution for in-situ cellular analysis. To glean much needed information about cellular and subcellular compartmentalisation of iron in health and disease, some authors developed ([Reinert T et al. 2011](#)) a powerful analytical approach, which we call immuno-*micro particle induced X-ray emission* (μ PIXE). It allows for quantitative determining the iron concentrations of specific target structures in tissue sections with a spatial resolution in the μm range. To this end, quantitative element mapping using μ PIXE was combined with nickel-enhanced immunocytochemical detection of cell type-specific antigens to specifically allocate element-related signals to specific cell types. In the present study ([Friedrich I et al 2021](#)), this method was applied to quantify the cell specific iron concentrations in SN nigrosome 1 in controls and PD: 8 cases of healthy controls (HC; mean age 66 ± 16 years) and from patients who died with a clinical diagnosis of idiopathic Parkinson's disease: 8 cases of PD; mean age 75 ± 7 years). The definite diagnosis of PD has been verified by neuro-histopathological examination based on a severe loss of neuromelanin containing neurons in the nigrosome 1 of the SNc (pars compact of substantia nigra), the presence of extra-neuronal melanin and Lewy bodies. Although the appearance of Lewy bodies might be also a hallmark of dementia with Lewy bodies (DLB), a detailed synopsis of neuropathological examination and clinical presentation of the PD individuals included in experimental analysis allowed a strict inclusion of patients that suffered exclusively from PD and did not present any comorbidity of dementia. The study showed a distinct patterns of iron accumulation were

observed across different cell populations. In the control (Co) SNc, oligodendroglial and astroglial cells hold the highest cellular iron concentration whereas in PD, the iron concentration was increased in most cell types in the substantia nigra except for astroglial cells and ferritin-positive oligodendroglial cells. While iron levels in astroglial cells remain unchanged, ferritin in oligodendroglial cells seems to be depleted by almost half in PD. The highest cellular iron levels in neurons were located in the cytoplasm, which might increase the source of non-chelated Fe^{3+} , implicating a critical increase in the labile iron pool. Indeed, neuromelanin is characterised by a significantly higher loading of iron including most probable the occupancy of low-affinity iron binding sites. Quantitative trace element analysis is essential to characterise iron in oxidative processes in PD. The quantification of iron provides deeper insights into changes of cellular iron levels in PD and may contribute to the research in iron-chelating disease-modifying drugs. Iron is definitively one of the key factors that most likely plays a major role in PD although its precise pathogenic role is not fully understood (Zecca L et al. 2004). While several studies report on increased levels of total iron in the SN (Dexter DT et al. 1989, Hirsch EC et al 1991, Jellinger K et al 1990, Riederer P et al 1989), others did not (Gałazka-Friedman J et al 1996, Loeffler DA et al 1995, Uitti RJ et al. 1989).

This increase of total nigral iron reflecting an interference of multiple pathological processes including inflammation, myelination, perturbed iron uptake as well as vascular damage, each affecting distinct cell populations. Of note, both in the normal brain and in PD, the major iron pool (about 80%) is localised in glial cells. But, as mentioned above, in the **normal brain**, the population of ferritin-stained **oligodendroglial** cells contain most iron, followed by astroglial cells, microglial cells and another population of Olig2-stained oligodendroglial cells. This pattern is inverted in PD. While the iron content of astroglial cells in **PD** remained unchanged, microglial cells showed an iron accumulation of about one quarter (26%) and Olig2-stained oligodendroglial cells by about 150%. Descriptions of

the physiological and pathophysiological role of iron need to take into account the iron redistribution between neurons and glial cells. The increase of iron in **microglial** cells has been attributed to its activation (Berg D et al. 2001, Thomsen MS et al. 2015, Zhang X et al. 2006) and might be due to phagocytosis of neuromelanin fragments (Wilms H et al 2003, Zecca L. et al 2003, Zhang W et al 2011, Zucca FA et al 2017) and increased iron uptake via transferrin-receptor (Ward RJ, Zucca FA et al 2014) or nontransferrin bound iron (Bishop GM, et al 2011). Accordingly, to these morphological observations, microglial cells have the potential to degrade and solubilize neuromelanin that is released by degenerating neurons (Zhang W et al 2011). As a result of this, soluble iron is generated that could be internalized in other surrounding cells, promoting neuroinflammation and ultimately neurodegeneration. Extracellular neuromelanin goes hand in hand with a release of proinflammatory and toxic molecules that can maintain neuroinflammation as well as degeneration processes (Zhang W et al 2011). The iron pool of activated microglial cells may again be subject to cellular redistribution. Apoptosis of exhausted and damaged microglial cells might result in release of iron into the extracellular space (Colton CA, Gilbert DL 1987). and circulating toxic iron may be taken by neurons or glial cells through transferrin-dependent and independent mechanisms (Belaidi AA et al. 2016, Bishop GM et al. 2011, Reinert A et al. 2019, Thomsen MS et al. 2015). Activation of microglial cells, furthermore, is associated by a reduction of ferritin-*de-novo*-synthesis and H-ferritin levels, which may occur as a consequence of increased oxidative stress (Mehlhase J et al. 2005, Mehlhase J et al. 2006).

1.The role of iron in brain ageing and neurodegenerative disorders

In the CNS, **iron** in several proteins is involved in many important processes such as oxygen transportation, oxidative phosphorylation, mitochondrial respiration, myelin production, and the synthesis and metabolism of neurotransmitters. Abnormal iron homoeostasis can induce cellular damage through hydroxyl radical production, which can cause the oxidation and modification of lipids, proteins, carbohydrates, and DNA, lead to neurotoxicity.

During ageing, different iron complexes accumulate in brain regions associated with motor and cognitive impairment. In various neurodegenerative diseases, such as Alzheimer's disease and Parkinson's disease, changes in iron homoeostasis result in altered cellular iron distribution and accumulation.

Whether the iron accumulation noted in neurodegenerative diseases is a primary event or a secondary effect is unclear. Ageing is the major risk factor for neurodegeneration. Age-related accumulation of iron might be an important factor that contributes to neurodegenerative processes.

The development of diagnostic and therapeutic strategies involves the use of disease-specific animal models and non-invasive imaging approaches, such as MRI dysregulation of iron homeostasis in prevalent neurodegenerative diseases, including Alzheimer's disease, Parkinson's disease, and multiple sclerosis; the use of iron chelators as a potential therapy for the aforementioned diseases and disorders.

1.1 Peripheral iron uptake: regulation of cellular iron

Iron released as ferrous iron from specific cells (ie, macrophages, hepatocytes) via ferroportin, is oxidised by ferroxidase ceruloplasmin and binds to circulating apo-

transferrin ; in enterocytes, hephaestin, a ceruloplasmin analogue, might have this role ([Andrews NC et al. 2007](#)). Peripheral cellular iron uptake mainly involves endocytosis of the diferric transferrin–transferrin receptor 1 (TFR1) complex; iron is then transported from the endosomes into the cell cytoplasm via the divalent metal ion transporter 1 (DMT1). Iron enters the intracellular labile iron pool, some of which will be incorporated into iron-containing proteins (for energy metabolism in mitochondria) or stored in ferritin, as a soluble, non-toxic, bioavailable form; additionally, iron can be stored in lysosomes within ferritin and haemosiderin ([Hentze MW et al. 2010](#); [Mills E et al. 2010](#)).

Ferroportin transports ferrous iron out of some cells (eg, hepatocytes, enterocytes, macrophages) to bind circulating apo-transferrin after oxidation by ceruloplasmin or other related ferroxidases, such as hephaestin. Circulating hepcidin regulates systemic iron homeostasis by interacting with ferroportin when iron is abundant, which results in ferroportin internalisation and degradation, thereby blocking iron exportation from cells. As circulating iron concentrations decrease, hepcidin synthesis decreases, and iron exportation by ferroportin resumes

1.2 Brain iron metabolism

Iron enters the endothelial cells of the blood–brain barrier as a low molecular weight complex, or via transferrin receptor-1 mediated endocytosis of transferrin, or independently as non-transferrin-bound iron ([Moos T et al. 2000](#); [Moos T et al 2007](#), [KeY, Qian ZM. 2007](#), [Leitner DF et al. 2012](#)). Transferrin receptors line the lumen of the brain and bind circulating diferric–transferrin facilitating iron uptake into brain vascular endothelial cells via receptor–mediated endocytosis. Whether there is a DMT1–ferroportin-independent pathway to release ferric iron or diferric-transferrin by exocytosis of recycling endosomes is unclear (vesicular export pathway, left side in brain vascular endothelial cells). Transferrin is synthesised

by the choroid plexus or oligodendrocytes so that any ferric iron released from the abluminal side of the endothelial cells can form complexes with transferrin or alternatively low molecular weight molecules (eg, ascorbate, citrate, or ATP) to form nontransferrin-bound iron. Citrate and ATP can be released from the astrocytes. Whether there is a DMT1–ferroportin dependent (fig 1) (non-vesicular export, right side in brain vascular endothelial cells) pathway to release ferrous iron, which would be rapidly converted to ferric iron via ceruloplasmin in the abluminal membranes, is also unknown. The glycosyl-phosphatidyl-inositol-anchored form of ceruloplasmin is highly expressed by astrocytes in the mammalian CNS and is physically associated with ferroportin.¹⁷ Astrocytes are ideally positioned to take up iron from the circulation and distribute it to other cells in the CNS. Astrocytes have the iron influx and efflux mechanisms needed for cell-to-cell transport of iron. DMT1 is expressed by astrocytes and probably mediates iron influx into these glial cells (Jeong SY et al 2003).

Iron can be stored as ferritin in astrocytes and exported by a mechanism that involves ferroportin and ceruloplasmin (Dringen R et al 2007). Oligodendrocytes might take up iron via the ferritin receptor Tim-2, or non-transferrin-bound iron via DMT1, or other non-vesicular iron import mechanisms. Neurons and microglia can influx iron via transferrin– transferrin receptor mediated uptake and efflux iron via ferroportin. IRPs (1 and 2), DMT1, and –IRE DMT1 (non-IRE form of DMT1 protein) are expressed mostly by astrocytes. Increased iron regulatory proteins expression might lead to increased expression of the +IRE form of DMT1 (Huang E. et al. 2006).

The role of hepcidin in orchestrating the regulation of egress from cells via ferroportin in different brain cells remains unclear. Neuron axons are wrapped with the myelin sheath, which is made of oligodendrocytes in an iron-dependent manner. Microglia form an association with neurons via CD200/CD200R to maintain the quiescent state. Microglia might take up iron via transferrin receptor and release iron via ferroportin.

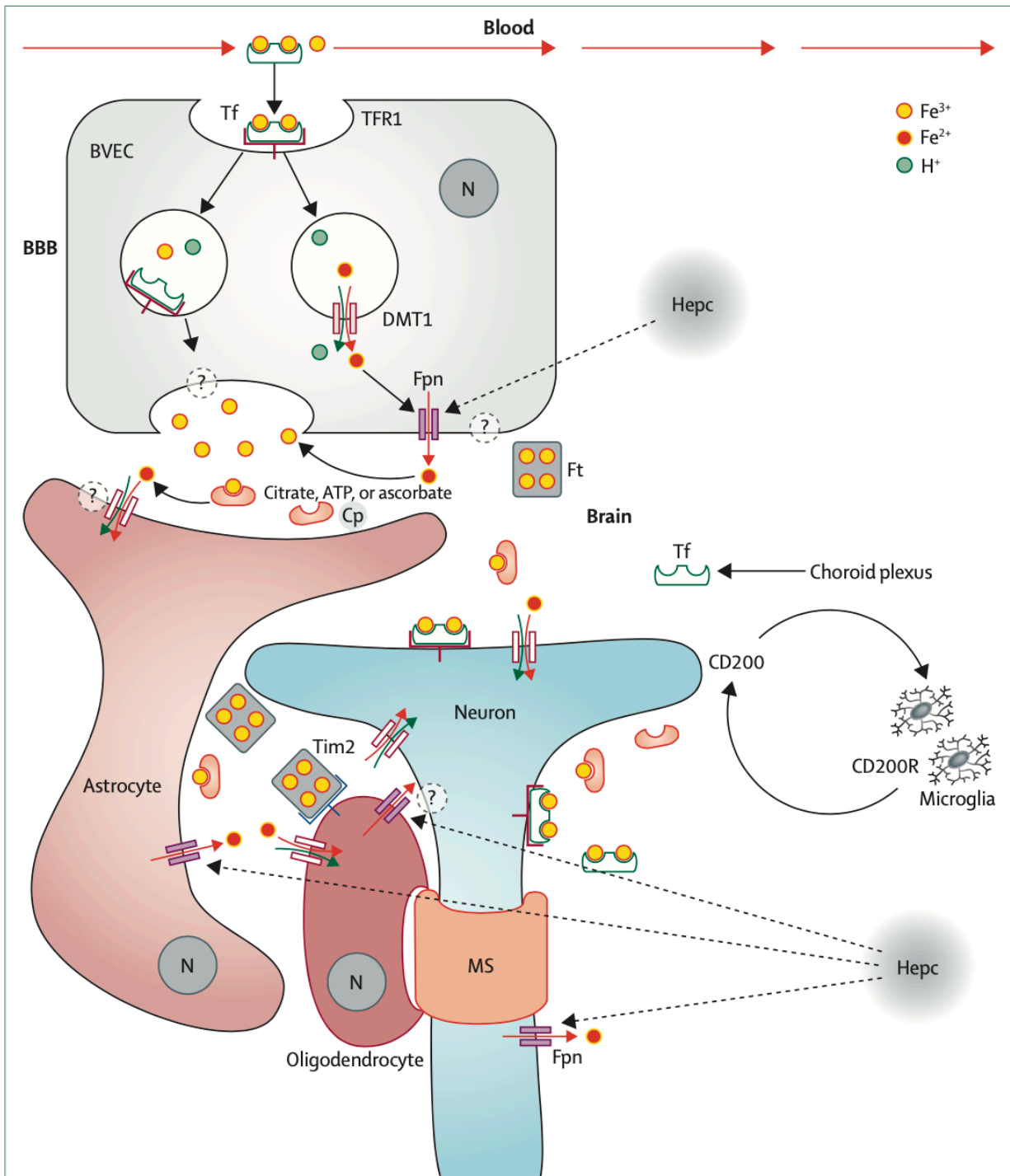


Fig 1 Brain iron metabolism

Dashed lines represent unknown regulation of iron. Solid arrows show iron movement. Reproduced from Ward and colleagues (2014). BBB=brain–brain barrier. TFR=transferrin receptor. Tf =transferrin. Fe²⁺=ferrous iron. Fe³⁺=ferric iron. BVEC=brain vascular endothelial cells. Cp=ceruloplasmin. Fpn=ferroportin. DMT1=divalent metal ion transporter 1. Ft=ferritin. IRP=iron regulatory protein. IRE=iron responsive or regulatory element. Hephepcidin. N=nucleus. MS=myelin sheath. ?=unknown pathway or mechanism. CD200=OX-2 membrane glycoprotein. CD200R=CD200 receptor.

Iron accumulation in brain cells needs to be tightly regulated to prevent toxic effects. Excess iron can induce oxidative stress by generating reactive oxygen species (ROS), notably the hydroxyl radical. ROS can damage DNA and mtDNA, affect DNA expression by epigenetic mechanisms, and oxidise proteins.

2. MRI Biomarkers of neurodegeneration

Magnetic resonance imaging (MRI) can detect iron due to its high magnetic susceptibility. Magnetic susceptibility is a dimensionless physical property that indicates the magnetizability of a material when exposed to an applied magnetic field. Elements and compounds are categorized as paramagnetic or diamagnetic based on their magnetic susceptibility. Paramagnetic substances (such as most biologic forms of iron and copper) have a positive magnetic susceptibility, are attracted to an external magnetic field, and increase the mean tissue magnetic susceptibility. On the other hand, diamagnetic substances (such as water, myelin, and calcifications) have a negative magnetic susceptibility, are slightly repelled by an external magnetic field and decrease the mean tissue magnetic susceptibility (Liu C et al. 2015).

2.1 QSM (Quantitative Susceptibility Mapping)

It's a promising MRI technique aimed to reproduce maps of the susceptibility distribution in tissues, starting from NMR-GRE T2*w phase data. This is possible thanks to the response of a magnetic susceptibility distribution inserted into an externally applied magnetic field.

The forerunner of this tool is called **SWI** - Susceptibility Weighted Imaging: this is another susceptibility-based technique, which allows to explore new

variables with respect to the traditional NMR techniques, but which does not provide an anatomical reconstruction (Liu et al. 2015, Haacke EM et al 2004).

2.1.1 Magnetic Susceptibility χ in the Human Body

The magnetic susceptibility χ is a property of matter, which measures the degree of magnetization of a material when it is exposed to a magnetic field. In the human body there are a lot of susceptibility sources. Those biomarkers and their specificities (such as the density and the concentration) allow healthy and unhealthy states to be determined and classified. Indeed, to study the tissue susceptibility helps in diagnosis and treatment of diseases.

Different MRI techniques can exploit susceptibility based on contrast in tissues. To better understand it, it has to be clear what magnetic susceptibility is and what we measure and describe when we are referring to it.

Magnetic susceptibility χ is a physical quantity which measures the extent to which a material is magnetized by an applied magnetic field (Liu C. et al 2015). In MRI, the tissues response is due to an external, static field \vec{B} so in this work we are going to refer to the static magnetic susceptibility. \vec{B}_0 is actually the magnetic flux density corresponding to the applied magnetic field \vec{H}_0 . The *magnetic flux density* is also called the *magnetic induction vector*.

2.1.2 Magnetic Field and Tissue Magnetization

Tissues in the human body react under the application of an external magnetic field, since they are characterized by magnetic properties. Their reaction is due to the interaction between the atomic electrons and the magnetic field, which causes the magnetization of the matter. Matter magnetization is quantitatively described by the **magnetization** \vec{M} , defined as

(<https://www.scribd.com/document/315221178/Swi>. María J. Otero Díaz, Magnetic Susceptibility in MRI. Lecture Slides).

$$\vec{M} = \frac{d\vec{m}}{dV} \quad (1.1)$$

where $d\vec{m}$ is the **elementary magnetic moment**. The magnetization \vec{M} and magnetic field \vec{H} are directly related. The susceptibility χ is the proportionality constant (Richard Bowtell. Magnetic susceptibility of biological tissues. Lecture Slides).

$$\vec{M} = \chi \vec{H} \quad (1.2)$$

χ shows both isotropic and anisotropic behaviour, depending upon the tissue under examination. In isotropic and homogeneous materials the response is uniform, and it means that χ can be modelled as a scalar quantity. But in some regions, the response of the tissue is not uniform: it depends on the orientation of the field, so χ shows an anisotropic reaction. This behaviour is an effect of the asymmetry of the molecules' structure. Thus, there are some situations in which the susceptibility is modelled as a tensor function of the applied magnetic field ($\vec{\chi} = \vec{\chi}(\vec{H})$). In such situations, the mathematical formalism for the phenomena description is more complicated.

In the meantime, we consider χ as scalar property of matter. To make clear the relationship between χ and the magnetic induction \vec{B} , remember that the following expression applies:

$$\vec{B} = \mu_0 (\vec{H} + \vec{M}) \quad (1.3)$$

where μ_0 is the vacuum permeability constant ($4\pi \cdot 10^{-7} \text{ H m}$). Then:

$$\vec{B} = \mu_0(\vec{H} + \chi\vec{H}) = \mu_0(1 + \chi)\vec{H} = \mu_0\mu_r\vec{H} \quad (1.4)$$

μ_r is called the relative permeability, and it represents the degree of the magnetization of the tissues (Collins CM et al. 2002). In MRI images, the ratio between magnetization and magnetic field defines the volume susceptibility ($\chi = \frac{\vec{M}}{\vec{H}}$) (Haacke EM et al. 2004). It is a dimensionless property, which can be measured in the SI (*Systeme Internationale*) or in CGS (Centrimetre-Gram-Second) systems. To pass from SI to CGS values one has to divide by a factor of 4π . For example (Collins CM et al. 2002, Schenck F et al. 2000):

$$\chi_{\text{water}} = -9.035 \text{ ppm (SI units)} = -0.719 \text{ ppm (CGS units)} \quad (1.5)$$

Water is the most abundant molecule in the human body. $\Delta\chi$ between water and other tissues inside the body is on the order of ± 0.1 ppm (Liu C et al. 2015). The biggest gap is between water and air, since χ_{air} is equal to $+0.37$ ppm (in SI units) (Fig. 2.1). During a magnetic resonance experiment, a region of interest ROI, containing different tissues, is explored. Different tissues have different values of susceptibility, which are described by the $\chi(r)$ distribution. We are going to explain, in Section 2.2, how this distribution affects the NMR measurements.

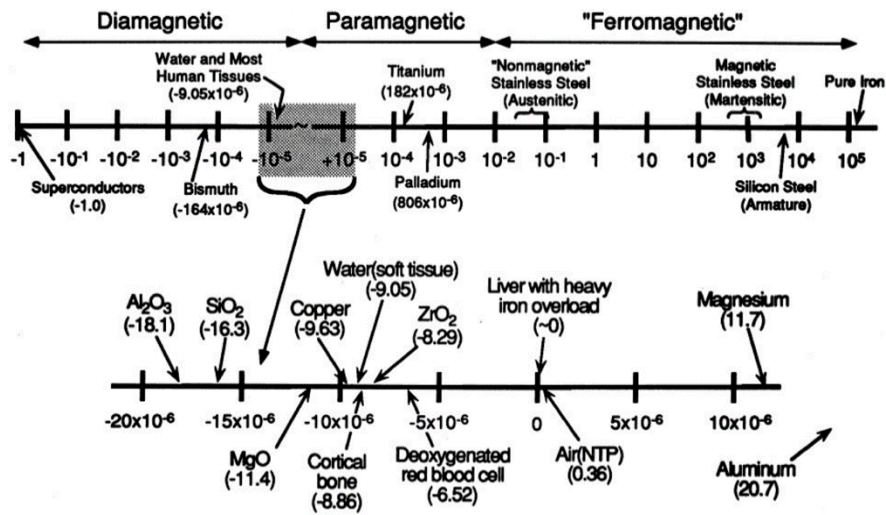


Figure 2.1: Scale of magnetic susceptibility values of some element and compounds in the human body (Schenck JF 2000)

2.1.3 Magnetic Materials: Dia-, Para- and Ferro-magnetic Conditions

In almost all the materials, without an externally applied magnetic field - $\vec{H} = \vec{B} = 0$ -, the magnetization vector \vec{M} has intensity equal to zero. When instead \vec{B} is $\neq 0$ and $\vec{H} \neq 0$, also \vec{M} is $\neq 0$ because of the equation Eq. 1.3. The direction, sense and intensity of \vec{M} are related to χ and μ_r , which affect the magnetic response of matter. Magnetic susceptibility values depend on the atomic and the molecular structure: availability of unpaired electrons, distribution of electron cloud, competition between spin and induction and microstructure (Liu C et al. 2015). In relation to these characteristics, materials are divided in three main classes: diamagnetic, paramagnetic and ferromagnetic materials.

Diamagnetic Materials

Diamagnetism is a magnetic property of matter which let a repulsive force be induced when an external magnetic field is applied. All the materials have this property, but sometimes other forms of magnetism, such as paramagnetism or ferromagnetism, dominate the diamagnetic effect. The diamagnetic materials

have not a permanent magnetic moment $|\vec{\mu}|$. The presence of an external magnetic field induced a magnetization field \vec{M} . \vec{M} has a small intensity and is directed in the opposite sense with respect of the field. This is due to electron induction currents which generate a magnetic field directed in the opposite sense with respect of the external one (Lenz's Law) (<https://www.scribd.com/document/315221178/Swi. Maria J. Otero Diaz, Magnetic Susceptibility in MRI. Lecture Slides>).

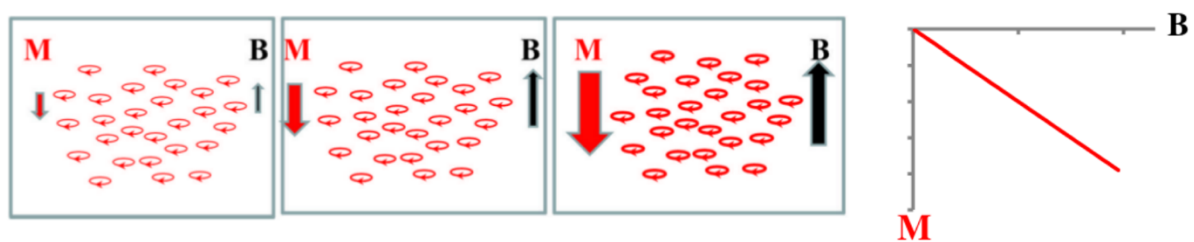


Figure 2.2: Scheme of magnetization vector \vec{M} and external magnetic field \vec{B} in diamagnetic materials ((11)). In balance condition, without an external magnetic field, diamagnetic materials have net magnetic moment equal to zero. When a field $B\sim$ is applied, a weak magnetization vector \vec{M} is formed along the same direction of the field but in the opposite sense.

In the human body, almost all the substances are diamagnetic (Deistung A et al 2017. 1). These diamagnetic materials have χ values small and negative. Water is diamagnetic ($\chi_{water} = - 9.035$ ppm), but also calcium, **oxyhemoglobin** (HbO_2, Fe^{3+})⁴ and **myelin** (Liu C et al 2015). Myelin sheaths envelop the **white matter (WM)** structures in the brain; for this reason WM appears as a primarily diamagnetic tissue.

Paramagnetic Materials

In contrast to diamagnetic materials, the paramagnetic and ferromagnetic ones are attracted by an externally applied magnetic field. The magnetic moments $\vec{\mu}_i$ in the paramagnetic materials have a non-zero intensity value even if there is not an

external field \vec{B} applied. When a \vec{B} is applied, the material is magnetized ($\vec{M} \neq 0$). \vec{B} and \vec{M} are directed in the same way. So, the external magnetic field is reinforced. Without an external magnetic field the magnetic moments of the single particles are directed in a random way. To simplify the description, consider only the \vec{z} direction and look into the Fig. 2.3: n_+ is the number of the magnetic moments pointing up, n_- the number of magnetic moments pointing down. In a balanced situation ($\vec{H} = 0 \rightarrow \vec{M} = 0$), $n_+ = n_-$. This balance is broken when an external field is applied. The imbalance $n_+ - n_-$ is proportional to $\frac{\mu B}{k_B T}$ when $|\vec{\mu}||\vec{B}| \ll k_B T$ - where $\sim \mu$ is the total magnetic moment, k_B the Boltzmann constant ($1.23 \cdot 10^{-23} \text{JK}^{-1}$) and T is the temperature. When \vec{B} has a strong intensity ($|\vec{\mu}||\vec{B}| \gg k_B T$), the relationship stops to be linear and n_- tends to zero (Richard Bowtell. [Magnetic susceptibility of biological tissues . University of Nottingham, UK. Lecture Slides](#)). All the single magnetic moments tend to line up in the same direction of the field.

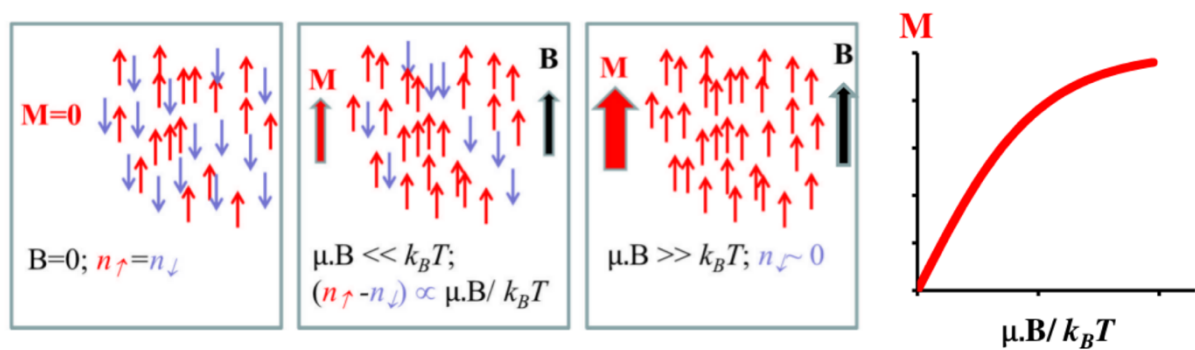


Figure 2.3: Scheme of magnetization vector \vec{M} and external magnetic field \vec{B} in paramagnetic materials. In absence of an external magnetic field, the number of magnetic moments pointing up n_+ and the ones pointing down n_- balance each other. When an external field is applied, the majority of the magnetic moments start to align as the field. When the intensity of the field is strong, the number of the magnetic moments directed in the opposite sense of the field tends to zero. (R. Bowtell)

Unpaired electrons produce strong paramagnetic effects. Their spins tend to align themselves along the direction of the field. In this way, they make it stronger in intensity. In paramagnetic materials, χ assumes small and positive values; the relative permeability μ_r is slightly greater than 1. **Deoxyhemoglobin (HbFe^{2+})**

is paramagnetic, and also iron-storage substances (i.e. ferritin and hemosiderin). Iron, inside the brain, is mainly concentrated in **the gray matter (GM)** structures. Thus, GM is mainly paramagnetic.

Ferromagnetic Materials Also ferromagnetic materials react in a constructive manner when an external field is applied. They are characterized by a net magnetic moment, also in absence of an external field. When a field is externally applied, their reaction is stronger than paramagnetic materials: their magnetization is long lasted, and they may become magnets. This happens thanks to a very energetically favorable energy exchange between the material and the field. Ferromagnetic materials are predominantly metals. Their magnetic moments are very high in intensity, so the magnetic susceptibility values are positive and very large. There are not elements stored in known ferromagnetic structures in the human body (Liu C et al. 2015). even if there are ferromagnetic elements. For example, iron is a ferromagnetic element, but ferritin and hemosiderin, which store iron, are not.

2.1.4 Susceptibility Sources in Human Body

Mean magnetic susceptibility of organic tissues is determined by their composition and the magnetic susceptibility of their constituents. The brain tissue is generally weakly diamagnetic since water (slightly diamagnetic) constitutes 70–85% of the brain. Magnetic susceptibility varies slightly among brain regions due to the differences in their tissue composition. The major contributors to the measurable changes of magnetic susceptibility across the brain are myelin (weakly diamagnetic) and iron-containing molecules (mostly strongly paramagnetic). The largest proportion of non-heme iron in the brain is bound to ferritin, which makes up the greatest contribution to the tissue magnetic

susceptibility among all iron compounds. Other forms of iron, including free and transferrin-bound iron only minimally contribute to the measured mean tissue susceptibility (Liu et al. 2015, Deistung et al., 2017).

Below, we give a list of the most interesting materials to analyze in evaluating human body state.

Iron

Despite the presence of trace amounts of paramagnetic transition metal ions, such as copper, manganese and cobalt, it is the significantly higher abundance of iron that creates a dominant paramagnetic contribution to tissue magnetic susceptibility in vivo (Deistung et al. 2017). The four unpaired electrons in the d-shell cause its magnetic response. In the human body, there are around 3-5 g of iron. Iron is ferromagnetic, but, as we have already noticed, it is stored in different structures. One third of iron is found in non-heme compounds, in which iron is in a ionic form. The two main structures are ferritin (Fe^{3+}) and hemosiderin (Fe^{2+} and Fe^{3+}), which are paramagnetic (Liu C et al. 2015). The remaining two thirds is stored in hemoglobin, and also does not show ferromagnetic behaviour. Iron deposition is the main reason of the paramagnetic susceptibility values in the brain. One often refers to it as the brain iron. Thus, a susceptibility map may be used to describe and quantify iron stores, also in the brain and in the nervous system in general. These stores are mainly concentrated in the gray matter structures.

Histological studies have revealed that brain iron concentration in deep GM nuclei and cortical areas increases with age, typically with a rapid increase from birth until about 20 years of age (Ramos et al. 2014). Thereafter, the increase slows down

and, in some brain regions, a distinct plateau is reached at middle age. Similar age trajectories have recently been demonstrated non-invasively using QSM in vivo (Persson et al., 2015). Iron concentration is an age-based parameter, and it is associated with some neurodegenerative conditions - i.e. Parkinson's and Alzheimer's diseases. QSM promises to be a valuable non-invasive tool for the assessment of iron deposition in deep GM nuclei, and offers an elegant possibility to study iron in various neurological and psychiatric disorders. (Deistung A. et al 2017).

Hemoglobin

The majority of the human iron is stored in hemoglobin (Richard Bowtell. *Magnetic susceptibility of biological tissues*. University of Nottingham, UK. Lecture Slides). It is a blood's metalloprotein, containing four iron atoms, involved in the oxygen transport. It may be found in two forms: oxyhemoglobin and deoxyhemoglobin (Fig. 2.4). In the first form, the molecule is carrying oxygen ($(\text{HbO}_2, \text{Fe}^{3+})$) - Fig. 2.4, left panel). Iron is temporarily oxidized from Fe^{2+} to Fe^{3+} . It is weakly diamagnetic, thanks to ligand interactions inside the structure, that prevents the unpaired electrons in the iron ion from showing paramagnetic effects (Wang Y et al. 2015). Instead, the second form of hemoglobin is the structure that the molecule assumes when the oxygen is released during the metabolic consumption ($(\text{Hb}, \text{Fe}^{2+})$) - Fig. 2.4, right panel). It is strongly paramagnetic, because it has four unpaired electrons per heme. Also, deoxyhemoglobin may further oxidized in methemoglobin, which has five unpaired electron per heme. It shows a ferromagnetic response (Liu C et al. 2015). To study hemoglobin magnetic effects aims to study BOLD signals and all disorders connected with the blood flow (Richard Bowtell. *Magnetic susceptibility of biological tissues*. University of Nottingham, UK.

Lecture Slides), thanks to the oxygenation related susceptibility changes occurring in blood products.

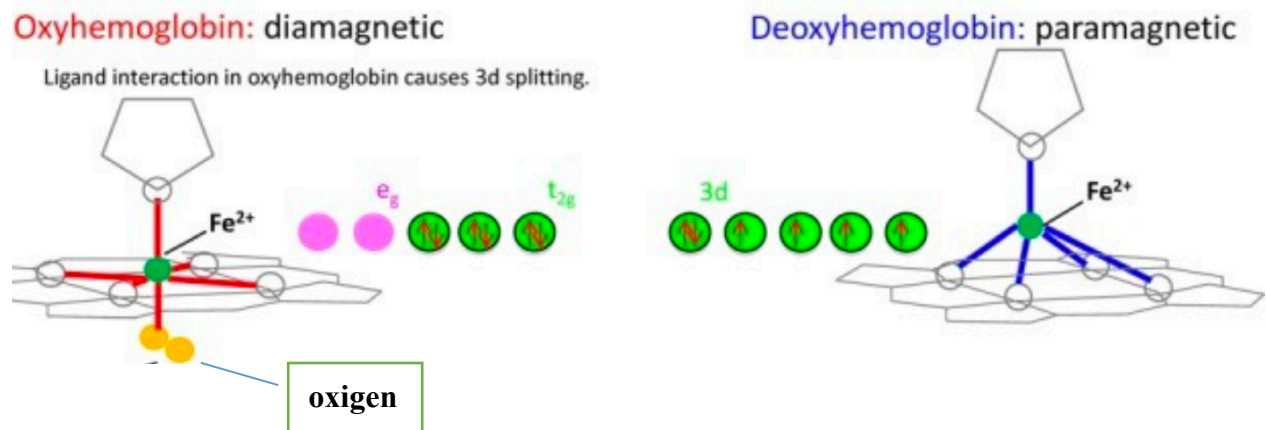


Fig 2.4 Oxyhemoglobin (-) and deoxyhemoglobin structure (Wang T. and Liu T 2015)

Myelin

Myelin, being predominantly present in WM, is a significant contributor to tissue magnetic susceptibility. It is a special membrane structure with a high abundance of lipids (phospholipids, sphingolipids consisting of extremely long acids ranging from C18 stearic acid to C24 lignoceric acid), water and proteins (C. Liu W. et al 2015) which, overall, render myelin more diamagnetic than water. Myelin forms a compact multilayered membrane by wrapping itself tightly around the axon, thus supporting efficient transport of action potentials along the axon. in the brain and in the spinal cord (Liu C et al 2015).

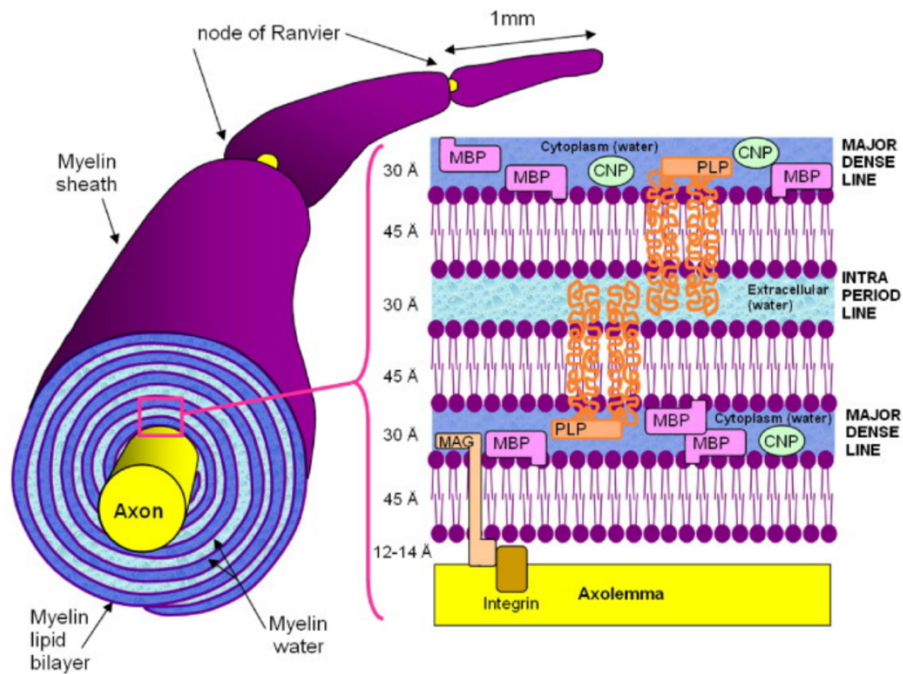


Figure 2.5 Myelin structure (Laule et al 2007)

It is composed of proteins (10%), water (40%) and lipids (50%) (Richard Bowtell University of Nottingham, UK. Lecture Slides), which are responsible to the electric insulation myelin provides. For most of these components, the volume susceptibility assumes diamagnetic values, some of them are more diamagnetic than water - i.e. $\chi_{\text{phospholipids}} = -9.68 \text{ ppm}$, $\chi_{\text{sphingolipids}} = -10.03 \text{ ppm}$ (Wang Y and Liu T 2015).

Myelination and **de-myelination** are age-based processes; loss of myelin is related with some neurodegenerative autoimmune diseases - e.g. Multiple Sclerosis.

Also, the WM tracts in the brain consist of myelinated nerve fibers (Wang Y 2015). In here, the several layers of bilayers lipid are very sensitive to the particular microstructures of WM. Indeed, here the susceptibility shows anisotropic response. This is the reason why to model χ as a tensor is more appropriate if the white matter inside the brain is the object under examination. WM has a very particular and complex structure. Its study requires more attention also because of its compartmentalization. It is in different compartments, such as the axonal

space, the myelin space and extracellular space, and each of them has specific magnetic properties and reacts in a unique way (Liu C et al 2015, Wharton W et al. 2015).

Calcium

It is an essential element, involved, for example, in the building of bones and in the synthesis of blood cells. It is stored in different structures in the human body, often in a ionic form (Ca^{2+}). If calcium magnetic properties are under examination, it is actually more precise to speak about calcification rather than proper calcium. In fact, there are many studies and insights about calcium-related pathologies (i.e. calcified lesions) but not many about the healthy state conditions (Wang Y and Liu T 2015). Calcification in damaged tissues causes the local tissue to appear diamagnetic in MRI susceptibility based techniques. To analyze a susceptibility distribution $\chi(\mathbf{r})$ is useful to understand physical mechanism in healthy and unhealthy human tissues. It is possible to investigate $\chi(\mathbf{r})$ with MRI techniques thanks to the relationship between $\chi(\mathbf{r})$ and the field perturbations $\Delta B(\mathbf{r})$ that it produces. The latter quantity is strictly related with the $\varphi(\mathbf{r})$ distribution measured during gradient echo NMR experiments.

2.2 Susceptibility and Imaging

There are many advantages in analyzing human tissues magnetic properties and responses. There are biomarkers, such as iron, calcium, and myelin, whose changes in concentration and state are strictly related with many disorders and pathologies. They are marked by different magnetic properties.

Thus, to study those properties means to study and analyze human body diseases. Some MRI techniques are specific for these kind of studies, using tissues magnetic susceptibility χ as the principal observable. Instead of other tools, to use magnetic resonance is better because it implies a non-invasive procedure. Susceptibility-

based techniques use information in phase data from gradient echo MRI measurements. Before these tools became available, only magnitude information was used; φ was ignored, even if it contained information about local χ changes between tissues.

The main problem in using the raw φ data is that they show some artifacts and they do not contain only local voxel information, but also some from effects of background fields. So, before using phase data in χ -based imaging techniques, the data need to be pre-processed by unwrapping and background field removal algorithms. Without them, the χ -induced field perturbations in MRI may be considered only source of noise and artifacts, without any significant meaning. After the φ pre-processing, the proper χ -based map can be obtained. We are going to describe the pre-processing stages first, and then the two techniques SWI [Haacke E M., Y. Xu et al, 2004.] and QSM (Deistung, F. et al 2017, Wang Y. and Liu T. 2015).

Below, a brief representation of the GRE sequence is given.

2.2.1 Gradient Echo Sequence

The most frequently used sequence in susceptibility-based imaging techniques is called the Spoiled Gradient-Recalled-Echo -SPGR or GRE sequence. A scheme is reported in Fig. 1.6. About the magnitude images (Eq. 1.6), in the first row, a single- or a multiexponential decay occurs, in order to allow the use of single echo or multiple echoes respectively. About the phase images φ (Eq. 1.6), in the second row, they measure the local frequency offsets relative to the Larmor frequency (Liu C, Li W et al 2015), which is related to the magnetic field perturbations

The measured NMR signal at echo time TE is:

$$S(TE) \propto \frac{-TE}{T_2^*} \propto e^{-TE/T_2^*} \cdot e^{i\varphi} \quad (2.6)$$

$$\varphi = \varphi_0 - \gamma \Delta B T E \quad (2.7)$$

φ_0 is an offset related to the RF phase and sequence adjustment. ΔB represents the main magnetic field perturbations. To estimate them, multiple measurements have to be performed. The MRI theory and acquisition sequence explanation is behind the proposal of this work. Deeper descriptions can be found in ([Brown R.W et al 2014](#)).

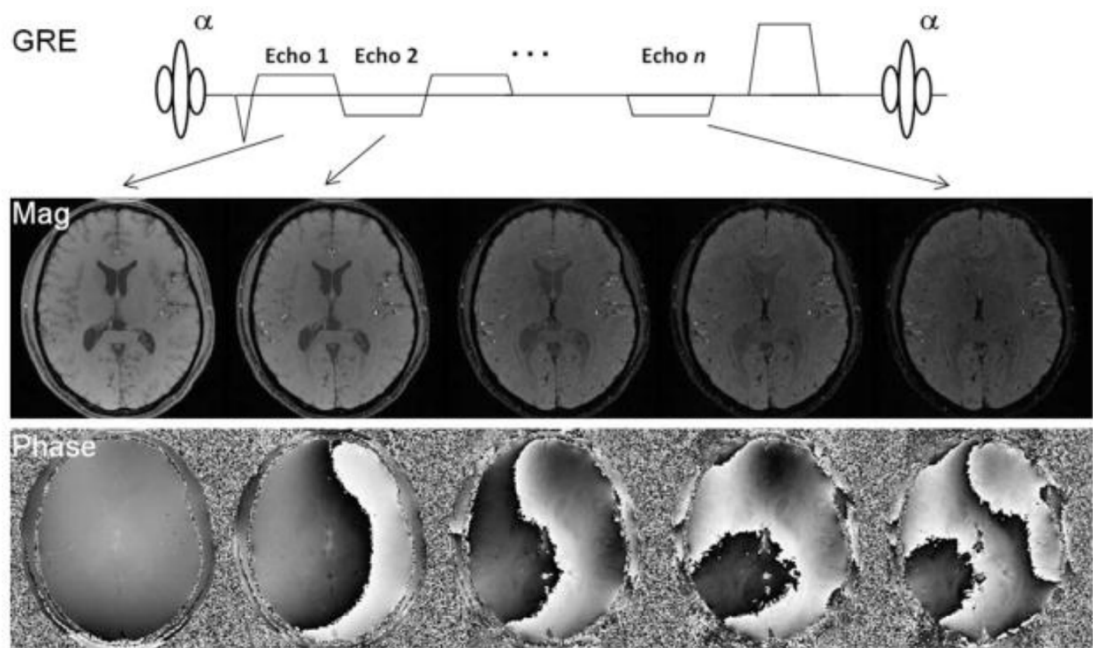


Figure 2.6: A spoiled multiecho gradient sequence. Alternating readout polarities are illustrated. The contrast in the magnitude images evolves as the echo time increases due to T_2 decay. Phase values increase as TE increases, thus more phase wraps appear at later echoes. SWI and QSM use either single or multiple echos ([Liu C et al 2015](#))

2.2.2 Raw Data Processing: Phase Unwrapping and Background Field Removal

The first operation to perform on raw φ data is the elimination of artifacts coming from the discontinuities caused by phase wrapping ([Schofield M. and Zhu Y 2003](#)). In fact, trigonometric functions, such as sine and cosine, are periodic, with period $T = 2\pi$. During the acquisition, all the angles outside of the range $[-\pi, +\pi]$ will be folded back into this range. An example of a raw φ map is reported in Fig. 2.7.

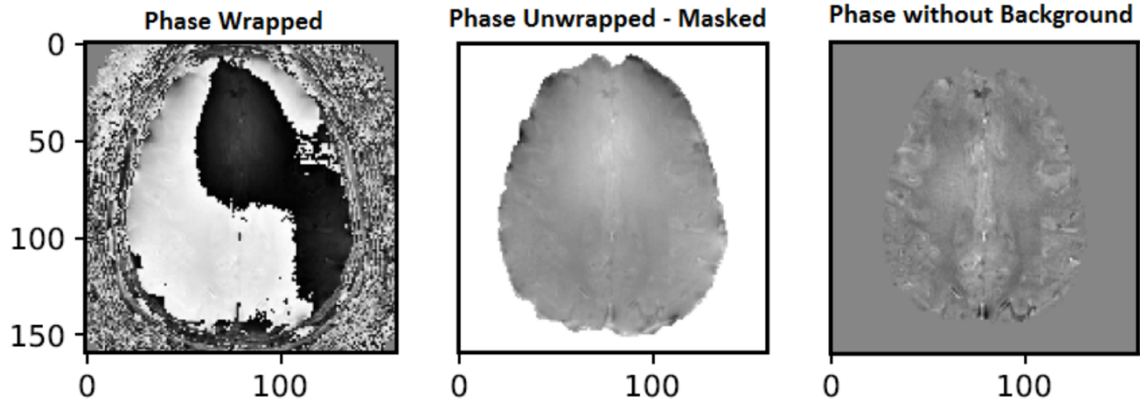


Figure 2.7: Raw φ data from NMR-GRE measurements. Central panel: same data after the application of an unwrapping algorithm. The data were also masked. Right panel: same data after the application of a background removal algorithm (LBV) - data from (Langmaker et al 2016)

As can be noticed from the picture, the map is not clear at all and to extract useful information from that is very difficult. Another problem to handle in this stage, in addition to the discontinuities, is the low values of **SNR - Signal-to-Noise Ratio**. Furthermore, the background field contribution in NMR measurements worsens the wrapping effect. In fact, in order to the shimming set during the acquisition, the NMR signal contains also information of the area where the region of interest is. The total field information B_T is the sum of two contributions, the local one and the one from the background (Zhou D, Liu T et al, 2014) :

$$B_T = B_L + B_B \quad (2.8)$$

The origin of the background field perturbations is related to the main field inhomogeneities, increasing with the intensity of the field, with the inaccuracies in the shimming setting and with the external χ sources (Deistung A. et al 2017). So, to obtain the local $\chi(r)$ distribution, namely whose of the region of interest, the external contribution has to be eliminated. Ideally, the background effect may be

removed with a previous reference scan, in which the region of interest is replaced with a uniform region with known susceptibility. However, this approach is impracticable in the clinical area. So, other post-acquisition techniques have to be implemented.

Fortunately, B_B and B_L have different characteristics, thanks to which it is not too difficult to separate these two contributions, after the acquisition, and to eliminate the background one. In fact, B_L is small in intensity with fast spatial variations. On the contrary, B_B is high in intensity and the spatial variations are slower. The main difference, exploited directly or indirectly in background removal algorithms, is that B_T may be described as harmonic function (Evens LC 2010). Then, background removal algorithms are often solvers for differential equations. In fact, Laplace's equation may be solved to obtain the background field function B_B (Zhou T. et al 2014):

$$\Delta B_B = 0 \quad (2.9)$$

or Poisson's equation may be solved to obtain the local field expression B_L

$$\Delta B_L = \Delta B_T \quad (2.10)$$

There are also algorithms which work as high-pass filters, exploiting the fact that the signal variations which we are interested in are faster varying in space than the ones associated to the background, so they correspond to high spatial frequencies range. Some of the most used background field removal algorithms are: **PDF** - Projection onto Dipole Fields (Liu T, I. Khalidov I et al. 2011, Moon T.K et al 2000), **SHARP** - Sophisticated Harmonic Artifact Reduction for Phase data and **RESHARP** - Regularization Enabled SHARP (Sun H et al. 2014), **LBV** - Laplacian Boundary Value (Zhou D. et al. 2014).

In Fig. 1.7, right panel, a φ map after a background removal algorithm is shown. In that case, the LBV technique was used.

2.2.3 Susceptibility Weighted Imaging

SWI Susceptibility-Weighted Imaging (SWI) (Liu C et al. 2015, Haacke EM et al. 2004).

uses both T_2^* magnitude and ϕ data from gradient echo sequences (Liu C et al. 2015, Haacke EM et al. 2004). Taken individually, these two maps

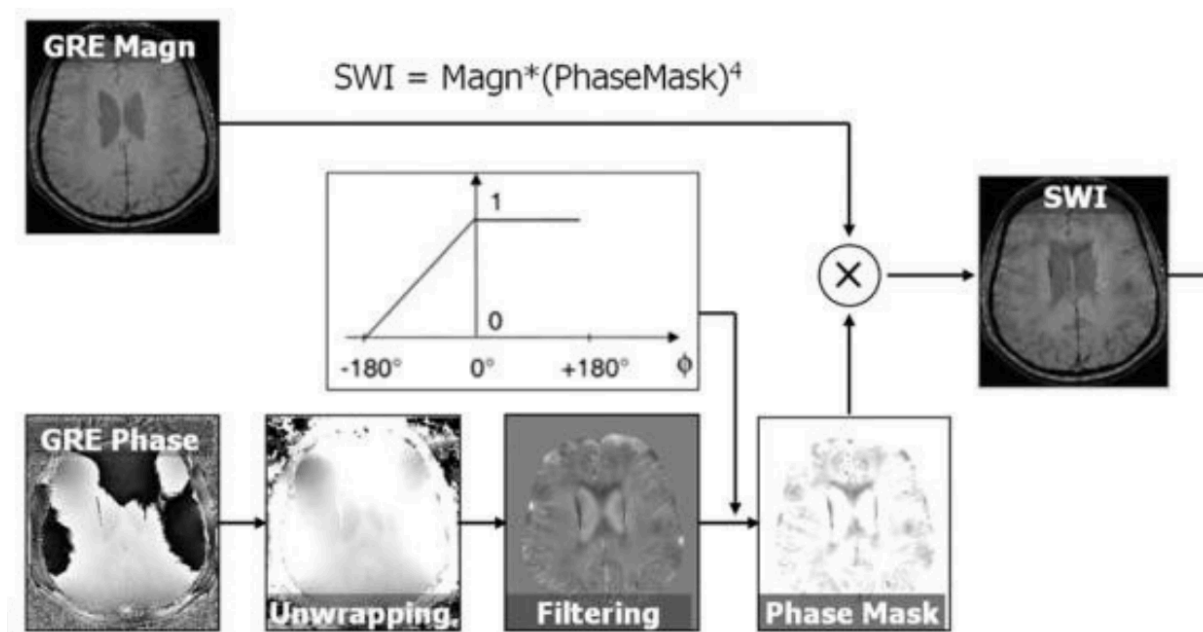


Figure 2.8: Scheme of operations which have to be performed in SWI technique. GRE phase data are processed with unwrapping and background field removal (high-pass filtering) algorithm. The returned map is transformed in a mask with intensity values between 0 and 1. Then, a pointwise multiplication is done between this mask and the GRE magnitude mask, n times. $n = 4$ (Liu C et al 2015)

carry only half of the useful information contained in a NMR acquisition (Eq. 2.6). Before, we have noticed that the construction of a χ -based map is possible thanks to the relationship between χ and the measured ϕ data. Actually, it is not only the ϕ map which contains χ -based contrast information; also the magnitude map does (Liu C, Li W et al 2015).

Using both, tissue contrast is reinforced. To enhance the intensity variations, many stages have to be followed, to combine magnitude and phase information. This combination is not unique, there are different ways to do this. In Fig. 2.8, a scheme of the most common procedure used nowadays is shown.

The GRE phase map has to be pre-processed, with an unwrapping and background field removal algorithm. Specifically here, a high-pass filtering operation is performed. This kind of filter exploits the fact that the spatial variations of the background field are slow, at least slower than the signal under consideration. The correspondent frequencies are indeed deleted with a high-pass filter. Then, the resulting φ map is transformed into a mask φ mask with intensity values between 0 and 1. A pointwise multiplication between GRE magnitude map M and this mask is performed, n times ($[M * \varphi \text{mask}]_n$). The value of n depends on the phase differences and on the contrast-to-noise ratio values. If there is no any specification, like in this situation, it is often set to be equal to 4 (Liu C et al 2015). A SWI map provides the evidence of particular contrast, different from the one based on the spin density, T_1 , T_2 or T_2^* . It helps, for example, to enhance the differences in contrast between WM and GM, or between fat and water. The main drawback of SWI is that it does not provide a quantitative susceptibility map: it is like a weighted-sum of the magnetic properties of the tissues. Thus, SWI does not allow the local magnetic properties of the single voxels to be explored. To do this, the phase map has to be deconvolved and a Quantitative Susceptibility Mapping algorithm has to be performed.

2.2.4 Quantitative Susceptibility Mapping

Quantitative susceptibility mapping (QSM) solves the deconvolution or inverse problem from magnetic field to susceptibility source to map a local tissue magnetic property (de Rochefort L et al. 2010; Wang Y and Liu T 2015). This local

property is fundamentally different from the nonlocal property of traditional gradient echo (GRE) MRI, including susceptibility weighted imaging (SWI), the closely related GRE magnitude T_2^* -weighted imaging (T_2^*w), and GRE phase imaging (Phase), although both QSM and traditional GRE MRI are regarded as being sensitive to susceptibility ([Reichenbach JR et al 2015](#); [Liu C, Li W. 2015](#), [Haacke EM, Liu S et al 2015](#))

. Without deconvolution, traditional GRE MRI generally suffers from blooming artifacts, which 1) may generate contrasts at neighboring locations without susceptibility sources, in addition to at locations with susceptibility sources; 2) strongly depend on imaging parameters, including field strength, voxel size and echo time; and 3) deceptively vary with object orientations, where tissue interfaces with susceptibility differences perpendicular to the main field B_0 have much greater contrasts than interfaces parallel to B_0 (6). With deconvolution, QSM eliminates the problem of blooming artifacts and provides quantitative distribution of susceptibility sources in tissue. Without deconvolution, traditional GRE MRI can only detect the presence of susceptibility interfaces perpendicular to B_0 , and cannot localize or quantify any susceptibility source. With deconvolution, QSM can precisely localize and quantify these sources ([Wang Yi et al 2017](#)).

The main idea underlying QSM is to extract the susceptibility source from its blooming artifacts on traditional GRE MRI through rigorous biophysical modeling of the MRI signal phase. Phase has historically been largely discarded in routine MRI practice, though MRI data is inherently complex, consisting of half phase and half magnitude. Yet, phase data provides rich insight into tissue properties that are complementary to magnitude data ([Wang Y. 2012](#)). Recalling that signal in clinical MRI comes from water (and sometimes fat) protons, phase reflects the inhomogeneous magnetic field experienced by protons. The field sources consist of tissue molecular electron clouds and background sources

outside tissue. They become magnetized in the MRI main field B_0 according to their magnetic susceptibilities and contribute to the magnetic field as dipoles according to Maxwell's equation. The tissue field and background field can be separated according to their source location difference (background field removal). Therefore, MRI phase can be processed to generate the tissue field, which can be analyzed according to the dipole field model to determine tissue magnetic susceptibility (Fig.1).

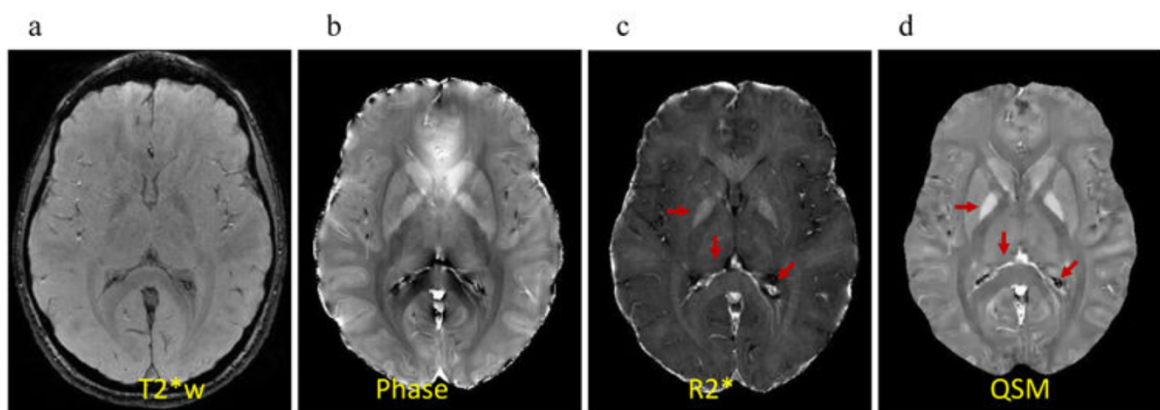


Fig 2.9 GRE MRI of a healthy subject: a) magnitude image of T_2^* weighting (T_2^*w , $TE=18\text{msec}$), showing marginal tissue contrast in the basal ganglia gray matter, b) phase-derived field image after unwrapping and background field removal, showing substantial contrast within the basal ganglia, c) R_2^* and d) QSM, showing bright contrast for iron in the globus pallidus (horizontal arrows) and vein (vertical arrows). However, calcification in the ventricle (oblique arrows in c&d) is shown bright on R_2^* but dark (negative susceptibility) on QSM.

2.3 Susceptibility Mapping and Clinical Applications

QSM can be used in all clinical applications of traditional GRE MRI including T_2^*w , Phase, and SWI (Haacke, EM., Reichenbach, JrR. 2011). Here, we describe only clinical applications that are enabled by QSM but that are beyond the reach of traditional GRE MRI. There are many diseases for which QSM can be used to measure biometal changes during pathogenesis, progression, and treatment. To illustrate the potential of these clinical applications, we use major cell types, their biometals and generalizable principal disease examples. Accordingly, this section

is organized into iron in neurons, iron in macrophages/microglia, iron in red blood cells, iron deficiency and calcification.

2.3.1 Iron in neurons: neurodegenerative diseases

The potential of QSM applications in neurodegenerative diseases can be illustrated with PD.

Monitoring iron chelation therapy in PD (Eskreis-Winkler S. et al. 2016). Although the pathogenic pathways of iron in PD are still under active investigation, increased iron in the substantia nigra pars compacta correlates with disease severity (Atasoy HT et al. 2004). A recent clinical trial for the iron chelator deferiprone has for the first time demonstrated a disease-modifying effect (Devos D, Moreau C et al. 2014) reported very encouraging results showing that DFP improves PD motor performance and reduces nigral R_2^* values on GRE MRI, suggesting that DFP can be the first disease-modifying therapy for PD. To evaluate the efficacy of deferiprone (DFP), as well as that of other iron chelators, a direct measure of nigral iron content is essential. Iron has previously been measured using R_2^* , which is known to suffer from blooming artifacts and to depend on imaging parameters. Recently, QSM has been demonstrated as a more sensitive detector of iron accumulation in the substantia nigra pars compacta as compared with R_2^* , (Barbosa JHO et al. 2015, Murakami Y et al. 2015; Du G et al. 2016). QSM is the best currently-available biomarker for monitoring of iron-chelation therapy. Because QSM is superior to R_2^* for evaluating nigral iron (Barbosa JHO et al. 2015, Du G et al. 2016, He N et al. 2015, Murakami et al. 2015, Langkammer C et al. 2016) an important potential application of QSM in PD is to measure DFP's effectiveness of target-engagement in clinical trials.

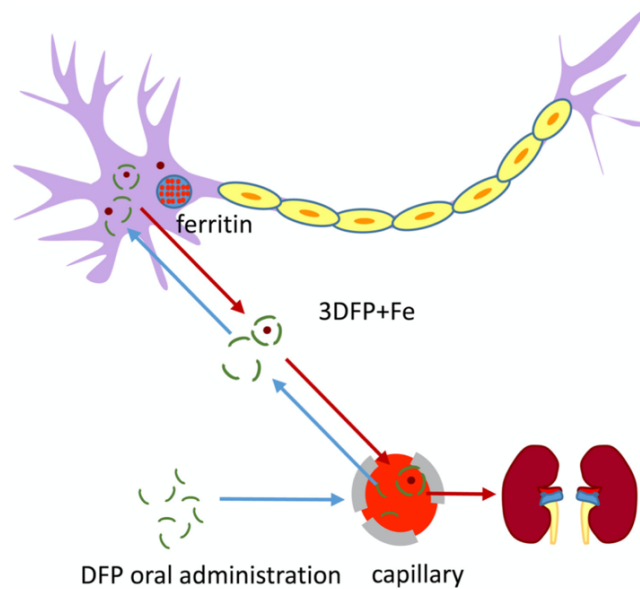


Fig 2.10 Iron chelation therapy for neurodegenerative disease. The deferiprone (DFP) can permeate through the blood brain barrier (BBB) and captures labile iron that is loosely bound to proteins, forming 3DFP Fe⁺. The complex carries zero charge and diffuses through the BBB, leading to excretion via urine. (Wang et al 2017)

QSM-Guided Surgery- Guiding Deep Brain Stimulation (DBS)

DBS, is an effective treatment for severe and/or advanced movement disorders including PD and other neurological disorders (Vega RA et al. 2015). Accurate geometric definition of deep gray nuclei is mandatory for pre-surgical mapping prior to this procedure. Many cases of advanced disease are treated with DBS, which requires implantation of a stimulating electrode in the deep gray matter of the brain, commonly in the STN (subthalamic nucleus). Precisely locating the ellipsoid-like STN, which measures approximately 4 mm in short axis length, is essential for maximizing therapeutic benefit while minimizing side effects, which occur when the DBS electrode is incorrectly placed (Richter EO et al. 2004). Currently, real time microelectrode recordings during DBS are used to monitor DBS electrode positioning in awake patients during surgery, and pre-surgical mapping of the STN is required to plan the path for DBS electrode insertion (Gross RE et al. 2006). MRI is the best imaging tool for STN mapping, as compared with other imaging modalities such as CT (computed tomography); however the STN

is still not well visualized on conventional MRI sequences, especially in those with non high field.

Since the STN has high iron content, QSM can be used for drastically improved depiction, as compared with T2-weighted (T2w), T2*-weighted (T2*w), and susceptibility-weighted imaging (SWI) (Plantinga BR et al 2014, Liu T, Eskreis-Winkler S et 2013, Schaefer A et al 2012). QSM using 7T MR can further hone visualization of the STN, and can detect the increased iron along the medial-inferior tip of the STN, which has been validated histologically. Therefore, QSM is the best currently available imaging technique for DBS surgery and can limit the morbidity associated with inaccurate DBS electrode placement (Chandran AS et al. 2015, Chandra AS et al. 2016).

2.3.2 Iron in macrophages and microglia: neuroinflammatory diseases

Monitoring smoldering inflammation after the blood–brain barrier (BBB) seals in MS. MS is an inflammatory demyelinating disease of the central nervous system, consisting of episodes of inflammatory attacks on the brain followed by smoldering persistent inflammation in the first phase (relapsing and remitting MS), and by deteriorating (Kutzelnigg A et al. 2014). MRI visualization of MS white matter (WM) lesions on conventional MRI sequences is central to disease diagnosis and therapy monitoring but correlates only weakly to physical disability score (Nijeholt G et al.1998). The pathogenesis of MS lesion formation, including demyelination and iron deposition, increases magnetic susceptibility and can be measured on QSM (Wisnieff C et al. 2015, Chen W et al., 2014. Zhang Y et al. 2016). In particular, pathology and QSM studies have reported that iron deposition at the rim of MS WM lesions is in M1 microglia/macrophages, which cause smoldering inflammation that persists after the BBB reseals (Wisnieff C et al. 2015, Mehta V et al. 2013, Hametner S et al. 2013, Zhang Y et al 2016). This smoldering inflammation in MS

brains, which is beyond the detection of the current standard-of-care gadolinium (Gd)-enhanced T1-weighted imaging (T1w), can be captured for the first time on QSM.

Susceptibility-based imaging, such as SWI, can detect the smoldering inflammation of chronic active MS lesions due to lesion iron deposition (Haacke EM, Makki M et al 2009), but only QSM can accurately depict the spatial geometry (e.g. hyperintense rim) of iron distribution (Wisnieff C, et al 2015, Li X, Vikram DS et al 2012, Eskreis-Winkler S et al 2015). The WM lesion susceptibility value measured by QSM has been demonstrated to be correlated better than conventional MRI with clinical disabilities (Rudko DA et al 2014). Therapies to delay the onset of and to treat secondary progressive MS are being actively developed using drugs targeting inflammation behind a closed BBB (Lassmann H. 2011). QSM can serve as a biomarker of MS inflammation, and its inclusion in MS MRI protocol in current clinical trials and practice may now be warranted.

Identifying lesion Gd enhancement status without Gd injection in MS

Gd is relatively contraindicated in pregnant patients, those with a Gd allergy, and patients with renal failure, who are at risk for Gd-induced nephrogenic systemic fibrosis. Recently, the long-term safety of repeated Gd injections has undergone scrutiny by the FDA, given the accumulation of Gd in the brains of patients with normal kidney function (Kanda T et al 2015, Radbruch A et al 2015) (<http://www.fda.gov/Safety/MedWatch/SafetyInformation/SafetyAlertsforHumanMedicalProducts/ucm456012.htm>). Of particular concern is that Gd accumulation in MS brains seems to be associated with degradation into secondary progression (Roccatagliata L et al 2009). Though the long-term sequelae of Gd accumulation in the brain are uncertain, these new data have forced a critical reevaluation of the long-held assumption of the long-term safety of repeated Gd injections. Therefore,

alternative imaging strategies to accurately characterize MS disease activity without Gd should be actively investigated, established, and disseminated to the MS community (Treaba CA et al 2014). QSM may obviate Gd-enhanced MRI for MS. Contrast-enhanced MR can distinguish between acute (<1 month) lesions, which enhance due to local breakdown of the BBB, and chronic lesions, which do not enhance since their BBBs have been resealed. Recent work suggests that QSM can identify acute enhancing lesions without the use of Gd by their pattern of iron deposition and myelin debris removal (Zhang Y, Gauthier SA et al. *J. Magn. Reson. Imaging* 2016), which invariably occur after the BBB reseals (Zhang Y, Gauthier SA, et al. *Am. J. Neuroradiol.* 2016). QSM can accurately identify MS lesion Gd enhancing status (Zhang Y, Gauthier SA, et al *J Magn Reson Imaging.* 2016, Zhang Y, Gauthier SA, et al. *Am. J. Neuroradiol.* 2016), more accurately than previous efforts using relaxation or diffusion MRI (Blystad I, et al 2015, Shinoara et al 2021, Lo CP et 2014).

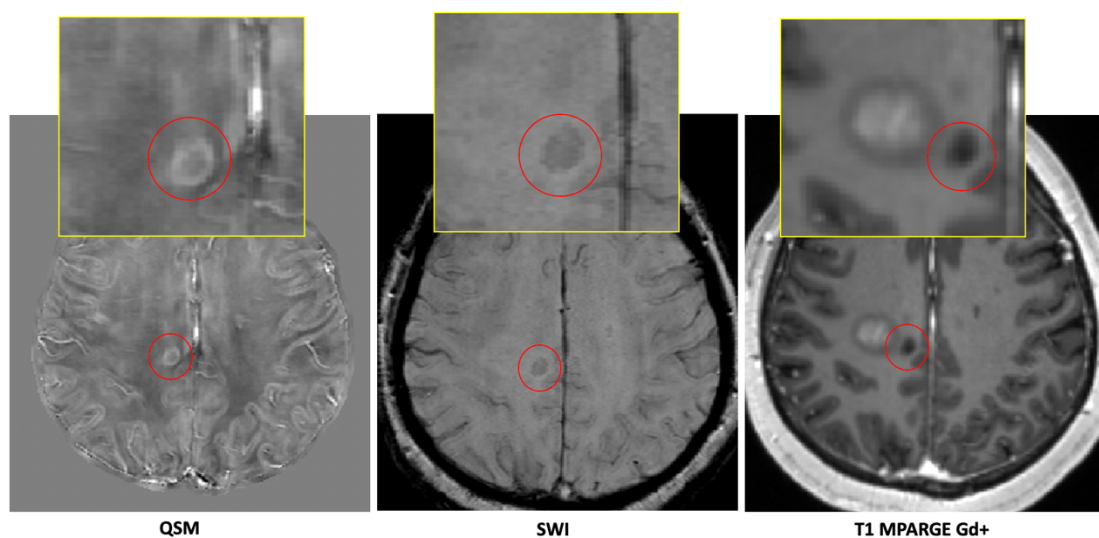


Fig 2.11 Chronic active multiple sclerosis (MS) lesions detected by QSM sequences. Hyperintense rime of iron-enriched activated microglia and macrophages on QSM image (left side), not clearly visible on SWI images (middle) and without Gd enhancement on T1 MPARGE (right side). *IRCCS Istituto delle Scienze Neurologiche di Bologna*

2.3.3 Iron in red blood cells: hemorrhage and oxygen consumption

The very high susceptibility of ICH (intracranic haemorrhage) presents an opportunity to further develop QSM (Sun H et al. 2016, Wei H et al. 2015). QSM has been used to study intracerebral hemorrhage, including measurement of hematoma volume (Wang S, Lou M et al 2013), differentiation from calcification (Schweser F et al. 2010, Chen W et al. 2014; Deistung A et al. 2013).

Iron and calcium both appear dark on SWI due to T2* effects, but distinguishing between blood, which contains iron, and calcium is necessary to better evaluate internal bleeding in calcified lesions

QSM, unlike other GRE-based imaging methods, easily distinguishes blood, which is bright (positive susceptibility value) on QSM, from calcium, which is dark (negative susceptibility value) on QSM (Schweser F et al. 2010 Chen W, Zhu W et al. 2014). This has been applied to characterize glioblastomas with oligodendroglial components (Deistung A, Schweser F et al. 2013) and dating of cerebral cavernous malformation lesions (Tan H Zhang L et al. 2016). QSM can also be used to measure the burden of cerebral microbleeds (CMB) (Liu T, Surapaneni et al 2012), which is a strong and independent risk factor for anticoagulant-associated ICH (Lee SH et al. 2009). In general, the long-term clinical risks and management in patients with microbleeds have yet to be defined. This remains an active area of investigation, where QSM could play an important role, particularly in longitudinal studies of microbleed burden (Liu W, Soderlund K et al. 2016). Moreover the ability to perform non-invasive CMRO₂ mapping could improve our ability to manage a variety of neurological disorders.

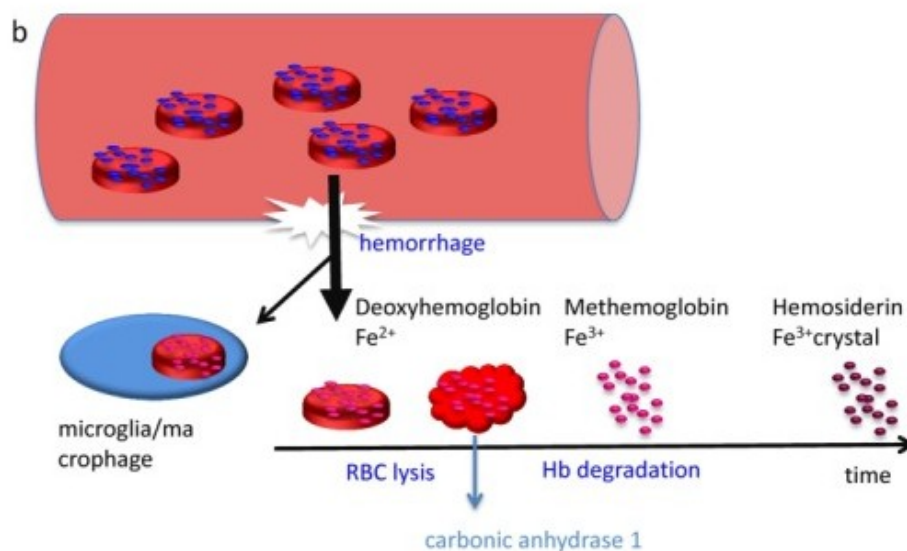


Figure 2.20: A scheme of blood degradation which occurs during a hemorrhage. Oxyhemoglobin, diamagnetic, carried by the red blood cells in a normal state, overflows changing its magnetic properties. It becomes deoxyhemoglobin, paramagnetic with 4 unpaired electrons per heme, methemoglobin, paramagnetic with 5 unpaired electron per heme, and hemosiderin, superparamagnetic with possible magnetic domain formation or ferromagnetic (Wang Y. and Liu T 2015).

Oxygenation

For example, close monitoring of central venous oxygenation is often used in critically ill patients with sepsis or cardiogenic shock, and in post-operative cardiac surgery patients. However, invasive monitoring with a central venous catheter can lead to infection, thrombus formation, and embolization.

Flow-compensated QSM sequences can be used not only to visualize veins, but also to measure venous susceptibility (Xu B, Liu T et al. 2014), which can be used to noninvasively calculate venous oxygen saturation level, SvO₂ (Wehrli FW et al 2016). SWI is very useful for its detailed depiction of veins, but the vein signal intensity on SWI (as well as on T₂ and T₂^{*}) varies both with the vein orientation and with echo time, and the underlying venous oxygenation cannot be derived (Haacke EM et al 2010). All these SWI limitations are addressed with QSM.

2.3.4 Iron deficiency

Lastly, QSM can be used to study brain iron deficiency in children ([Carpenter KL et al 2016](#)), in adults with restless leg syndrome ([Li X et al 2016](#)), and, potentially, to detect iron deficiency in the bone marrow, liver and other organs. Restless leg syndrome (RLS; Willis-Ekbom disease) is a syndrome characterized by an irresistible urge to move the legs, is a neuro-sensorimotor disorder associated with iron deficiency, with iron levels decreased in the substantia nigra, thalamus, putamen, and pallidum. QSM may offer a new reference means for non-invasive detection of iron deficiency that can avoid the confounding effects of inflammation, infection, and malignancy on currently available biomarkers.

2.3.5 Calcium

QSM has been used not only to study calcification in tumors ([Wang Y, Liu T et al. 2015](#), [Deistung A et al. 2013](#)) and to resolve hemorrhage from calcification. QSM of arterial calcification could have an emerging role in quantifying calcification in arterial beds, including in the coronary arteries where calcium scores have been shown to be a highly predictive measure of overall cardiovascular risk. Among patients with significant plaques, using QSM to differentiate calcium from hemorrhage may great clinical impact because intraplaque hemorrhage is a potential trigger of plaque vulnerability ([Michel JB, Virmani R et al. 2011](#)) while calcification may be an indicator for plaque stability ([Wu B, Pei X, et al. 2014](#)).

3. STUDY INTRODUCTION

Differential diagnosis between Parkinson's Disease (PD) and Atypical Parkinsonisms (AP) remains challenging, mainly in the early phases of the disease, as illustrated by a significant number of patients with an incorrect clinical diagnosis in these histo-pathological studies ([Koga S et al. 2015](#), [Miki Y et al. 2019](#)). An early accurate diagnosis helps to choose the optimal therapeutic decisions. The increasing prevalence of parkinsonian disorders, partly due to population's longevity, motivate the introduction of experimental therapeutic strategies and technological advances in data analysis (i.e. deep learning) that stimulate the development of novel biomarkers.

Until recently, standard MRI techniques had a marginal role in the diagnosis and follow-up of parkinsonian syndromes. Indeed conventional MRI signs described in parkinsonisms showed high specificity but low sensitivity, giving a limited support to clinical diagnostic criteria ([Massey LA et al. 2012](#); [Meijer FJA et al. 2015](#)). The main purposes of imaging neuroscience actually is to identify biomarkers that can aid in diagnosis, disease progression monitoring and long-term drug impact analysis. Biological markers, or biomarkers, are quantitative measurements that provide information about biological processes, a disease state, or about response to treatment, providing much-needed insight into preclinical and clinical data ([FDA's Biomarkers Definitions Working Group](#)). Brain MR imaging enables to better understand the pathological changes of nigral and extranigral structures during the course of the diseases. Even if both PD and MSA are synucleinopathies, in MSA the degenerative process mainly involves the dorsolateral pars of the putamen (clinical phenotype p-MSA) and pons, the medium cerebellar peduncles (MCP) and the cerebellum (clinical phenotype c-MSA) ([Halliday et al. 2011](#)).

Idiopathic Parkinson's disease (PD) is a common progressive degenerative disorder characterized pathologically by proteinaceous aggregates of α -synuclein in the form of Lewy bodies and Lewy neurites.

These are thought to occur early in the brainstem, gradually spreading across vulnerable sites in the allocortex and temporal paralimbic cortex before reaching prefrontal and sensory association isocortex ([Braak et al. 2003](#)). It is postulated that projection neurons (with disproportionately long, thin and poorly myelinated axons) are particularly susceptible to degeneration in Parkinson's disease ([Braak et al., 2003](#)), of which the most studied to date have been the neuromelanin-pigmented dopaminergic neurons of the basal ganglia. The motor dysfunction in Parkinson's disease related to nigrostriatal degeneration is only one aspect of this multi-faceted disease that includes numerous non-motor manifestations.

Multiple system atrophy (MSA) is a sporadic, adult-onset, relentlessly progressive neurodegenerative disorder, clinically characterized by various combinations of autonomic failure, parkinsonism and ataxia. The neuropathological hallmark of MSA are glial cytoplasmic inclusions consisting of misfolded α -synuclein. Selective atrophy and neuronal loss in striatonigral and olivopontocerebellar systems underlie the division into two main motor phenotypes of MSA-parkinsonian type and MSA-cerebellar type. Isolated autonomic failure and REM sleep behavior disorder are common premotor features of MSA. Beyond the core clinical symptoms, MSA manifests with a number of non-motor and motor features. Red flags highly specific for MSA may provide clues for a correct diagnosis, but in general the diagnostic accuracy of the second consensus criteria is suboptimal, particularly in early disease stages. The current challenge in neuroimaging is focused on research of biomarkers, trying to diagnosis early ([Fanciulli A et al. 2019](#)).

Rem Behavior disorder (RBD) has emerged in recent years as one of the most promising markers of prodromal Parkinson's, since its first description in 1986 by Dr. Carlos Schenck, and his group's subsequent report of the delayed emergence of a Parkinsonian disorder in idiopathic RBD patients one decade later ([Boeve, B.F. et al. 2010](#))

RBD is present in 25–58% of patients with Parkinson's disease and up to 90% of those with Dementia with Lewy Bodies (DLB) or Multiple System Atrophy (MSA). In a substantial proportion of these patients RBD onset occurs before motor symptoms. Critically, when seen in isolation, RBDi (RBD idiopathic) is a highly specific marker of future synucleinopathy: long-term cohort studies indicate that more than 80% of people who develop isolated RBD will go on to develop an alpha-synuclein related neurodegenerative disorder. RBDi ultimately represents and provides a unique window for the study of prodromal neurodegeneration, whether it be Parkinson's disease.

Impairment of the substantia nigra (SN) is common to some AP, however the neuronal loss in the pars compacta (SNpc) proceeds with different patterns: the lateral part of the ventral layer of SNc is the most affected in PD, the medial part is more affected in other parkinsonian disorder PSP (Progressive Supranuclear Palsy) (Fearnley and Lees, 1991).

Even if it is still under debate whether iron accumulation represents a cause or a consequence of neurodegeneration, specific patterns of iron deposition, different from physiological age-related changes, have been described in different neurodegenerative disorders including PD and AP. Increased total iron levels were demonstrated in the SN of PD, MSA and PSP patients (35%, 59% and 70% respectively, compared to control subjects) and in the striatum of MSA and PSP subjects (Dexter et al. 1991).

The increasing interest for selective iron deposition in neurodegenerative diseases encouraged the use of Susceptibility Weighted Imaging (SWI) (Liu et al., 2015). Magnetic susceptibility (χ) is a physical property that in brain tissues is mainly related to ferritin and myelin content.

Quantitative in vivo imaging of tissutal χ could be a promising approach for differential diagnosis in particular by applying a recently established post-

processing technique, namely Quantitative Susceptibility Mapping (QSM) (Wang Y et al. 2015).

The Nigrosome-1 (N1) is a substructure of the healthy Substantia Nigra pars compacta (SNpc) enriched by dopaminergic neurons; their loss in Parkinson's disease and atypical parkinsonian syndromes is related to the **iron** accumulation. N1 changes are supportive MR biomarkers for diagnosis of these neurodegenerative disorders, but its detection is hard with conventional sequences, also at 3T. Quantitative susceptibility mapping (QSM), an iron-sensitive technique, enables the direct detection of N1 (Fig. 3.1 yellow arrows) (Robinson et al. 2017)

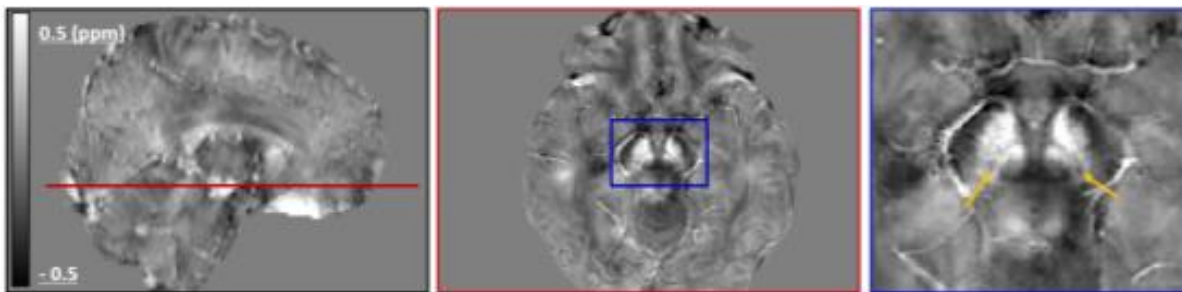


Fig 3.1 : Nigrosome-1 in Quantitative Susceptibility Map

Primary objective of our study was to compare, at high magnetic field strength, quantitative susceptibility values of the main brain regions affected by the neurodegenerative process in patients with PD, MSA and RBD in order to evaluate the potential utility of the QSM technique, as biomarker, for differential diagnosis.

For this purpose this study also aimed to investigate role of conventional MR study and possible correlations between MR findings, magnetic susceptibility values and clinical data.

4. MATERIALS AND METHODS

4.1 Study Population

All participants of this study gave written informed consent to data processing for research purposes. We enrolled consecutive 67 patients referred to the tertiary Movement Disorder Center “Neuromet Unit”, IRCCS Istituto delle Scienze Neurologiche di Bologna, from June 2020 to June 2021, with a clinical diagnosis of probable PD, MSA or RBDi. We enrolled patients until June 2021 since the clinical follow-up of patients between June and January 2022 is in progress. The clinical diagnosis was made on the basis of Gelb’s criteria (Gelb DJ et al 1999). Unified Parkinson Disease Rating Scale, Part III (UPDRS III) and Hoehn and Yahr (H&Y) scale [Hoehn and Yahr, 1967] were recorded to evaluate the severity of motor symptoms. MSA diagnosis was made in according with second consensus criteria for MSA (Gilman S et al. 2008). Patients with MSA were further classified as MSA with predominant parkinsonism symptom’s (MSA-P) and MSA with predominant cerebellar ataxia (MSA-C). Idiopathic REM Sleep Behavior Disorder (RBD) was diagnosed by clinical assessment coupled with a subsequent overnight video polysomnography (v-PSG) study, according to diagnostic criteria of the International Classification of Sleep Disorders (3rd Edition) (ICSD-3) (Seteja M 2014).

We studied a population of 67 patients: 41 PD (19 F, 22 M; mean age: 60.9 a \pm 7.5 y, range 43-71), 12 were affected by MSA (6 M, 6F, mean age 66.9 \pm 8,8y, range 55-78), 14 had a diagnosis of RBD (14 M; mean age 67.2 \pm 8,2 y, range 55-82). Exclusion criteria for all three groups were: uncertain clinical diagnosis with undetermined parkinsonism or history of another neurodegenerative disorder, the presence of cognitive impairment that could compromise the understanding of the informed consent or interfere with imaging protocol acquisition, the presence of

infarction, hemorrhage, tumors or trauma or severe white matter lesion load measured by means of Age-Related White Matter Changes score (AWRMC) (Wahlund et. al 2001) that classifies changes from absent to severe (scale point from 0 to 3). We exclude patients with ARWMC score >2 , claustrophobia or any contraindications to perform MR investigation.

4.2 Clinical Evaluation

Patients were evaluated by two neurologists with experience in movement disorders within two weeks from the MRI scan. Clinical recordings included main demographic and disease related data such as duration, clinical phenotype and prevalent affected side. Motor assessment was performed in the whole study population in the OFF and ON state by means of the III sub-scores of the UPDRS. Even if this scale is not designed for the clinical evaluation of MSA patients, it was applied to compare disease severity among the three groups. In the PD group the Hoehn and Yahr (H&Y) score was recorded and clinical sub-scores were calculated as a result of tremor, rigidity and bradykinesia items of the UPDRS III for each side. Moreover, PD patients were categorized on the basis of the clinical phenotype into Tremor Dominant (TD) or AR (akinetic rigid) and Tremor Dominant/mixed/akinetic (TD or AR) (Konno T et al. 2018). Moreover, cognitive profile evaluation (MMSE: Mini Mental State Examination) and RBD status as absent, probable or present in PD and MSA patients were also assessed.

4.3 Brain MR Image Protocol Acquisition

All MR examinations were performed on a high field 3.0-T scanner (Siemens Magnetom Skyra VEC11C-SP01) equipped with a 64-channel Head/Neck 64-channel coil as receiver. The MRI conventional protocol were also acquired before the QSM sequence, in order to exclude other diseases and significant

comorbidities, in particular vascular damage, hydrocephalous or brain tumors, that could be responsible for the symptoms or that could interfere with susceptibility measurement.

The conventional protocol included volumetric T1-weighted imaging based on 3D MPRAGE [176 continuous sagittal slices, 1-mm isotropic voxel, no slice gap, echo time (TE) = 2.98 ms, repetition time (TR) = 2,300 ms, Inversion Time (IT) = 900 ms, flip angle = 9 °, acquisition matrix = 256 × 256, pixel bandwidth = 240 Hz, in-plane acceleration factor = 2, duration 5.21 min] and volumetric fluid-attenuated inversion recovery (FLAIR) T2- weighted imaging (3D SPACE, 176 sagittal acquisition slices, 1- mm isotropic voxel, no slice gap, TE = 428 ms, TR = 5,000 ms, IT = 1,800 ms, flip angle = 120° , acquisition matrix = 256 × 256, pixel bandwidth = 780 Hz, in-plane acceleration factor = 2, duration 5.55 min).

All sequences were scanned using axial sections parallel to the anterior commissure–posterior commissure (AC-PC) line with whole-brain coverage.

For the qualitative evaluation of deep brain nuclei, a 3D multi-echo GRE sequence (Susceptibility Weighted Imaging -SWI) targeted on the midbrain was included in the protocol: TR = 28 ms, average TE = 20 ms, FA = 15 degree, number of excitations (NEX) = 1; spatial resolution acquisition= 0.71x0.54x2.14 mm³; spatial resolution reconstruction = 0.5x0.5x1.5 mm³, scan duration = 4 min 38''.

4.4 QSM: Sequence processing and optimization

Before the application of the QSM sequence for the study of patients, the first our aim was its optimization on a sample of healthy controls in order to visualize N1 using the same MRI equipment, Siemens Magnetom Skyra 3T, VEC11C-SP01, and Siemens Head/Neck 64-channel Coil as receiver. Between November 2019 and February 2020 three healthy subjects, one male (M/29 years), and 2 females (46 and 20 years,), age 31.7 ±13.2) have been evaluated. All subjects gave consent to data processing for research purposes. Exclusion criteria for enrollment

were as follows: (1) sleep disorders, such as obstructive sleep apnea or insomnia; (2) neurological diseases (epilepsy, head injury, etc); (3) psychiatric disorders; (4) alcohol, or substance abuse, current intake of psychoactive medications; (5) congenital or inherited diseases, chronic pulmonary/respiratory disease, or heart disease; (6) MRI contraindications, such as claustrophobia or metal implants; and structural brain lesions based on MR imaging.

3D GRE multi-echo T2*-w images were acquired. The phase maps were processed by Laplacian unwrapping [Robinson et al., NMR Biomed (30), 2017] and V-SHARP background field removal (Deistung et al 2017) (Fig. 4.1, A-C).

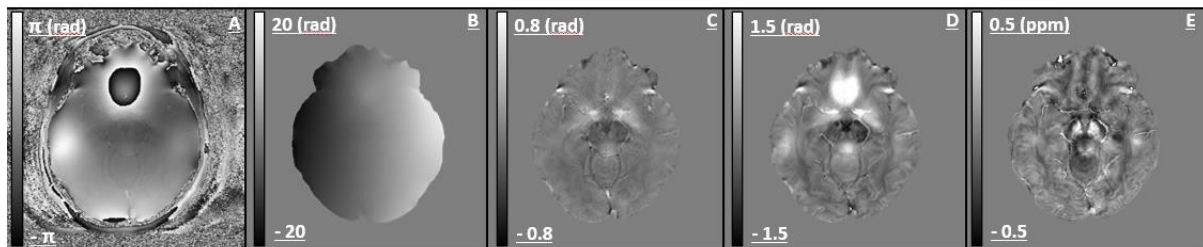


Fig. 4. 1 Phase and quantitative susceptibility maps from a 5TEs GRE acquisition. A) Raw phase data from 1st TE. B-C) processed phase maps, respectively after the unwrapping and the background field removal . D) Single-phase map as result of multi-echo map combination. E) QSM, evaluated with iLSQR technique *IRCCS Istituto delle Scienze Neurologiche di Bologna*.

Multi-echo phase data were combined into a single-phase image through a weighted-sum over echoes of processed phase maps (Lu W et al. 2012) (Fig. 4.1 D). The iLSQR technique was used as dipole inversion method (Li et al. 2015) (Fig. 4.1 E).

Different measurements were performed, changing spatial resolution, number and values of echo times and coil combination method:
a) 2 TEs (TE1/ΔTE/TR=9.42/9.42/27 ms) and spatial resolution 1x1x1,

0.8x0.8x1.5, 0.5x0.5x1.5, 0.5x0.5x1 mm³, ASPIRE (Ekstein K et al 2018) as coil combination method (scan time ~ 3,4,5,7 mins respectively)

b) 5 TEs and spatial resolution 0.5x0.5x1.5 mm³ (TE1/ΔTE/TR=9.42/9.42/53 ms, ~9 mins), using both ASPIRE, manually implemented, and the ADAPTIVE combination method (Walsh DO et al. 2000), automatically performed by the scanner

c) 8 TEs (TE1/ΔTE/TR=5.6/5.6/51ms) and spatial resolution 0.8x0.8x1.5 mm³ (scan time ~ 7 halving the number of axial slices). N1 and SN were manually segmented and the Contrast-to-Noise Ratio (CNR) N1-SN in susceptibility χ maps was evaluated, with 0.5 as estimated error:

$$CNR = |\langle \chi_{N1} \rangle - \langle \chi_{SN} \rangle| / \sqrt{N1 - SN} \sigma^2$$

We obtained a final scan duration was: 8, 45'.

4.4.1 Nigrosome-1 Detection in Quantitative Susceptibility Mapping: Contrast Optimization with 64-channel Coil

a) 2TEs: N1 was visually detected only with in-plane resolution 0.8x0.8 and 0.5x0.5 mm² (Fig. 4.2 A), the returned CNR values were respectively 1.5 and 6.1. Decreasing the slice thickness from 1.5 to 1 mm, the scan time increased and CNR worsened.

b) 5TEs: N1-SN CNR values were 6.9 with ASPIRE and 8.7 with ADAPTIVE (Fig. 4.2B).

c) 8TEs: in-plane spatial resolution was decreased from 0.5x0.5 mm² to 0.8x0.8 mm², to reach a good compromise between N1- SN contrast and the scan time (Fig. 4.2 C). Despite of the general improvement of the map contrast due to the number of echo times, the worsening of the spatial resolution affected the N1-SN CNR results. The evaluated CNR values were 2.7 and 2.4 using respectively ASPIRE and ADAPTIVE.

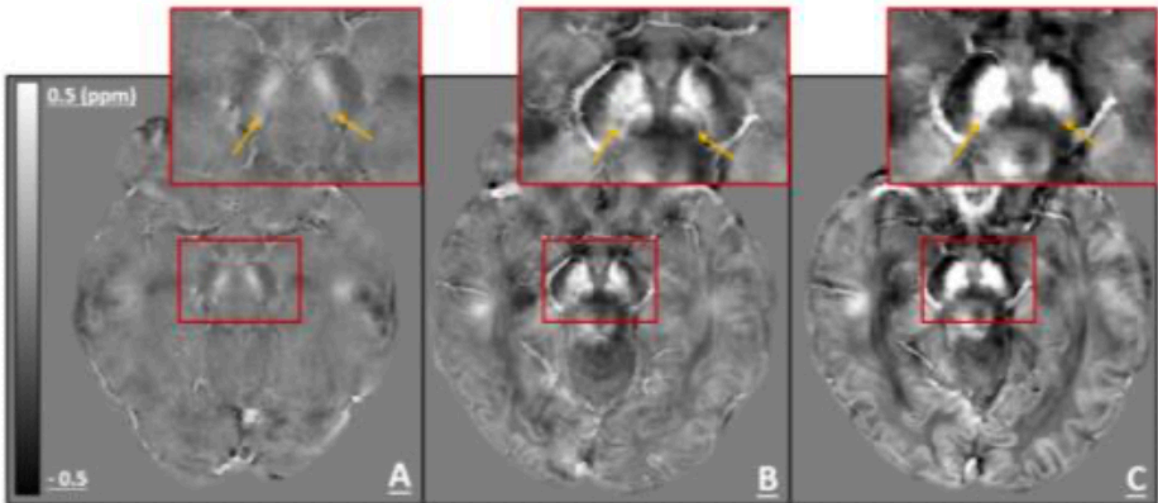


Fig. 4.2: Axial view with SN and N1 of QSM maps: A) 2TEs, spatial resolution $0.5 \times 0.5 \times 1.5 \text{ mm}^3$, ASPIRE; B) 5TEs, spatial resolution $0.5 \times 0.5 \times 1.5 \text{ mm}^3$, ADAPTIVE; C) 8TEs, spatial resolution $0.8 \times 0.8 \times 1.5 \text{ mm}^3$, ADAPTIVE. *IRCCS Istituto delle Scienze Neurologiche di Bologna*

CNR values are summarized in Fig. 4.3

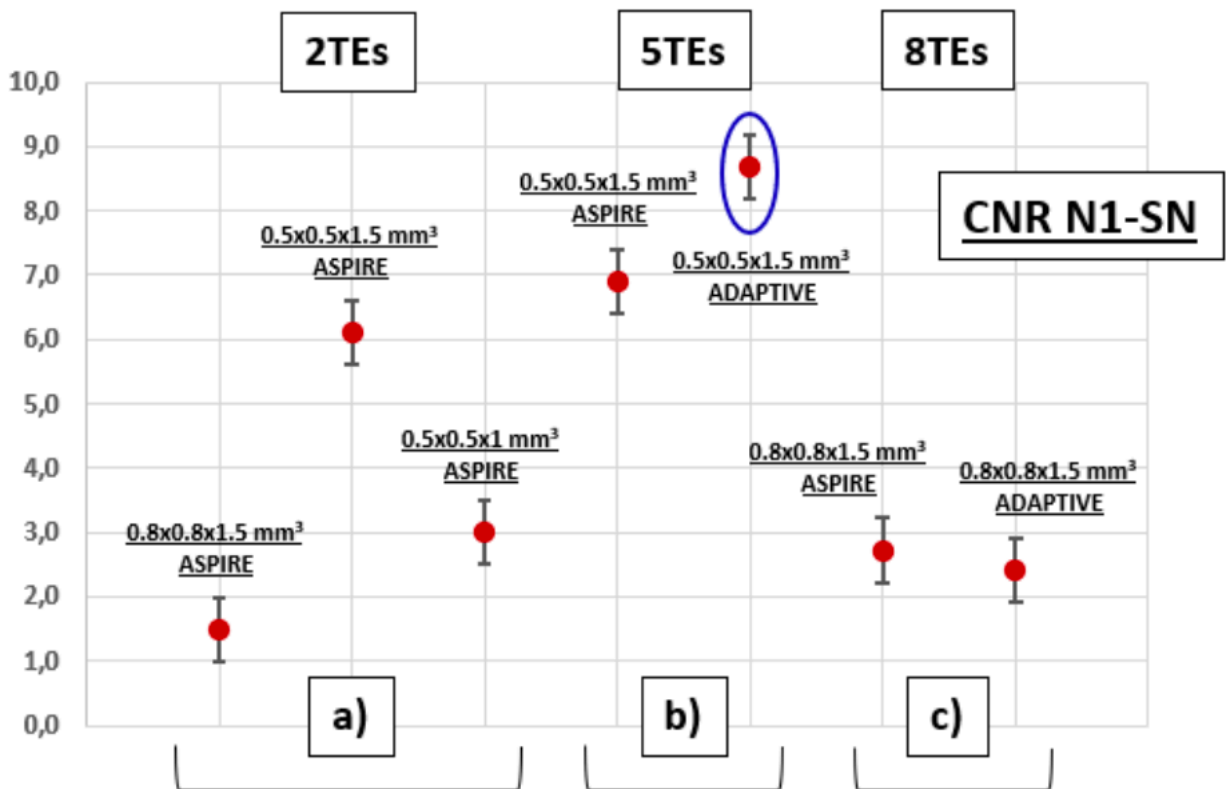


Fig. 4.3 CNR (N1-SN) values for the implemented QSM sequences.

Definitely the optimal protocol for quantitative susceptibility map reconstruction was obtained (3T Siemens Head/Neck 64 Coil) maximizing the contrast of Nigrosome-1 in Substantia Nigra. The best CNR N1-SN has been achieved with $0.5 \times 0.5 \times 1.5 \text{ mm}^3$, 5 TEs ($TE1/\Delta TE/TR=9.42/9.42/53 \text{ ms}$) and the ADAPTIVE coil combination method. ([Fiscone C et al. 2020](#))

4.5 Image analysis

4.5.1 Qualitative visual assessment

a) Definition of Nigrosome 1 (and Nigrosome 4)

Two neuroradiologists with 3 and more of 10 years of experience blinded to clinical information assessed the MR images of the SN of each subject and of 14 healthy controls N1 region was identified as hypointensity on QSM imaging. According to a previously validated protocol, identified on SWI images ([Cosottini M. et al 2014](#), [Cosottini, M. et al 2015](#)), the nigral anatomy was evaluated on both sides along the rostro-caudal axis at the level of the inferior third of the RN (level I) and at the level of the superior cerebellar peduncles decussation (level II). SN anatomy was considered normal (on QSM images) if characterized at level I by a medial homogeneous hyperintense region and by a lateral hypointense area (nigrosome 1) between two hyperintense layers, and if a trilaminar organization (central hypointense layer between two hyperintense laminae was detectable at level II. It was considered abnormal when the hypointense lateral spots at level I or the three-layered organization at level II were absent in at least one side of the midbrain.

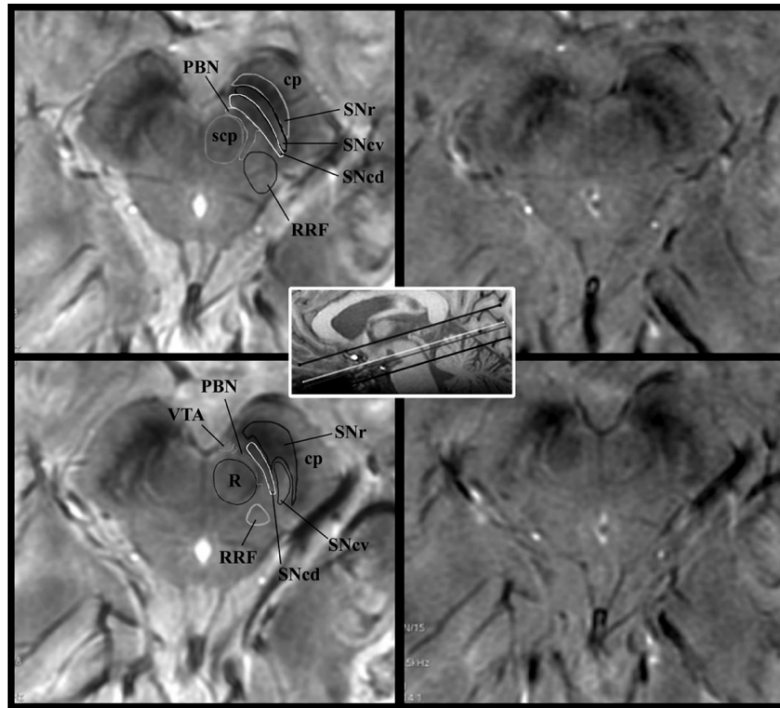


Fig 4.4 SWAN-targeted axial image of the midbrain in a healthy subject evaluated at 3T (right column) and at 7T (left column). The trilaminar organization of the SN at level II (upper row) and the nigrosome formation at level I (lower row) are clearly shown with 3T and 7T magnets. Levels I and II of image acquisition are represented by *white* and *gray lines* in the scout strength magnets. cp indicates cerebral peduncle; PBN, parabrachial nucleus; RRF, retrorubral field; scp, superior cerebellar peduncle; SNcv, substantia nigra pars compacta ventralis; SNcd, substantia nigra pars compacta dorsalis; SNr, substantia nigra pars reticularis; VTA, ventral tegmental area; R, red nucleus. (Cosottini 2015).

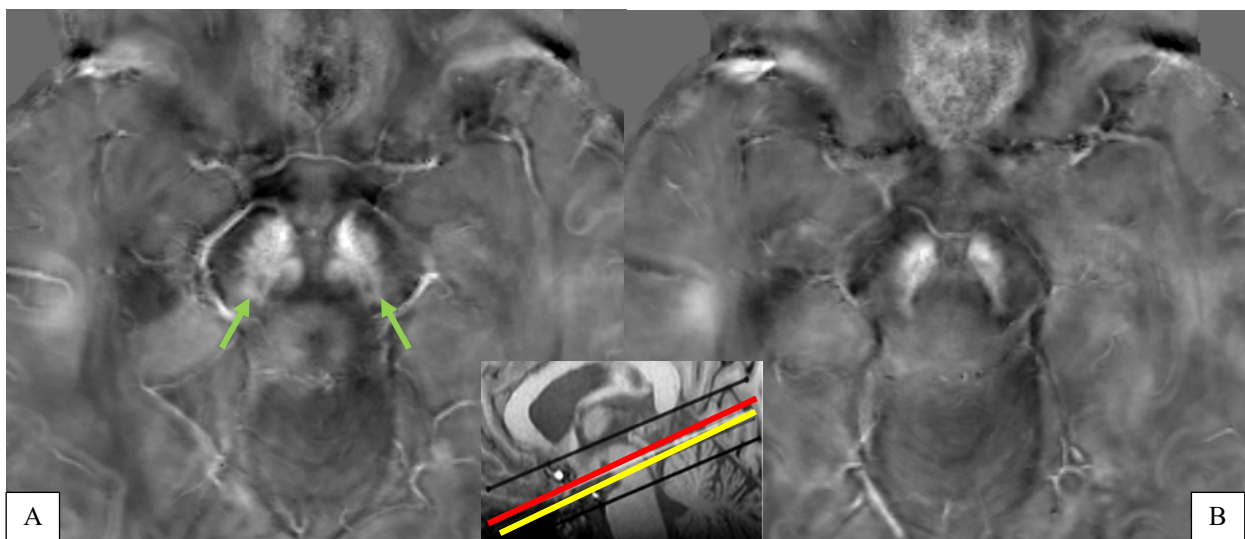


Fig 4.5 QSM axial image (0.5x0.5x15mm) of the midbrain (bicommissural plane) in a healthy subject evaluated at 3T. A) Nigrosome formation at level I (red upper row) and B) the trilaminar organization of the SN at level II (lower yellow line). Levels I and II of image acquisition are represented by red and yellow lines in the sagittal scout (middle). IRCCS Istituto delle Scienze Neurologiche Bologna.

Moreover we aimed to distinguish nigrosomal subregions likely involved in different stages of PD disease, as preliminarily indagated in a previous study (Sung et al 2018), based on the histologically validated anatomical description of the substantia nigra in five nigrosomes, using high field spin-echo high resolution magnetic resonance image (Massey LA et al 2017).

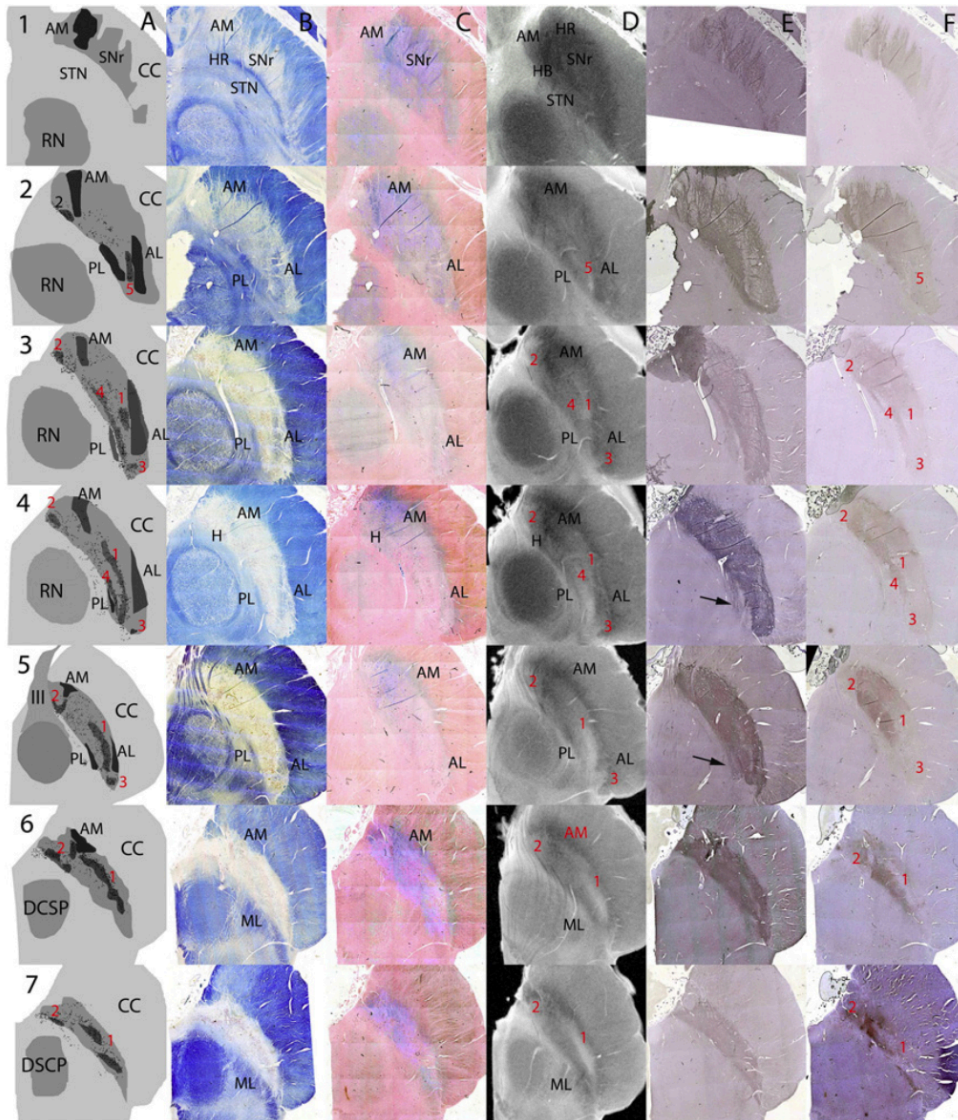


Fig. 4.6. The Anatomy of the SN on serial axial sections using different Luxol fast blue/Cresyl Violet (LFB/CV), Perls stain, high field spin-echo MRI, and substance P (SP) and calbindin (CB) immunohistochemistry. Serial axial sections at 1.5 mm through a single substantia nigra (SN). Nigrosomes (1–5) are labelled in red; on the third and fourth line nigrosome 1 and 4. Nigrosome 4 appeared as a hyperintense band posterior to N1 and bounded by the signal hypointensity of the parabrachial nucleus immediately adjacent.

A: cartoon showing key anatomical structures based on SP and LFB/CV for borders, LFB/CV for location of pigmented neurons on substantia nigra pars compacta (SNc) and CB for nigrosomes. Pigmented neurons are shown as black dots and it is notable that not all of these fall within the CB-defined nigrosomes. B: LFB/CV. C: Perls stain. D: High field spin-echo MRI. E: SP. F: CB. Anatomical landmarks are in black. Nigrosomes (1–5) are labelled in red. (Massey 2017)

Accordingly to the histopathological findings, on axial QSM images, unlike nigrosome 1 below the red nucleus it was well detected (fig 4.6 row 5 and 6), the border between nigrosome 1 and the putative nigrosome 4 was unclear, at the level of lower one-third of the red nucleus (fig 4.6 row 3 and 4). Thus, in order to distinguish both subregions, we designated as the putative nigrosome 4, the hypointense region located in the medial half of the SN at the level of lower one-third of the red nucleus, on coronal-reformatted images (i.e., a craniomedial component of the dorsal nigral hyperintensity) and was assessed on coronal-reformatted images as well, covering the anterior two-third of the red nucleus (Fig. 4.7). This method has allowed to better appreciate the nigrosome in its cranio-caudal extension with putative differentiation of two subregions (N1 and N4).

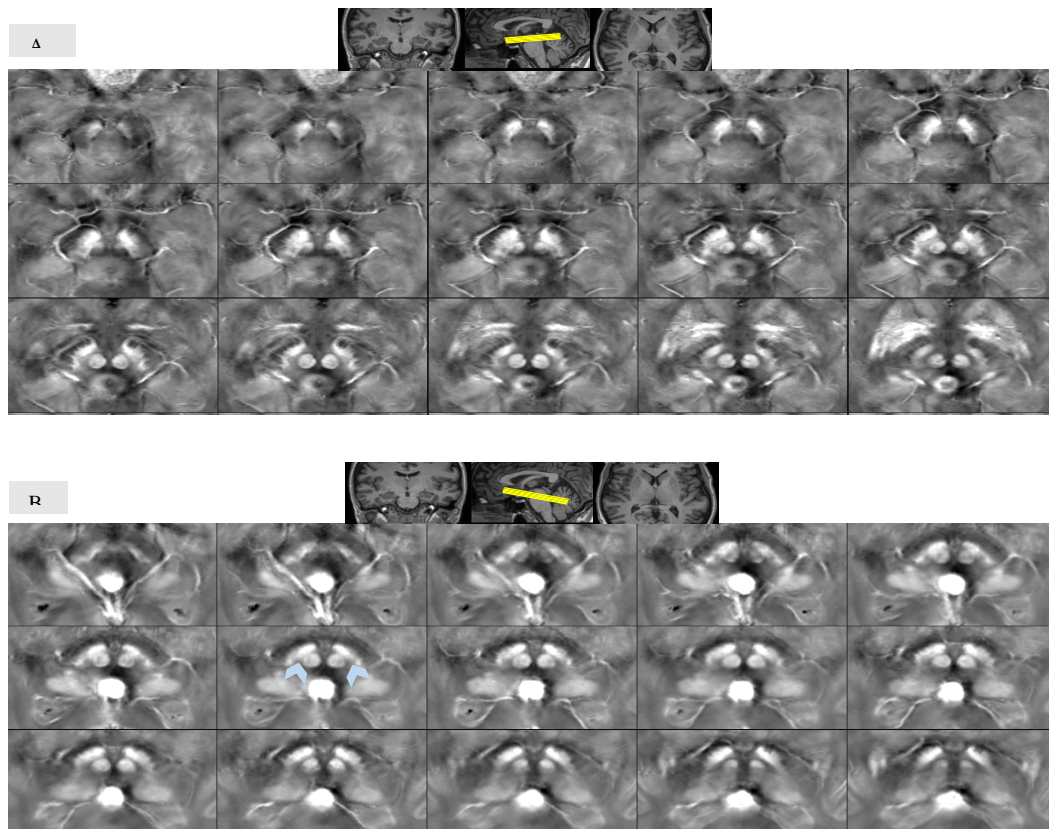


Fig 4.7 Bicommissural (A) and oblique coronal (B) quantitative susceptibility map-weighted images of a 46-year-old healthy control female (A) Axial obtained parallel to the bicommissural line (yellow lines) (AC: anterior commissure e PC posterior commissure) including all red nuclei region until to the lower border. (B) Oblique coronal plane : the same images was resliced with an increment of 0.5 mm on this plane (yellow lines on sagittal scout). Note the putative bilateral nigrosome 4 region (light blue arrowheads): is better delineated because this reconstruction is able following nigrosomial structure along cranio-caudal extension. *IRCCS Istituto delle Scienze Neurologiche Bologna.*

b) Imaging evaluation of nigrosome 1 score between three groups

A total of 48 participants with an acceptable quality of QSM images were included in this evaluation. Due to the higher number of PD patients with respect to the other groups; we selected a reduced sample of 22 patients for comparison measurements.

The sample included 22 PD, 12 MSA and 14 RBD patients. Two radiologists (with three and ten years of experience in neuroradiology), both blindly to the clinical diagnosis, independently evaluated the STS (*swallow tail sign*) in each hemisphere on QSM images.. Three continuous axial slices with the most superior layer at the level of the inferior tip of the red nucleus were chosen for the evaluation of STS. The inter-rater reliability was assessed as well. In cases where the evaluators disagreed, a consensus was reached and used in the following analysis.

We used an STS (Loss of swallow tail sign) (Liu X et al 2020) score in the range of 0–2 (representing 0= “total loss”, 1= “partial loss/blurring margin” and 2= “normal”) on QSM images to assess the STS in each hemisphere.

We used an STS scale in the range of 0–4 by summing bilateral STS scores at participant level. STS score in the range of 0–2 was applied to evaluate the STS in each hemisphere (Figs 4.8, 4.9), 0: absence of hypointensity in the SN on three slices (represents total loss of STS); 1: blurring margin and decreased hypointensity but still visible on one slice (represents partial loss of STS); and 2: presence of hyperintensity in the dorsolateral SN with oval or linear appearance visible on at least two slices (represents normal STS). The nigrosome total score derived from right and left score sum indicates the global evaluation of both sides. The higher the nigrosome score, the more the intactness of nigrosome-1 in participants.

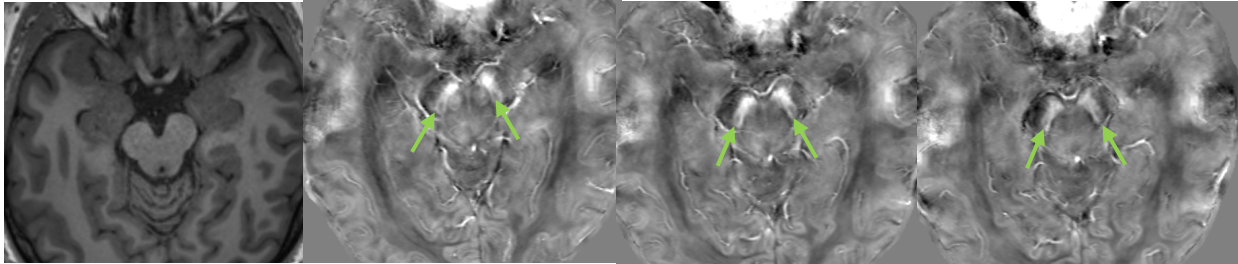


Fig 4.8 The criteria for rating STS scale (nigrosome score) on QSM within three continuous slices. A 41-year-old male HC. Normal nigrosome aspect on both side, total nigrosome score: 4 (R:2+L:2). R: right; L: left. *IRCCS Istituto delle Scienze Neurologiche Bologna*

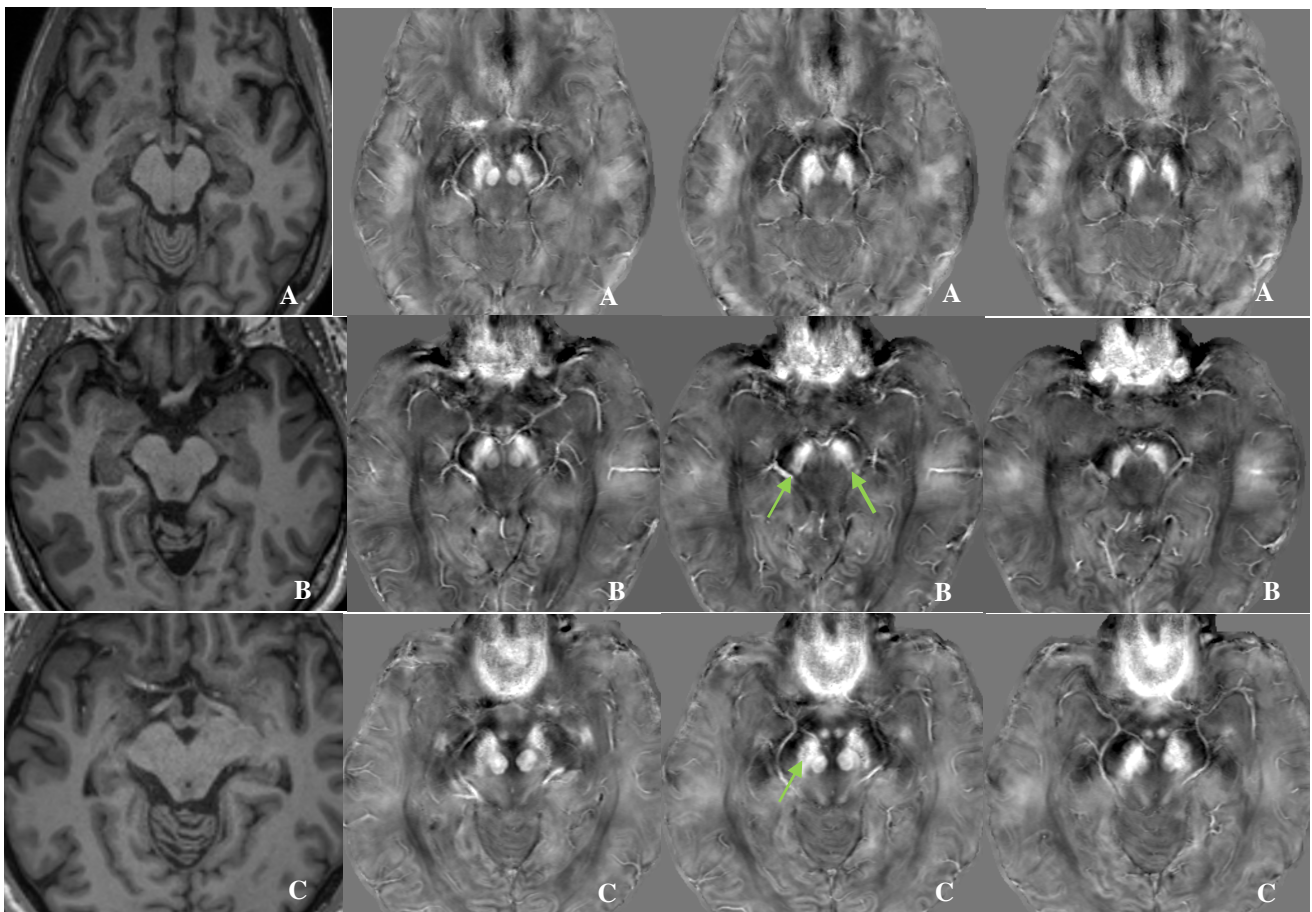


Fig 4.9 The criteria for rating STS on QSM within three continuous slices. (A1-A4) a 55-year-old male patient with PD, rating bilateral total loss of STS. Total nigrosome score: 0; (B1-B4) a 55-year-old male patient with RBD rating bilateral blurring STS. Total nigrosome score R:1+L:1= 2 (green arrow); (C1-C4) a 57-year-old female with MSA, rating STS R: 2 (green arrow) and L: 0 Total Nigrosome score: 2. PD Parkinson disease, RBD Rem Behaviour Disease MSA, Multiple system atrophy R: right; L: left. *IRCCS Istituto delle Scienze Neurologiche Bologna*

c) Definition of putaminal hypointensity and putamen score

From a sample of 67 patient- 41 PD, 12 MSA, and 14 RBD- we excluded respectively six PD, one MSA and two RBD patients, because of the absence of SWI sequences. We finally analyzed 35 PD (15 F, 20 M; mean age: 60.9 ± 7.8 years, range 43-71), 11 MSA (5 M, 6F, mean age 67.3 ± 9.2 years, range 55-78) and 12 RBD (12 M; mean age 68.3 ± 8.0 years, range 55-82).

The hypointensity of posterolateral putaminal nuclei in all groups was measured on SWI images according to a grading scale based on the comparison of signal intensity (SI) of regions of interest (ROIs) placed on these nuclei respect to the SI of the cerebrospinal fluid (CSF) and vein of Galen ([Gupta et al. 2010](#)).

For calculating the SI, mIP image of the SWI slice in which the nucleus was best visualized was chosen. The more hypointense nucleus of the two sides was chosen for ROI placement. ROI was then placed in the most hypointense part of the nucleus in that slice. Based on the SI values obtained, the putaminal hypointensity was graded as follows: Grade 0: SI similar to CSF intensity ($SI > 200$) Grade 1: mild hypointensity ($SI > 150$ but less than 200) Grade 2: moderate hypointensity ($SI > 75$ but less than 150) Grade 3. severe hypointensity ($SI < 75$, similar to vein of Galen). (fig 4.10).

Size of ROIs of the four nuclei was similar among all study subjects.

Visual grading of hypointensity of deep gray matter nuclei has been used previously for SWI ([Harder SL et al 2008](#)).

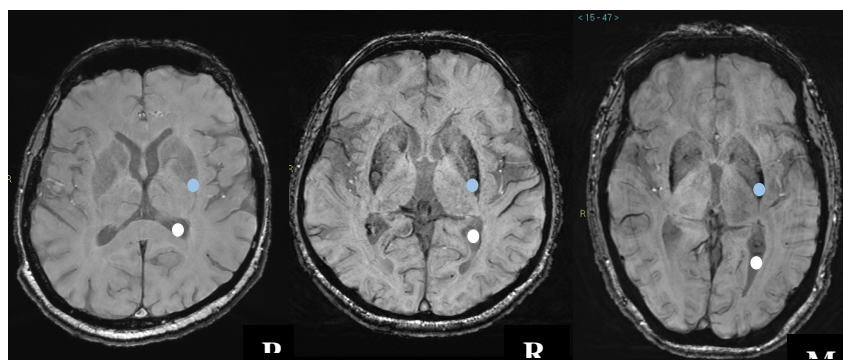


Fig. 4. 10 Increasing grades of putaminal (light blue oval) hypointensity in SWI vs CSF (white oval) in three patients subgroup vs CSF (white oval): PD (M/71y), Grade 0, RBD (M/71y) Grade 2, MSA (F/73y) Grade 3.

4.5.2 Quantitative imaging analysis

Volumetric T1w images were processed using FSL-FIRST (<https://fsl.fmrib.ox.ac.uk/fsl/fslwiki/FIRST>), a segmentation/registration tool. We selected some deep Gray Matter nuclei and structures: Caudate, Hippocampus, GP, Putamen and Thalamus.

QSM maps were linearly registered to T1w maps (FSL-FLIRT), so susceptibility properties of the so-segmented structures were analyzed. (Figs 4.11, 4.12).

Selection of ROIs was done according the patterns of movement disorders neurodegeneration described in neuropathologically confirmed cases (Dickson, 2012; Halliday et al., 2011; Williams et al., 2007). A limited number of extranigral regions was included taking into account the results of previous qualitative and quantitative MR studies investigating PD patients respect to HC ([Barbosa et al., 2015](#); [Murakami et al., 2015](#)).

Therefore Substantia Nigra (SN), Red and Dentate nuclei (RN, DN), which are not included in the analysis provided by other automatic tools, were segmented with the following semi-automatic method. QSM maps from the 15 healthy controls were registered to the MNI atlas, setting up an atlas with susceptibility contrasts on which SN, RN and DN was clearly detected. ROIs in all structures were manually drawn on the atlas and then registered back on the original acquisition space for each subject, healthy or patient. Back-registered ROIs needed to be a slight manual adjustment (Fig 4.13).

For each structure we evaluated: 1) median χ value (ppm) 2) 90^o-percentile χ percentile value (ppm) 3) volume, corrected for brain volume using proportional method ([Sanchis-Segura C et al. 2019](#)): volume (a.u)

$$v_{structure}(a. u.) = \frac{v_{structure}(mm^3)}{v_{brain}(mm^3)}$$

For differentiating non-normal distributions we chosen 90°-percentile χ -percentile value (ppm).

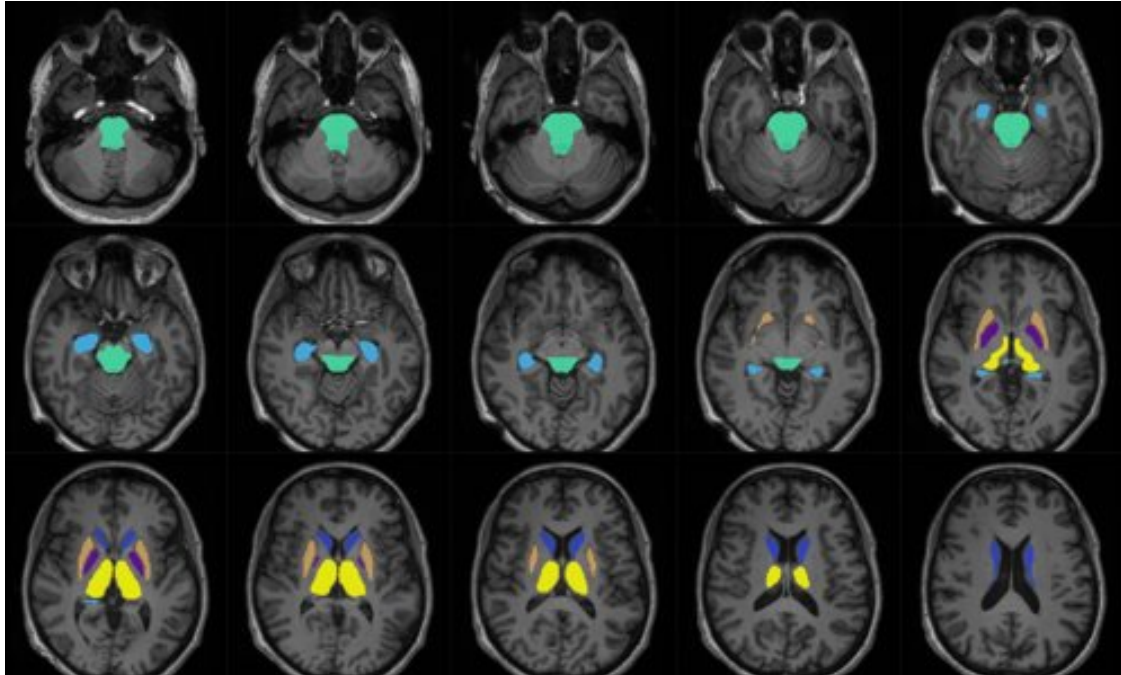


Fig 4.11 FSL FIRST segmentation (<https://fsl.fmrib.ox.ac.uk/fsl/fslwiki/FIRST>) on axial 3D T1 MPAGE. Healthy subject control, femal of 46 years old. Deep gray nuclei and structures (yellow R-L thalamus, blue R-L caudate, orange R-L putamen, purple R-L pallidum, light green brainstem, light blue R-L hippocampus). Same segmented structures are seen on axial QSM images (Fig 4.12 IRCCS Istituto delle Scienze Neurologiche di Bologna).

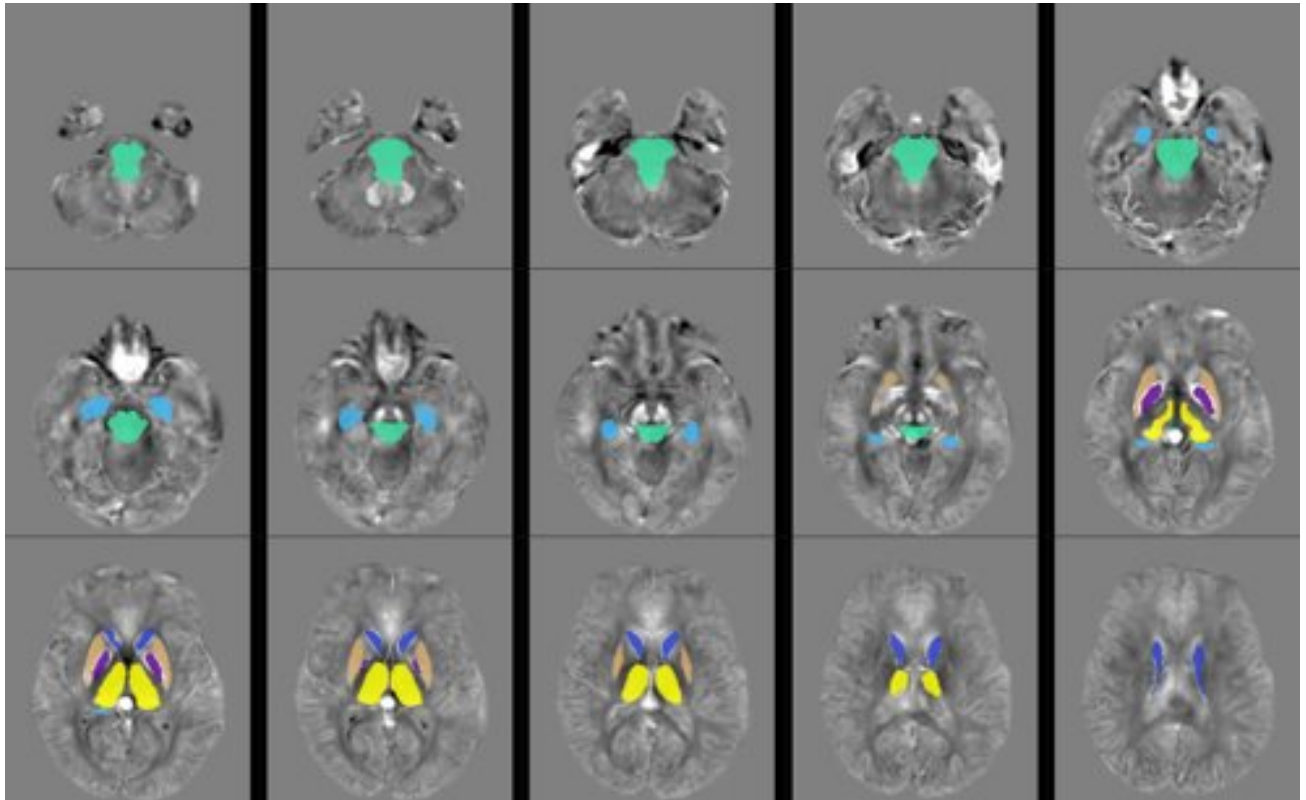


Fig 4.12 FSL FIRST segmentation (<https://fsl.fmrib.ox.ac.uk/fsl/fslwiki/FIRST>) on axial QSM images. Healthy subject control, female of 46 years old. Deep gray nuclei and structures (yellow R-L thalamus, blue R-L caudate, orange R-L putamen, purple R-L pallidum, light green brainstem, light blue R-L hippocampus). Same segmented structures are seen on axial 3D T1 images (Fig 4.11). *IRCCS Istituto delle Scienze Neurologiche di Bologna*

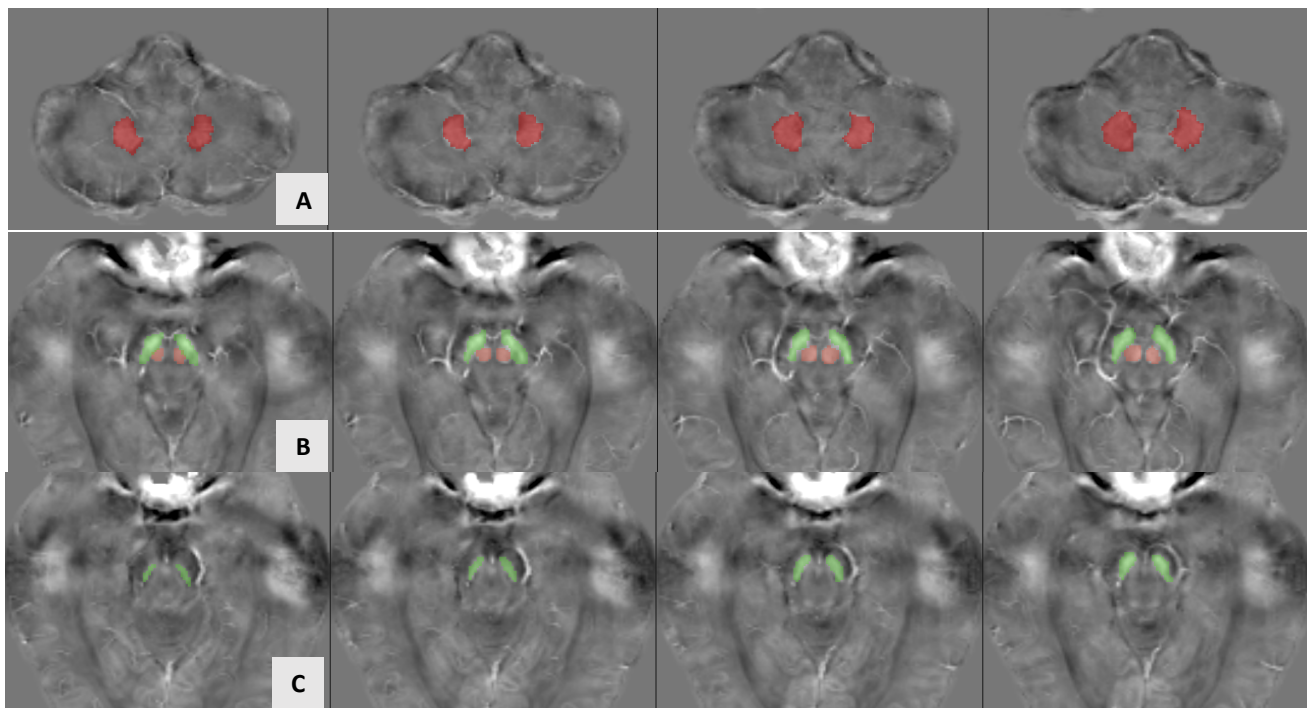


Fig. 4.13 Semi-automatic segmentation on axial QSM images of DN, RN e SN. HC subject, male 54 years old. Dentate nuclei (A: upper row, dark red), red nuclei (B: middle row, light red) and substantia nigra (B and C: middle and lower row, green). QSM maps linearly registered on MNI atlas. (elaboration pipeline in described in paragraph 3.5.2). *IRCCS Istituto delle Scienze Neurologiche di Bologna*

4.6 Statistical analysis

The statistical analysis approach is detailed following the order of the paragraphs of the Section 5 (Results).

Due to the larger PD population with respect to the other groups, for the comparison measurements between three groups we selected a reduced sample of 22 patients; otherwise the entire PD 41-subject sample was considered.

Study population: we did an exploratory investigation, in order to verify if the analyzed groups were as homogeneous as possible. Age, brain volume, UPDRS III and MMSE distributions of PD, RBD and MSA populations were compared each other using non-parametric Kruskal-Wallis test and considering significant difference with *p-value* <0.05. This test was selected since the distributions resulted non-normal from one-sample Kolmogorov-Smirnov test.

Qualitative brain imaging results: total nigrosome score, putaminal intensity and putaminal score distributions were compared between PD, RBD and MSA patients, using non-parametric Kruskal-Wallis test and considering significant difference with *p-value* <0.05. This test was selected since they resulted non-normal from one-sample Kolmogorov-Smirnov test. Note that for what concerns the putaminal signal comparison, three PD, two RBD and one MSA patients have to be excluded since the SWI sequence was not acquired during the MRI exam.

Quantitative brain imaging results: susceptibility median, 90th percentile and volume in 8 structures (Caudate, Hippocampus, GP, Putamen, Thalamus, Substantia Nigra, Red nuclei and Dentate nuclei) were analyzed, in particular: a) comparison of susceptibility and volume structures between the three group of patients was carried out. Since none of the distributions resulted normal, Kruskal-

Wallis test was used, with Bonferroni correction and considering p -values < 0.006 significant. (**)

Age was inserted as covariate index during the analysis, to check its influence on the results; b) correlation between median susceptibility and volume was evaluated in each structure and in each group separately, measuring Spearman's coefficient and considering significant p -values < 0.006 .

MRI and Clinical Correlation analysis: Correlation between nigrosome score and disease severity (UPDRS-III, H&Y, and disease duration) in PD, RBD and MSA groups, and correlation between median susceptibility in each structure and MMSE in PD group were evaluated. Spearman's coefficient was calculated and p -values < 0.05 considered significant.

5 RESULTS

5.1 Study population

We studied a population of 67 patients: 41 PD (19 F, 22 M; mean age: 60.9 ± 7.5 years, range 43-71), 12 were affected by MSA-P (6 M, 6 F, mean age 66.9 ± 8.8 years, range 55-78), 14 had a diagnosis of RBD (14 M; mean age 67.2 ± 8.2 years, range 55-82). QSM images were available in all out of selected sample patients and suitable for qualitative and quantitative analysis. SWI images for qualitative evaluation was not acquired in two PD, two RBD and one MSA patients; not evaluable for movement artifacts in one PD patient. Demographic data of the three different groups are presented in **Tab 5.2**.

PD patients were classified according to the clinical phenotype: 25 bradykinetic (BR), 11 tremorigen (T) and 5 had a mixed phenotype. Disease duration was between one and 20 years (mean 10.0 ± 4.4): in 17 % of cases ≤ 5 years, in 83 % >5 years; UPDRS III mean score was 42.7 ± 14.4 ; H&Y median score was 2.14 ± 0.57 (range 1–3). MMSE mean score was 27.83 ± 2.05 .

In MSA-P patients disease duration was between <1 and 21 years (mean 6.5 ± 6.4): in 64% cases ≤ 5 years; in 36% of cases >5 years. UPDRS III mean score was 42.2 ± 18.7 ; H&Y median score was 3.13 ± 0.96 (range 2–5). MMSE mean score was 29.01 ± 0.89 .

In the RBD group disease duration was between two and 17 years (mean 7.4 ± 4.7): in 57 % of cases ≤ 5 years, in 43 % >5 years. UPDRS III mean score was 5.6 ± 4.5 . MMSE mean score was 29.01 ± 0.89 .

Comparison of age and brain volume between three groups of patients are showed in **Fig 5.1**.

Comparison of clinical between three groups are showed in **Tab 5.3**.

Disease severity (UPDRS III sub-scores) was significantly greater in MSA vs RBD and in PD vs RBD group: in both comparison the p-value from Kruskal-Wallis test results $< .000^*$, highlighting a significant difference. No significant differences were observed between MSA and PD groups (**Tab 5.3**).

Table 5.2: Demographic data of the three different groups. PD (n= 41): entire sample; PD (n= 22): sample for comparison between groups.

	PD (n= 41)	PD (n= 22)	RBD (n=14)	MSA (n= 12)
Mean Age\pm SD/ (y)	60.9 \pm 7.5	66.0 \pm 3.0	67.2 \pm 8.2	66.9 \pm 8.8
Min	43	60	55	55
Max	71	71	82	78
M	22	12	14	7
F	19	10	0	5

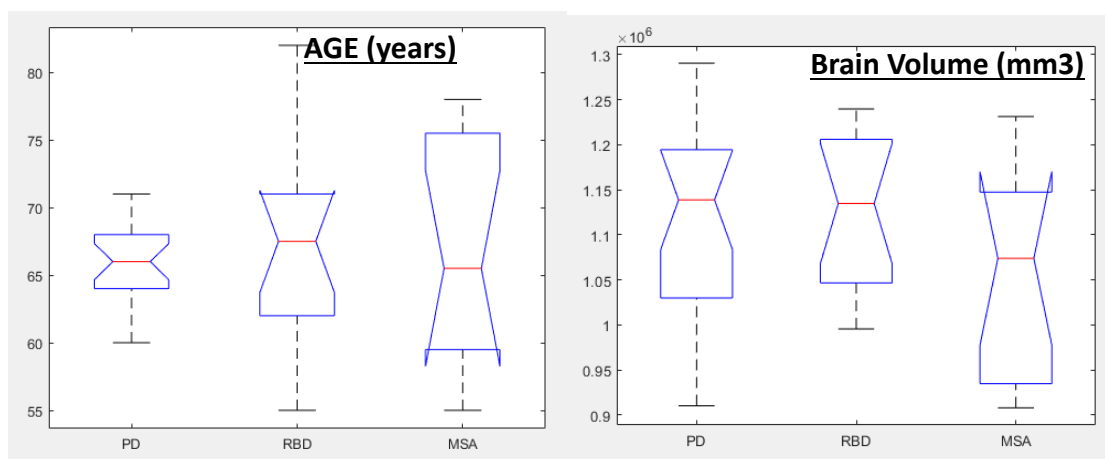


Fig 5.1: Box plot of age and brain volume distribution. Vertical dashed lines (whiskers) show lower and upper values. Box stretches from lower hinge (25th percentile) to upper hinge (75th percentile). Median age (left side) and brain volume (right side) shown as line across each box. Comparison between three clinical subgroups with Kruskal Wallis test: the three groups are comparable for age and brain volume (p-value= 0.060).

Table 5.3: Comparison of main clinical data between the three-groups of patients.

	PD (n= 22)	RBD (n= 14)	MSA (n=12)	<i>p</i>
Age (y)	66.0 ± 3.0	67.2 ± 8.2	66.9 ± 8.8	<i>ns</i>
Disease duration (y)	11.0 ± 4.4	7.4 ± 4.7	6.5 ± 6.4	<i>ns</i>
UPDRS III (OFF)	44.1 ± 13.8	5.6 ± 4.5	42.2 ± 18.7	<0.000
H & Y	2.20 ± 0.41	/	3.13 ± 0.96	/
MMSE	27.7 ± 2.0	28.79 ± 0.84	29.09 ± 0.89	<i>ns</i>

Considering *p* values <0.05 significant (*) UPDRS III was significantly higher in PD group vs RBD (*p* <0.000) and in MSA group vs RBD (*p* <0.000).

5.2 Conventional imaging evaluation results

In the three groups age, , disease duration, MMSE score were not statistically different (Table 5.3).

The presence of conventional MR signs on MPRAGE T1 images was evaluated on whole sample of 67 patients (41 PD, 14 RBD, and 12 MSA) and was recorded as follows: hot cross bun sign in 16.7 % of MSA; MCP hyperintensity in 16.7 % of MSA; postero-lateral putaminal hypointensity (evaluated on SWI images) in 100% of MSA; putaminal hyperintense rim (evaluated on FLAIR image) in 58.3% of MSA patients.

None of PD or RBD patients presented the hot cross bun sign, MCP hyperintensity, postero-lateral putaminal hypointensity on SWI images and putaminal hyperintense rim on FLAIR images.

Morphometric evaluations were recorded according to [Quattrone A et al. 2008](#) in all three groups of patients and compared to a sample of age matched healthy subjects: pons area (lower normal values > 386 mm²), mesencephalic area normal values > 94 mm²), medial cerebellar peduncle (MCP) (lower normal values > 8.10 mm) and superior cerebellar peduncle (SCP) length (width) (lower normal values

> 3.1 mm) We found: pons reduced area in 16.7 % of MSA, and in none of of PD and RBD patients; midbrain reduced area in 8.3% of MSA patients, and in none of PD and RBD patients; MCP reduced width in 16.7% of MSA patients, and in none of PD and RBD patients; SCP reduced width decrease in 5% of PD patients, and in none of RBD and MSA patients.

Table 5.4: in Distribution of targeted structures atrophy in the three-groups of patients.

	Pons reduced area (%)	Midbrain reduced area (%)	MCP reduced width (%)	SCP reduced width (%)
PD	0	0	0	5.0
RBD	0	0	0	0
MSA	16.7	8.3	16.7	0

MCP= medial cerebellar peduncle, SCP= superior cerebellar peduncle.

5.3 Imaging features of nigrosome score between three groups

A total of 48 participants with an acceptable quality of QSM images were included in this evaluation. The sample included 22 PD, 12 MSA and 14 RBD patients. Nigrosome score of quantification and distribution in three groups are shown in **Tables 5.4, 5.5 and 5.6 and Figure 5.4**). For all STS, on total score nigrosome, an inter-rater agreement of 70% was reported.

Bilateral total loss of STS (total score: 0) was shown in 6/12 (50%) patients with MSA, 10/22 (45,5%) patients with PD and in only 1/14 (15%) patient with RBD. Bilateral nigrosomial STS blurring or monolateral total loss of STS (total score: 2) was shown in 7/22 (31.8%) patient with PD, in 1/14 (7.1 %) patients with RBD, and in 4/12 (33%) patients with MSA. Bilateral presence of STS was not detected

in in any PD and MSA patient, in 3/14 patients with RBD (21.5%). Nigrosome score on each side in three different groups are shown in **Tables 5.4-5.6**.

Frequency distribution of nigrosome score was significantly different between PD and RBD ($p=0.0013^*$) and between MSA and RBD ($p=0.0084^*$); in both group's comparison the nigrosome score was higher in the RBD group, which means that STS (nigrosome structure) was better detected in this group. No statistical difference was observed between PD and MSA groups, as expected and reported in previous studies ([Kwon et al 2012](#))(Table 5.7 and Figure 5.2).

Tab. 5.4 Nigrosome score in PD group.

PD (n. 22) NIGROSOME SCORE	Right	Left	TOTAL SCORE	
			n. patients	%
Grade 0	14	13	10	45.5
Grade 1	7	9	7	31.8
Grade 2	1	0	4	18.2
Grade 3	--	--	1	4.5
Grade 4	--	--	0	0

Tab. 5.5 Nigrosome score in RBD group

RBD (n: 14) NIGROSOME SCORE	Right	Left	TOTAL SCORE	
			n. patients	%
Grade 0	1	2	1	7.1
Grade 1	10	8	1	7.1
Grade 2	3	4	8	57.2
Grade 3	--	--	1	7.1
Grade 4	--	--	3	21.5

Tab. 5.6 Nigrosome score in MSA group

MSA (n 12) NIGROSOME SCORE	Right	Left	TOTAL SCORE	
			n. patients	%
Grade 0	1	7	6	50.0
Grade 1	10	5	2	16.7
Grade 2	3	0	4	33.3
Grade 3	--	--	0	0.0
Grade 4	--	--	0	0.0

Tab 5.7 The frequency of distribution of **nigrosome total score** in the three different clinical group.

NIGROSOME SCORE	n. pz	GRADE 0 (n.)	GRADE I (n.)	GRADE II (n.)	GRADE III (n.)	GRADE IV (n.)	<i>p</i>
PD	22	45.5% (10)	31.8% (11)	18.2.% (6)	4..5% (3)	0% (2)	0.0013*
RBD	14	7.1% (1)	7.1%(1)	57.2% (8)	7.1% (1)	21.5%(3)	
MSA	12	50.0%(6)	16.7%(2)	33.3%(4)	0.0	0.0	0.0084*

P values in table refer to comparison with RBD group. Considering *p* values <0.05 significant (*) nigrosome score was significantly higher in PD group vs RBD ($p=0.0013^*$) and in MSA vs RBD ($p= 0.0084^*$), but showed no significant differences between PD and MSA groups.

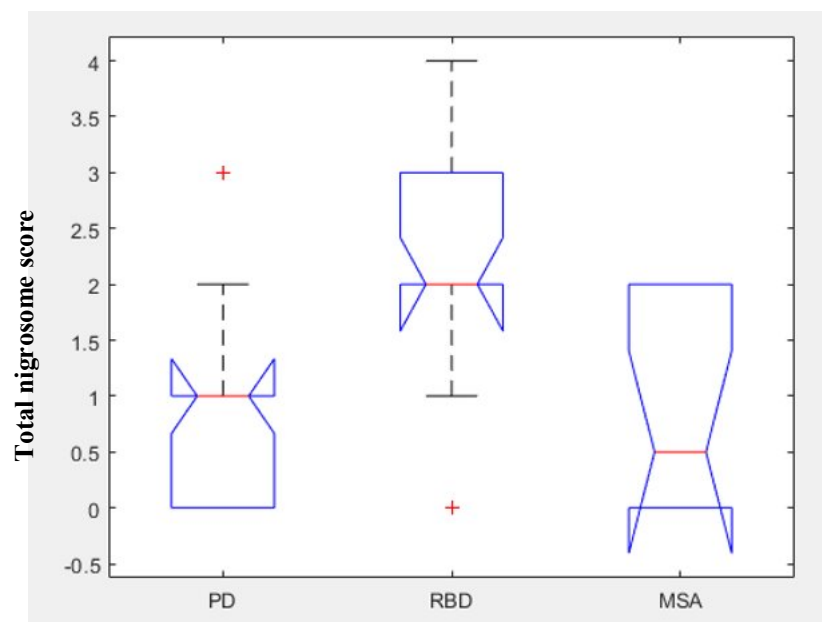


Fig 5.2 Box plot of total nigrosome score in three different clinical group. Vertical dashed lines (whiskers) show lower and upper values. Box stretches from lower hinge (25th percentile) to upper hinge (75th percentile). Median nigrosome score shown as line across each box. Left: PD group. Middle: RBD group. Right: MSA group. Considering *p* values <0.05 significant (*) nigrosome score was significantly lower in PD group vs RBD ($p=0.0013^*$) and in MSA vs RBD ($p= 0.00159^*$), but showed no significant differences between PD and MSA groups.

5.4 SWI putaminal analysis

Among the 47 patient sample in SWI sequences were not acquired in three PD, two RBD and one MSA patient . Therefore SWI putaminal analysis was performed in 41 patients: 19 PD, 11 RBD and 11 MSA). Putamen ROIs SI in the three groups is shown in Table 5.8 and Figure 5.3; subdivision of groups in different grades (putamen score) are reported and illustrated in Tab 5.9. and fig 5.7. Kruskal-Wallis test was used to perform the comparison. Considering p values <0.05 significant (*) putaminal SI was significantly lower in MSA patients when compared to PD ($p=0.00002^*$) and in RBD group ($p= 0.00159^*$), but showed no significant differences between PD and RBD patient groups (Tab 5.9 and fig 5.6). For bilateral putaminal analysis, an inter-rater agreement of 71% was reported.

Tab 5.8 Signal Intensity evaluation of Putaminal nuclei ROIs in different clinical groups.

	Putamen SI (mean \pm DS)	<i>p</i>
PD (n= 19)	241.5 \pm 59.8 (159-351)	0.00002*
RBD (n=12)	206 \pm 58.8 (110-285)	0.00159*
MSA (n=11)	88.6 \pm 59.8 (26-178)	

P values in table refer to comparison with MSA group. Considering p values <0.05 significant (*) putamen SI was significantly higher in MSA patients when compared to PD ($p=0.00002^*$) and RBD ($p= 0.00159^*$), but showed no significant differences between PD and RBD patient groups.

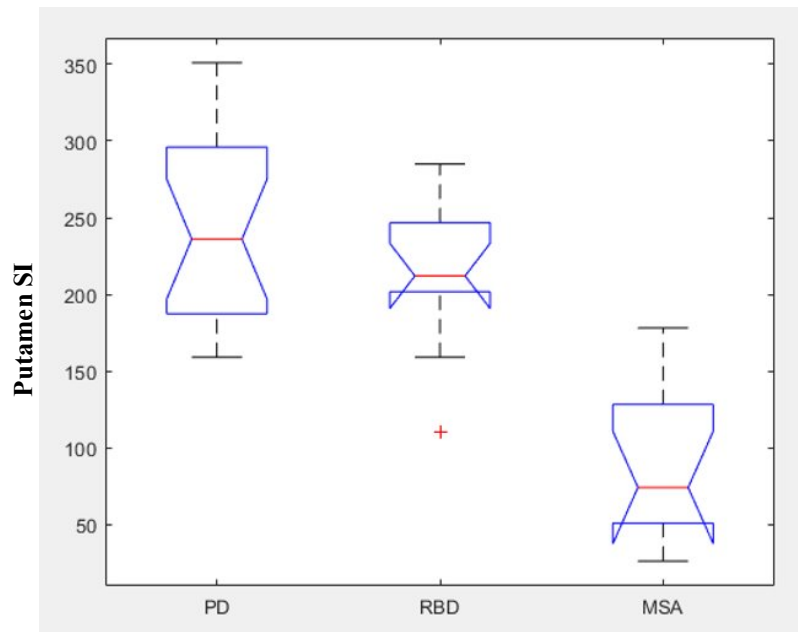


Fig. 5.3

Box plot of frequency distribution of putamen SI in three different clinical groups. Vertical solid lines (whiskers) show lower and upper values. Box stretches from lower hinge (25th percentile) to upper hinge (75th percentile). Median putamen SI shown as line across each box. Considering p values <0.05 significant (*) nigrosome score was significantly lower in MSA vs PD ($p=00002^*$) and in MSA vs RBD ($p=0.00159^*$), but showed no significant differences between PD and RBD groups.

Considering putamen score, patients with PD had lower hypointensity scores (0 or 1) n , and none had a score of 2 or 3. On the other hand, patients with MSA frequently scored 2 or 3 and none had score of 0. RBD group showed a prevalent score of 2 (**Tab 5.9**). Since the hypointensities of the regions of interest can be physiologically affected by aging, noteworthy we considered three groups matched by age. Putamen score histogram in all three groups is reported in **Fig 5.7**.

Tab 5.9 Putamen score in all three clinical groups.

PUTAMEN SCORE	n.patients	GRADE 0	GRADE I	GRADE II	GRADE III	<i>p</i>
PD	19	63.2% (12)	36.8% (7)	0.0	0.0	0.00004*
RBD	12	75.0%(9)	8.3% (1)	16.7% (2)	0.0	0.00004*
MSA	11	0.0	18.2% (2)	18.2% (2)	63.6% (7)	--

Considering *p* values <0.05 significant (*) putamen score was significantly higher in MSA patients when compared to PD (*p*=0.00004*) and to RBD (*p*= 0.00004*), but showed no significant differences between PD and RBD patient groups. *P* values in table refers to comparison with MSA group. For each grade is indicated percentage over total number of patients and in brackets exact n.of patients (in brackets) .

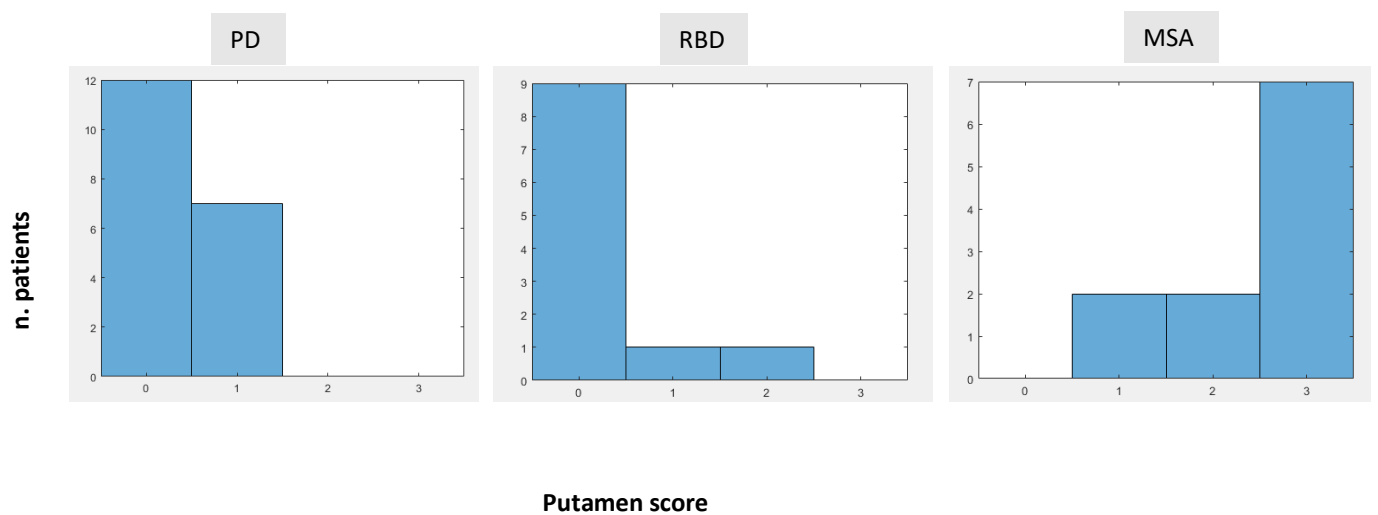


Fig 5.4 Putamen score histogram in all three groups.

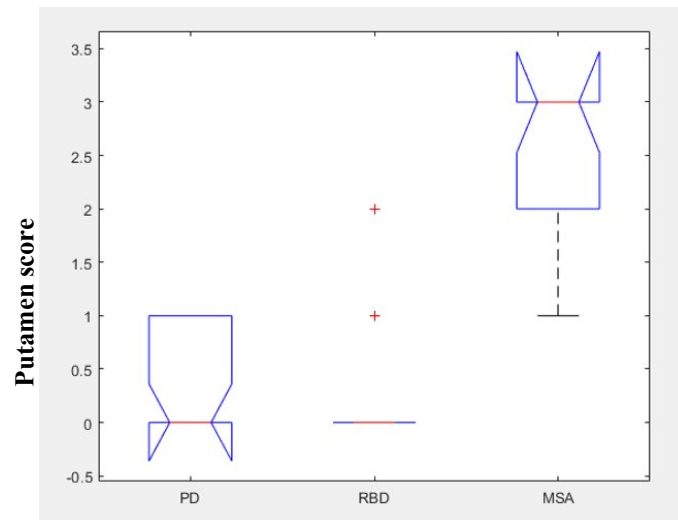


Fig 5.8 Box plot of frequency distribution of putamen score in three different clinical groups. Vertical solid lines (whiskers) show lower and upper values. Box stretches from lower hinge (25th percentile) to upper hinge (75th percentile). Median putamen score shown as line across each box. Considering p values <0.05 significant (*) putamen score was significantly higher in MSA vs PD ($p=0.00004^*$) and in MSA vs RBD ($p=0.00004^*$), but showed no significant differences between PD and RBD groups.

5.4 Quantitative brain imaging results

Susceptibility and volume: description In fig 5.7 are reported values of χ (median and 90° percentile) and volume comparison for all ROIs considered in three different groups. Significant differences across patients were observed in putamen (MSA vs PD) with effect of age being statistically controlled.

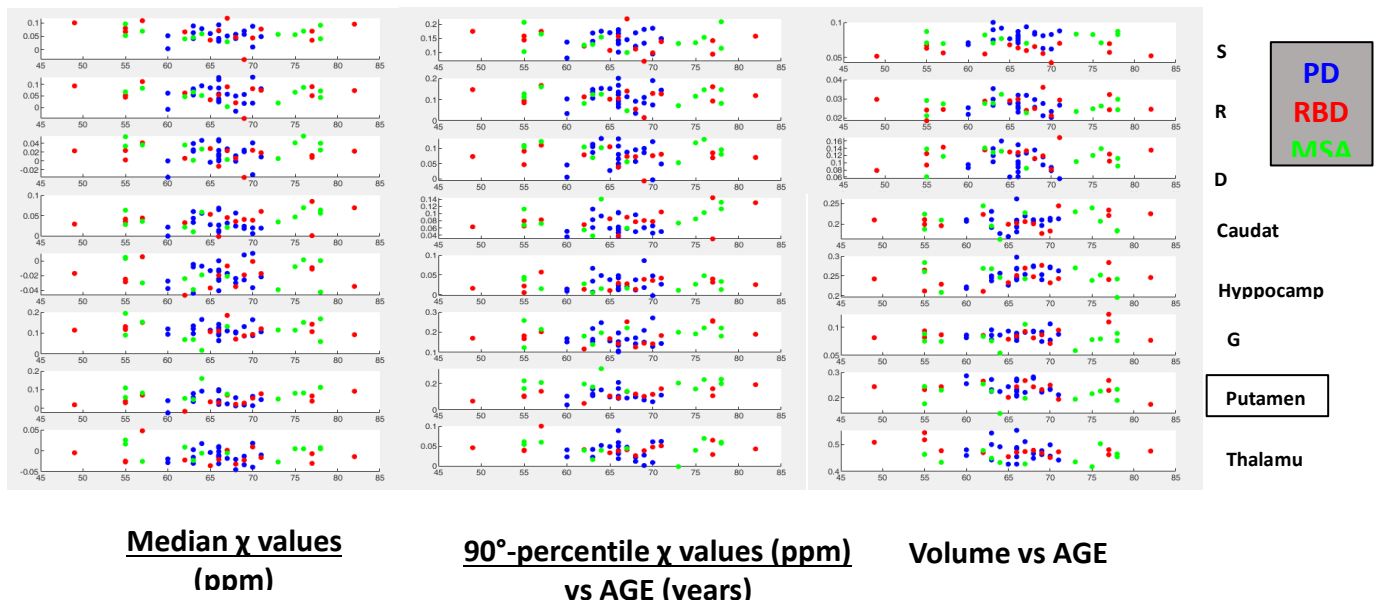


Fig 5.7 Values of χ (median and 90°-percentile) and volume comparison for all ROIs considered in three different clinical group. Significant differences across patient groups were observed in putamen (MSA vs PD), with the effect of age being statistically controlled (non-significant). Test Test Kruskal-Wallis Bonferroni correction ($P * < 0.006$)

In Fig 5.8 and 5.9 bar plots of median and 90th percentile susceptibility in the analyzed structures are reported. The highest χ values were observed in globus pallidus. At SN the median susceptibility values were higher in RBD than in PD and MSA, and in MSA with respect to PD. The highest putaminal χ was recorded in the MSA population to respect PD patients and RBD patients. Axial QSM images passing through the foramen of Monro showing the caudate, putamen,

globus pallidus comparing patients with PD, RBD and MSA are shown in Fig 5.10.

Susceptibility: comparison between PD, RBD, MSA

Values of χ (median) for all ROIs considered in this study are reported in Fig 5.8: significant differences across patient groups were observed in putamen of MSA patients vs PD group, as expected from previous work, with Kruskal-Wallis and Bonferroni correction ($P^* = 0.002$). Age was inserted as covariate index during the analysis and did not show significant difference between the three group, which means that the slope of iron growth with age does not change referring to PD, RBD or MSA.

Values of χ (90^o percentile) for all ROIs considered in this study are reported in Fig 5.9: there are significant differences in putamen 90th percentile susceptibility between MSA and PD groups ($P^* < 0.000$) and between MSA and RBD groups ($P^* = 0.001$). Note that, as already mentioned, 90th percentile refers to the high-concentration iron regions in non gaussian distribution. Results showed that both median values and 90th percentile susceptibility values of putamen are significantly involved in PD-MSA discrimination, while only the second one is involved in MSA-RBD discrimination. That means that in this situation the difference mainly lies in putamen subregions in which iron is more concentrated.

Putaminal median X and 90th percentile were predictors with high diagnostic accuracy for the MSA group with respect to PD (AUC: 0.807 and 0.932) and RBD (AUC: 0.804 and 0.905) (Tab 5.10).

Tab 5.10 Diagnostic accuracy (AUC) of median and 90° percentile susceptibility (χ) in the comparison of MSA-PD and MSA-RBD groups. AUC: area under the curve.

	Median χ (ppm)	90° percentile χ (ppm)
PD – MSA	0.807	0.932
RBD - MSA	0.804	0.905

Susceptibility and volume: correlation

We correlated values of χ (median) and volume for all ROIs selected between three groups and we found significant positive correlation in DN of PD patients (increase of values of χ (median) with increase of volume in DN. In our cohort of PD patients we didn't find any significant differences between AR (akinetic rigid) group, the T (tremorigen) in median values of χ in DN.

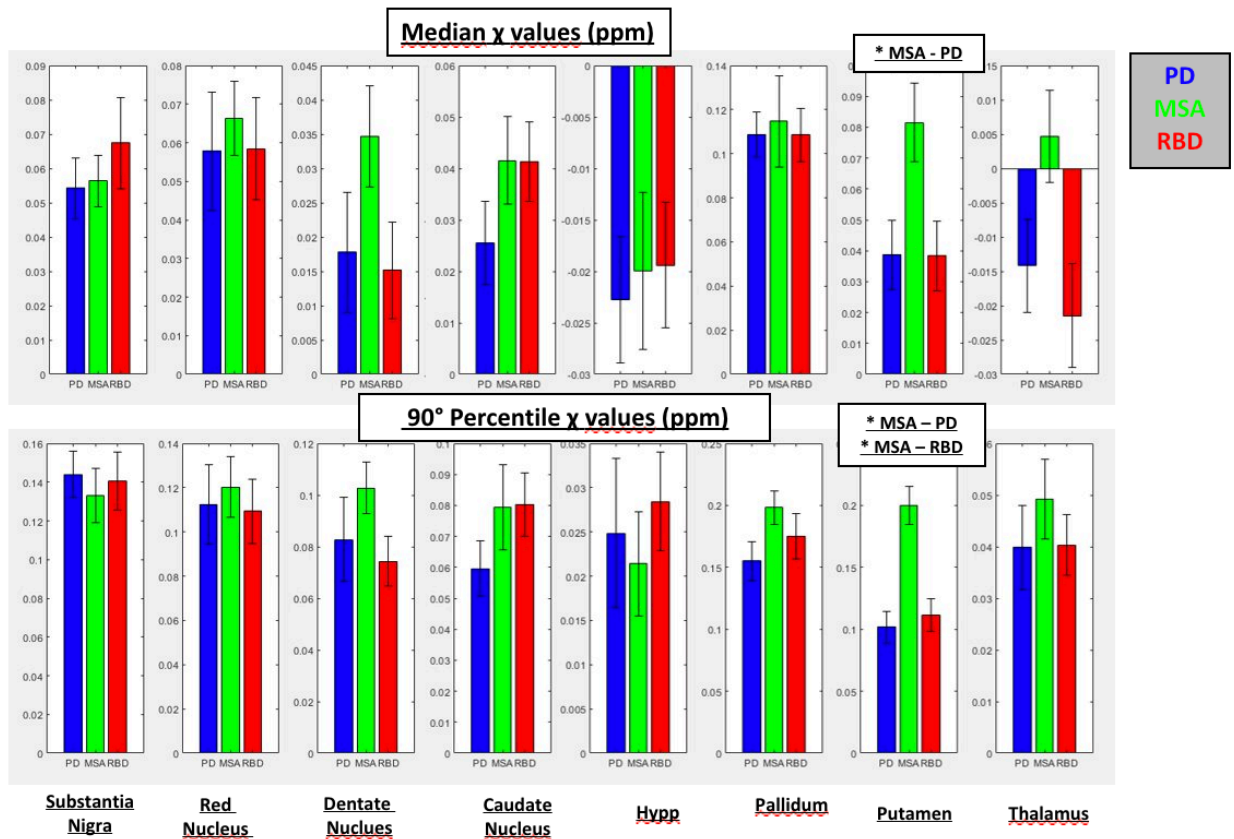


Fig 5.8 Comparison of median susceptibility values 90°-percentile χ values (ppm) (χ ppm) of substantia nigra and extranigral segmented structures in three clinical groups

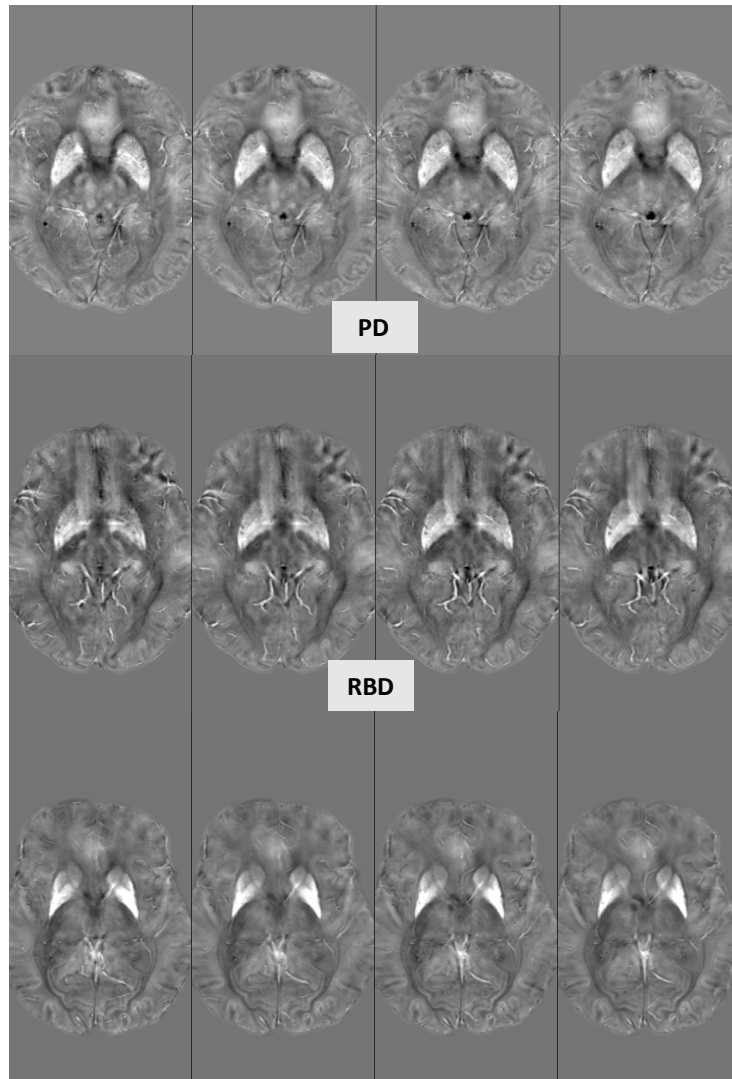


Fig 5.10 Axial QSM images passing through the foramen of Monro showing the caudate, putamen, globus pallidus comparing patients with PD (upper row M/71y), RBD (middle row M/71y) an MSA (lower row F/73y). Putamen window of susceptibility values: $-0.03 +0.17$ parts per million (ppm)

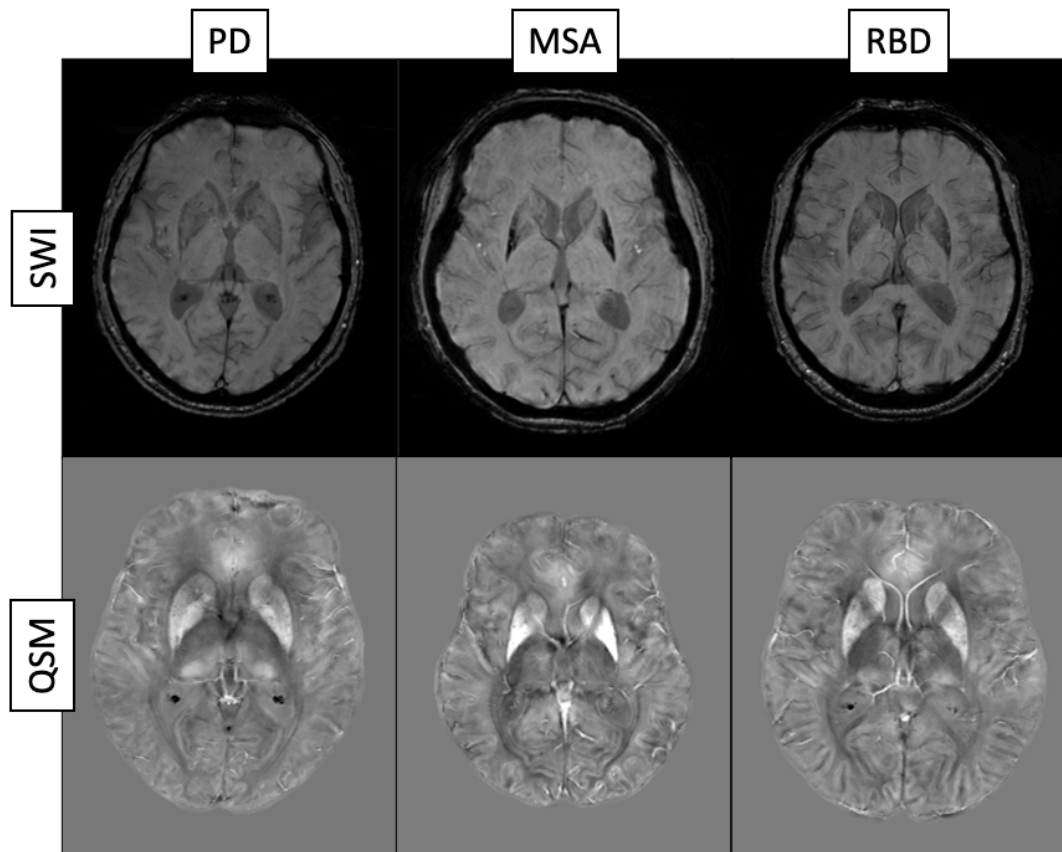


Fig 5.11 Comparison of axial SWI (first row, 3D GRE T_2^*w , TR/TE=28/20ms, $0.5 \times 0.5 \times 1.5 \text{mm}^3$) and QSM (second row, 3D GRE T_2^*w , nTEs=5, TE1/ Δ TE/TR=9.42/9.42/53ms, $0.5 \times 0.5 \times 1.5 \text{mm}^3$): PD (M/71y), MSA (F/73y) e RBD (M/71y). *IRCSS Istituto delle Scienze Neurologiche Bologna*

5. 5 MRI and Clinical correlations analysis

The correlations between STS scale (nigrosome score) and disease severity in PD, RBD, and MSA were explored. The nigrosome score in patients with PD was not significantly correlated with UPDRS III (Spearman -0.177 *p*-value 0.827,), with H–Y stage (Spearman -0.038 *p*-value), duration of disease (Spearman 0.055, *p*-value 0.745); no significant correlation between STS scale and disease severity in the RBD and MSA groups were found as well.

Table 5 The Spearman correlation of nigrosome score with disease severity (UPDRS III, H&Y, disease duration disease) in PD, RBD and MSA patients.

	UPDRS III OFF		H & Y		DURATION OF DISEASE	
	Spearman	<i>p</i>	Spearman	<i>p</i>	Spearman	<i>p</i>
PD	-0.177	0.827	-0.038	0.821	0.055	0.745
RBD	-0.265	0.359	<i>ns</i>	<i>nc</i>	-0.165	0.572
MSA	0.198	0.583	0.332	0.349	-0.346	0.298

UPDRS III, Unified Parkinson’s Disease Rating Scale Part III, OFF (without medication); H–Y, Hoehn and Yahr; STS, swallow tail sign

We finally evaluated in PD subgroup (with or without RDB status) values of χ (median and 90° percentile) and volume in all ROI selected, that didn’t show significant differences between two subclinical PD subgroup (with or without RBD status)

None statistical correlation was found between values of χ (median) and MMSE in all ROIs selected, including Hippocampal region in PD (fig 5.12).

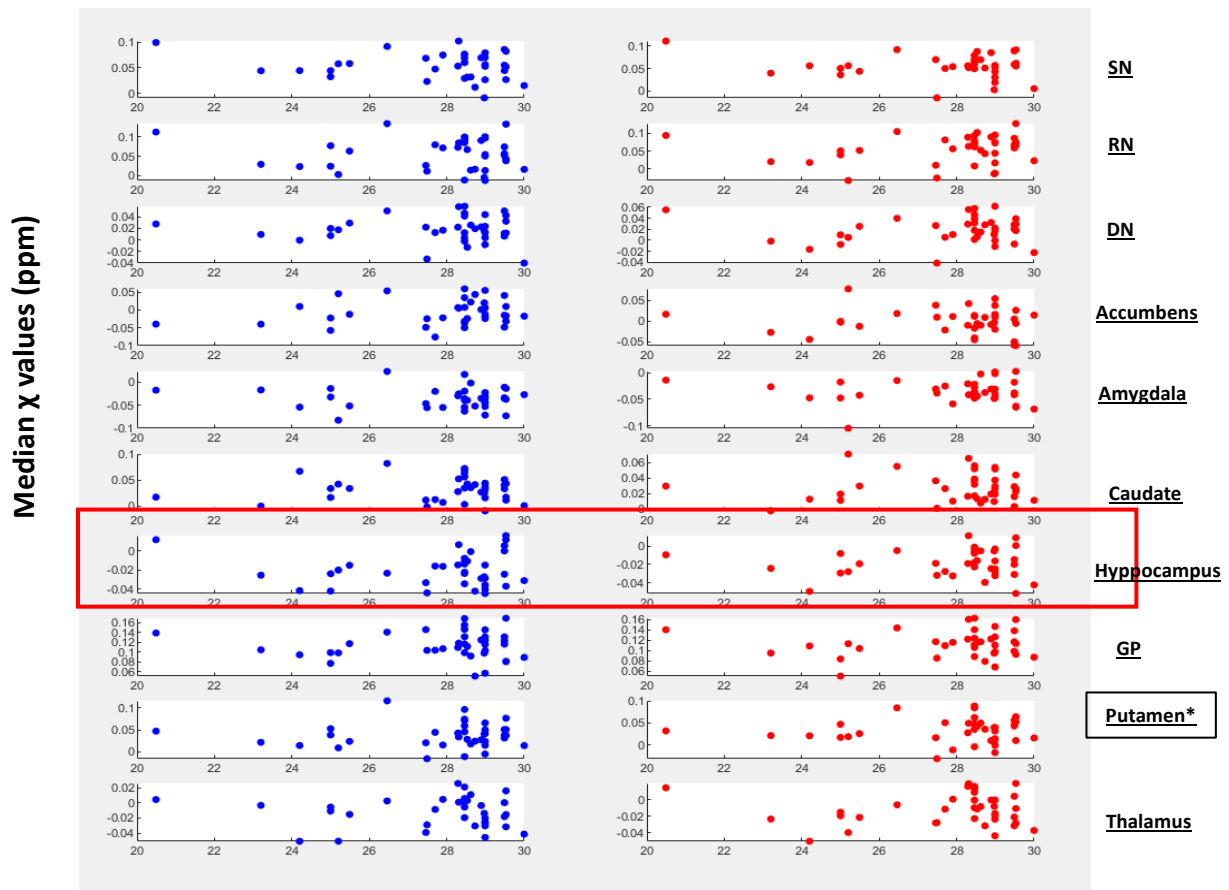


Fig 5.12 a: Median χ values (ppm) vs MMSE in all ROI selected. No significant correlation including Hippocampus (red box see fig 5.12 b in detail).

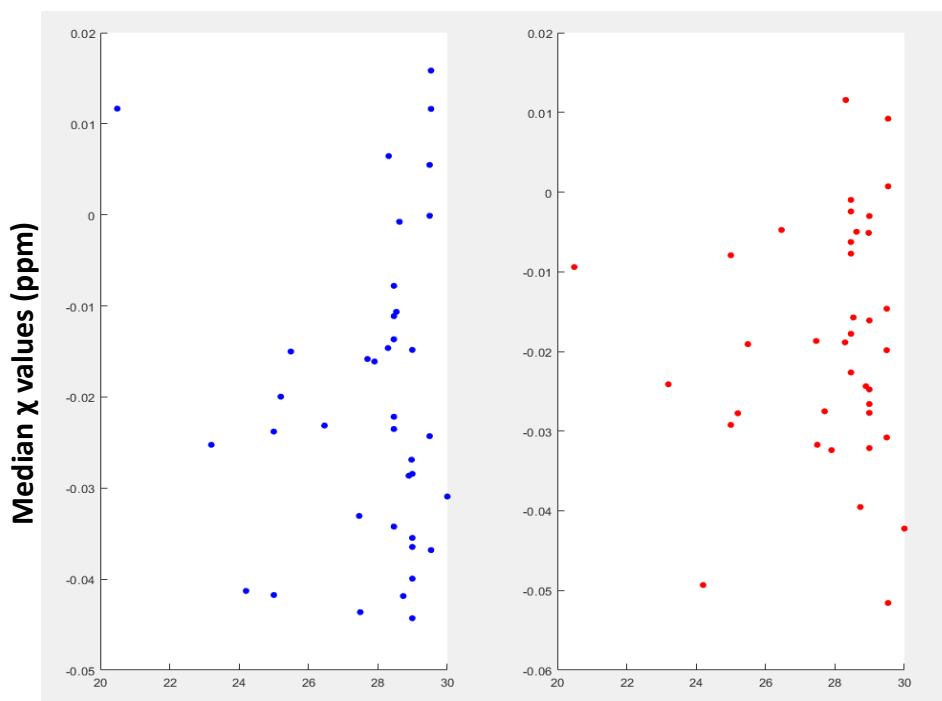


Fig 5.12 b: Median χ values (ppm) in Hippocampus vs MMSE

6. DISCUSSION

In idiopathic Parkinson's disease and atypical parkinsonian disorders, the differential diagnosis can be challenging, as demonstrated by a significant number of patients with an incorrect clinical diagnosis in two histopathological studies (Koga et al 2015, Miki et al 2019). An early and accurate diagnosis helps to choose the optimal therapeutic decisions and provides opportunities to participate in clinical research trial.

Conventional MRI signs described in parkinsonisms showed high specificity but low sensitivity, giving a limited support to clinical diagnostic criteria (Massey et al., 2012; Meijer et al., 2015).

One of the most utilized method for targeted-structures atrophy evaluation on conventional imaging is the “Parkinsonian index” (Quattrone et al., 2008), but the low sensitivity of these macroscopic findings at autopsy may limit the accuracy of the diagnosis in the early phase of disease underlying the need for imaging techniques sensitive to microstructural abnormalities which precede the regional atrophy (Massey et al., 2012).

Recent studies using SWI or QSM (Reiter E et al 2015; Calloni SF, et al 2018, Jin L et al 2019, Stezin A et al 2018) techniques focused on the nigrosome-1 detection and reported a sensitivity ranging from 79.4% to 98.5% and a specificity of 85%–97.2%, in discriminating PD vs controls. (Liu X et al 2021). Nevertheless more recent studies evaluating the Substantia Nigra anatomy with SWI failed to demonstrate differences between PD and atypical parkinsonian syndromes (Reiter et al., 2015; Meijer et al. 2015; Frosini et al., 2016).

In our cohorts of PD and MSA P patients the qualitative evaluation of the SN on QSM images showed the loss of the typical nigral structure in most cases: we found significant differences in PD vs RBD and in MSA vs RBD, while the nigrosome score was similar in PD and MSA groups . Therefore, according to

some previous studies ([Koga et al. 2015](#)), our data confirming that qualitative nigrosomal analysis approach does not help the differential diagnosis among parkinsonism.

With respect to the discrimination of two nigrosomal subregions (N1 e N4) we were able to obtain a high accuracy and a good agreement by evaluating axial e coronal oblique QSM images, unlike [Sung et al \(2018\)](#). These authors claimed to differentiate two nigrosomal subunits according to the stage of PD: they found more frequent abnormality in nigrosome 1 in early-stage PD, more frequent abnormality in the putative nigrosome 4 in late-stage PD and no solitary involvement of the putative nigrosome 4 in any SNc.

The failure to distinguish the two different subunits could have some possible explanations: it may mainly depend on our population, which lacked PD in early stage (mean disease duration: 11.0 ± 4.4 years), but also on high anatomical variability of nigrosome structure as documented by histopathological study ([Damier P, Hirsch, et al 1999](#)). Finally, intensity of magnetic field may play a role, affects the ; as demonstrated by the a discrimination of all five nigrosomes thanks to an ultra-high field magnet (9.4 T) using spin-echo high resolution magnetic resonance images ([Massey LA et al. 2017](#)).

Moreover we investigated the accuracy in the differential diagnosis among APS of putamen abnormalities. The presence of postero-lateral putaminal hypointensity improved the diagnostic accuracy of brain MR imaging. Our data, according to literature ([Meijer FJA et al 2015](#)), confirms that the mean SWI signal intensity of the putamen evaluated on SWI images was significantly lower in MSA-P patients compared to Parkinson disease and RBD groups. On the other hand, no significant differences between PD and RBD groups were found (Tab 5.9 and fig 5.6). Moreover, median putamen score was significantly higher in MSA vs PD and in MSA vs RBD, but showed no significant differences between PD and RBD groups (Fig 5.)

Wang et al (Wang Y., Butros SC et al 2012) found increased iron deposition in the putamen in MSA-P, as we did, and reported that the lower inner region of the putamen was the most valuable subregion in differentiating MSA-P from PD, while in our study, according to Meijer et al 2015 this finding was demonstrated for the posterior part of the putamen.

Gupta et al (Gupta et al 2010) found higher putaminal SWI hypointensity scores in MSA-P respect PD, although this difference was not statistically significant.

It is important to underline that SWI signal intensity is influenced by many factors besides iron content of brain structures, including acquisition parameters and magnetic field strength but also by spatial position and reconstruction algorithms which differ across MR imaging vendors. For reproducibility of quantitative analyses, it is crucial to apply a normalization technique. Our study population was scanned by using a 3T MR imaging scanner, while in others studies a 1.5T scanner was used (Gupta et al 2010, Wang Y., Butros SC et al 2012). Different magnetic field strengths likely explain some discrepancies in different study results because a 3T MR imaging scanner is more sensitive to susceptibility changes than a 1.5T scanner (Nandigam RN et al 2019 , Wardlaw JM, et al 2012)

Since no significant differences were found between PD and MSA groups in nigrosome score, we investigated a quantitative approach as for improving the accuracy of differential diagnosis. In our study we included RBD patients, since this disorder, could represent a prodromal phase of Parkinson's disease or other parkinsonisms (Boeve et al 2010). Indeed RBD is present in 25–58% of patients with Parkinson's disease and up to 90% of those with Multiple System Atrophy (MSA) and Dementia with Lewy Bodies (DLB). Indeed, in a relevant proportion of these patients RBD onset occurs before motor symptoms, making RBD a highly specific prodromal marker of synucleinopathies: long- term cohort studies indicate that more than 80% of subjects who presented isolated RBD will progress to an alpha-synuclein related neurodegenerative disorder.

Therefore, we examined the potential of QSM in the differential diagnosis between PD and APS, exploring the role of this quantitative advanced MRI sequence in differentiating three principal clinical group: PD, RBD and MSA.

The selection of ROIs on QSM images was performed on the basis of the neuropathological topography of each disease (Dickson, 2012). Extranigral regions were also selected, including upper structures that receive nigral projections and that are usually spared in PD, but significantly affected by neurodegeneration in APS. Using FSL-FIRST a segmentation/registration tool, T1w ic, hippocampus, globus pallidus, putamen and thalamus. QSM maps were then linearly registered to T1w maps (FSL-FLIRT), in order to analyze susceptibility properties of each segmented structure. We observed increased values of magnetic susceptibility within nigral and extranigral regions in MSA patients compared to PD patients. Interestingly distribution of susceptibility values did not reflect in MSA group the physiological age-related pattern, characterized by maximum iron levels in the globus pallidus, followed by RN, SN and putamen (Hallgren and Sourander, 1958).

While no significant differences of iron content were observed in caudate and globus pallidus, χ of putamen allowed to discriminate not only PD from MSA (median χ values, p Kruskal-Wallis: 0.002; 90°-percentile χ values, p Kruskal-Wallis: 0.000) but also MSA from RBD (90°-percentile χ values, p Kruskal-Wallis: 0.001). The highest values of putaminal iron content were recorded in the MSA group, confirming pathological data of severe involvement of this nucleus during the course of the disease. The increase of susceptibility in the putamen detected is notable since subgroup of patients with MSA-p are more difficult to be clinically distinguished from PD. Our results according literature likely reflect the increased putaminal iron deposition demonstrated in MSA but not in PD subjects (Dexter et al., 1991). The observation of increased susceptibility values in putamen in MSA compared to PD patients is interesting considering that the neurodegeneration in MSA occurs both in dopamine and dopaminoceptive

neurons (G.K. Wenning, C. Colosimo, et al date), and is also in line with histopathological findings of α -synuclein in glial cytoplasmic inclusions within this region in MSA (Ahmed Z et al 2012).

We didn't find significant correlations between UPDRS III scores, H&Y, disease duration, MMSE and nigrosome score in PD patient. These results are in agreement with recent studies (Sjstrom et al 2019). A possible explanation could be related to our cohort characterized by , a high mean disease duration in both MSA and PD patients.

To the best of our knowledge, four studies before have applied the QSM technique to compare patients affected by PD and APS (Sjöström et al., 2017; Ito et al., 2017, Cosottini 2017, Sjöström et al., 2019). Our study is the first that include RBD group to explore the potential use of QSM in a prodromic stage of degenerative parkinsonism. To compare groups of subjects avoiding susceptibility changes unrelated to structural changes we express the values of χ with respect to a reference region (Haacke et al., 2015).

Moreover, we measured values of χ by median and 90°-percentile; the last measure helps to best differentiate non gaussian distributions. Differently from previous studies, from a methodological point of view, we used QSM as a stand alone technique to test the role of magnetic susceptibility for APS differential diagnosi, using a 3T MR system as that is more sensitive to susceptibility phenomena and iron quantification compared to lower field strenght.

FSL-FIRST segmentation of subcortical structures also included hippocampus. Advanced stage Parkinson's disease (PD) patients frequently show other non-motor comorbidities such as cognitive decline/dementia and psychosis. Indeed, while abnormal iron level in the substantia nigra is clinically accepted as a biomarker of PD related to motor dysfunction , due to nigrostriatal degeneration, was non elucidated if this change could impair other brain regions inducing non-

motor symptoms (Braak et al 2003). Accordingly to a previous study, where authors investigated iron level of different subcortical and limbic structures in Parkinson's disease (PD) patients with and without dementia by using QSM images (Darrel D.H et al 2018), we included in FSL-FIRST segmentation in addition to deep brain nuclei also the hippocampus, in order to evaluate median values of χ in PD patients in correlation with MMSE profile: we didn't find any significant correlation between these two variables.

It should to be noted that MMSE is only a screening test of global cognitive dysfunction, resulting not accurate for the assessment of subtle memory decline; or instance in a subject affected by a dysexecutive onset pathology, such as Parkinson's disease, it may not show any deterioration, except at very advanced stages of the disease. It could be desirable to complete cognitive profile of PD patients with others tests, for example the Montreal Cognitive Assessment (MoCA). This represent a screening tool for mild cognitive impairment (MCI) and examines, in the full version, different cognitive domains: executive functions, visuo-constructive skills, language, immediate and deferred memory, attention and concentration, calculation, abstraction, orientation.

Longitudinal QSM studies are needed tor evaluate the role of limbic iron concentration M in PD pathogenesis, its relationship to dementia and its potential role as a biomarker in monitoring treatment by iron chelation therapy.

Some authors (Naving He et al 2017) explored inter-group susceptibility differences in bilateral DN and correlations of clinical features with susceptibility between subclinal forms. They found in contrast to the AR (akinetik rigid) group, the T (tremorigen) group was found to have increased susceptibility in the bilateral DN, when compared to healthy controls. In addition, susceptibility was positively correlated with tremor score in drug naive PD patients.

We correlated values of χ (median) and volume for all ROIs selected between the three groups and we found significant differences in bilateral DN of PD patients. In a previous QSM study, the authors tested the hypothesis that DN iron may be elevated in tremor dominant (TD) PD patients. In our cohort of PD patients we didn't find any significant difference between AR (akinetic rigid) and T (tremorigen) groups in median values of χ in DN.

Our study has some limitations:

The first one is the lack of a group of age matched healthy controls. However, since QSM is a quantitative method and accuracy of QSM in differential diagnosis between HC and PD patients was already demonstrated in several recent studies ([Barbosa et al., 2015](#); [Murakami et al., 2015](#); [Acosta-Cabronero et al., 2017](#)), we explored directly the patterns of iron distribution in the different forms of parkinsonism. Moreover, magnetic susceptibility changes that we observed in nigral and extranigral regions are concordant with the well-known pathological changes of these regions in AP rather than reflect physiological age-related iron deposition. Given the known correlation between age and progressive physiological increase of tissue susceptibility, the potential role of age as a confounding factor for the interpretation of our results was investigated. Our analysis included, as covariate, the effect of age, which was not significant,

A further limitation of the study is related to the elevated mean disease duration (> 5 years) of the PD subgroup. This effect could hide some significant correlation between nigrosome score and clinical scale (UPDRS III, H&Y and MMSE) and disease duration.

Relative advanced stage of PD disease may explain a reduced power of STS (*swallow tail sign*) as a biomarker for both, diagnosis and assessment of disease progression.

Another limitation of the study is the small number of MSA and RBD patients, mainly related to the low prevalence of these diseases, but also to the clinical characteristics and rapid disease progression for MSA. Even if QSM sequence enable to detect iron distribution in nigral and extranigral regions of the brain, in line with the pathological changes of the different forms of APS, the main benefit of the clinical use of this technique is the increase in sensitivity ([Massey LA et al., 2012](#)) rather than specificity. The increased susceptibility of putamen in MSA, for example, should be longitudinally evaluated as an early biomarker of neurodegeneration in the early forms of parkinsonisms .

FUTURE DIRECTIONS

PD disease is characterized by pathologically deposit of proteinaceous aggregates of α -synuclein in the form of Lewy bodies and Lewy neurites. These are thought to occur early in the brainstem, gradually spreading across vulnerable sites in the allocortex and temporal paralimbic cortex, before reaching prefrontal and sensory-association isocortex ([Braak et al., 2003](#)).

It should be noted, however, that the mechanisms that render certain neuronal populations vulnerable to degeneration are unclear; furthermore, the motor dysfunction in Parkinson's disease related to nigrostriatal degeneration is only one aspect of this multi-faceted disease that includes numerous non-motor and neurovegetative manifestations. For this reason new in vivo approaches, such as QSM sequence in MRI, will be useful and are now currently oriented to identify possible pathological mechanisms, not only in selected deep brain nuclei (ROIs), but **across the entire** Parkinson's disease **brain**. This concept also applies to the others parkinsonian groups explored in this study, especially in RBD group, as a interesting prodromic phase of α -synucleinopathy. In this condition impairments of neural circuit switching and imbalance between the inhibitory and excitatory

neuronal populations are likely responsible for episodic sleep disturbances. Animal studies have localised neuronal structures regulating REM sleep atonia, to the pontine sub-coeruleus nucleus and ventral medulla of the brainstem (Valencia Garcia et al., 2018; Weber et al., 2015), alongside the amygdala which is linked to the emotional content of dreams in humans.

Moreover, the potential mechanism of disease is linked to oxidative stress, due to excessive brain iron accumulation, but conclusive evidence incriminating free-iron mediated mechanisms as a primary cause rather than a secondary consequence of neurodegeneration in Parkinson's disease is lacking. Several studies have confirmed iron elevation in the substantia nigra pars compacta of post-mortem brains using histochemical (Dexter et al., 1991; Sofic et al., 1991) and X-ray methods (Popescu et al., 2009). However, generally limited to regions of interest (ROIs), and though several brain areas beyond the substantia nigra have been identified as having increased (Griffiths et al., 1999) or decreased (Dexter et al., 1991; Popescu et al., 2009) iron content, but global distribution of iron dysregulation in Parkinson's disease has not yet been elucidated. An interesting previous study (Acosta Cabronero et al., 2017) used a **whole-brain approach** for the first time to map the landscape of magnetostatic alterations in Parkinson's disease, **revealing QSM changes across the brainstem and cortex as well**. The authors identified QSM in the brainstem, at the level of rostral pons (including pyramidal tracts and pontine tegmental areas co-localized with the site of the locus coeruleus), at the superior cerebellar peduncle, caudal mesencephalon—seemingly spreading across pars compacta/ventral tegmental substantia nigra subregions and midbrain tegmental areas, possibly also including dorsal raphe and oculomotor nuclei. Parts of the temporal paralimbic, prefrontal and occipito-parietal cortex and, less markedly, insular and cerebellar areas were also involved.

These results, therefore, demonstrate the relevance of mapping the biochemical environment of the whole Parkinson's disease and parkinsonin syndromes brain

in vivo, and provide new insights into the behaviour of QSM as a disease biomarker. MRI's safe and non-invasive nature means, in addition, that QSM might be suitable for longitudinal monitoring in clinical trials of PD and AP disease.

BIBLIOGRAFIA

Acosta-Cabronero J, Cardenas-Blanco A, Betts MJ, Butryn M, Valdes-Herrera JP, Galazky I,

Nestor PJ.(2017)The whole-brain pattern of magnetic susceptibility perturbations in Parkinson's disease.

Brain Jan;140(1):118-131.doi: 10.1093/brain/aww278. Epub 2016 Nov 11.

Acta Radiol Feb;62(2):234-242. doi: 10.1177/0284185120920793.

Ahmed Z, Asi Y.T, Sailer A., Lees A.J, H. Houlden H, Revesz T., Holton J.L. (2012)

The neuropathology, pathophysiology and genetics of multiple system atrophy, Neuropathol. Appl. Neurobiol. 38 4–24. doi:10.1111/j.1365-2990.2011.01234

Andrews NC, Schmidt PJ. (2007) Iron homeostasis. Annu Rev Physiol; 69: 69–85.

doi: 10.1146/annurev.physiol.69.031905.164337

Arribarat G, De Barros A and Péran P (2020) Modern Brainstem MRI Techniques for the Diagnosis of Parkinson's Disease and Parkinsonisms. Front. Neurol. 11:791. doi: 10.3389/fneur.2020.00791

Atasoy HT, Nuyan O, Tunc T, Yorubulut M, Unal AE, Inan LE.(2004) T2-weighted MRI in Parkinson's disease; substantia nigra pars compacta hypointensity correlates with the clinical scores. Neurol. India; 52: 332–337.

Barbosa JHO, Santos AC, Tumas V, Liu MJ, Zheng WL, Haacke EM, Salmon CEG (2015); Quantifying brain iron deposition in patients with Parkinson's disease using quantitative susceptibility mapping, R2 and R2*. Magn. Reson. Imaging 2015; 33: 559–565. doi: 10.1016/j.mri.2015.02.021

Bastian TW, von Hohenberg WC, Mickelson DJ et al (2016) Iron Deficiency Impairs Developing Hippocampal Neuron Gene Expression, Energy Metabolism, and Dendrite Complexity. Dev Neurosci 38:264–276. <https://doi.org/10.1159/000448514>

Belaidi AA, Bush AI (2016) Iron neurochemistry in Alzheimer's disease and Parkinson's disease: targets for therapeutics. J Neurochem 139(Suppl 1):179–197. <https://doi.org/10.1111/jnc.13425>

Berg D, Gerlach M, Youdim M et al (2001) Brain iron pathways and their relevance to Parkinson's disease. J Neurochem 79:225–236 doi: 10.1046/j.1471-4159.2001.00608.x

Bishop GM, Dang TN, Dringen R et al (2011) Accumulation of non-transferrin-bound iron by neurons, astrocytes, and microglia. *Neurotox Res* 19:443–451. <https://doi.org/10.1007/s12640-010-9195-x>

Blazejewska AI, Schwarz ST, Pitiot A et al (2013) Visualization of nigrosome 1 and its loss in PD: pathoanatomical correlation and in vivo 7 T MRI. *Neurology* 81:534–540. <https://doi.org/10.1212/WNL.0b013e31829e6fd2>

Blystad I, Hakansson I, Tisell A, Ernerudh J, Smedby O, Lundberg P, Larsson EM. (2015) Quantitative MRI for analysis of active multiple sclerosis lesions without gadolinium-based contrast agent. *Am. J. Neuroradiol*; 37(1): 94–100. doi: [10.3174/ajnr.A4501](https://doi.org/10.3174/ajnr.A4501)

Boeve, B.F., (2010) REM sleep behavior disorder: Updated review of the core features, the REM sleep behavior disorder neurodegenerative disease association, evolving concepts, controversies, and future directions. *Ann. N. Y. Acad. Sci.* 1184, 15–54. doi: [10.1111/j.1749-6632.2009.05115.x](https://doi.org/10.1111/j.1749-6632.2009.05115.x)

Borie C Gasparini F, Verpillat P et al (2002) Association study between iron-related genes polymorphisms and Parkinson's disease. *J Neurol* 249:801–804. <https://doi.org/10.1007/s00415-002-0704-6>

Braak H, Del Tredici K, Rüb U, de Vos RAI, Steur ENHJ, Braak E. (2003) Staging of brain pathology related to sporadic Parkinson's disease. *Neurobiol Aging* 24:197–211. doi: [10.1016/S0197-4580\(02\)00065-9](https://doi.org/10.1016/S0197-4580(02)00065-9)

Brown R.W, Norman Cheng Y.C, Haacke E.C, Thompson M.R and Venkatesan R. *Magnetic Resonance Imaging: Physical Principles and Sequence Design*. 2nd edition, 2014.

Calloni SF, Conte G, Sbaraini S, et al. (2018) Multiparametric MR imaging of Parkinsonisms at 3 Tesla: Its role in the differentiation of idiopathic Parkinson's disease versus atypical Parkinsonian disorders. *Eur J Radiol*;109:95–100. doi [10.1016/j.ejrad.2018.10.032](https://doi.org/10.1016/j.ejrad.2018.10.032)

Carpenter KL, Li W, Wei H, et al. (2016) Magnetic susceptibility of brain iron is associated with childhood spatial IQ. *NeuroImage*; 132:167–174. doi: [10.1016/j.neuroimage.2016.02.028](https://doi.org/10.1016/j.neuroimage.2016.02.028)

Chandran AS, Bynevelt M, Lind CR. (2015) Magnetic resonance imaging of the subthalamic nucleus for deep brain stimulation. *J. Neurosurg*; 1–10. doi: [10.3171/2015.1.JNS142066](https://doi.org/10.3171/2015.1.JNS142066)

Chandran AS, Bynevelt M, Lind CR. (2016) Magnetic resonance imaging of the subthalamic nucleus for deep brain stimulation. *J. Neurosurg*; 124: 96–105 doi: [10.3171/2015.1.JNS142066](https://doi.org/10.3171/2015.1.JNS142066)

Chen W, Gautier SA, Gupta A et al (2014) Quantitative susceptibility mapping of multiple sclerosis lesions at various ages at various ages. *Radiology*; 271: 183–192.

doi: [10.1148/radiol.13130353](https://doi.org/10.1148/radiol.13130353)

Chen W, Zhu W, Kovanlikaya I, et al. (2014) Intracranial calcifications and hemorrhages: characterization with quantitative susceptibility mapping. *Radiology*; 270(2):496–505. Doi: [10.1148/radiol.13122640](https://doi.org/10.1148/radiol.13122640)

Collins C.M, B. Yang, Q.X. Yang, and M.B.Smith (2002). Numerical calculations of the static magnetic field in three-dimensional multi-tissue models of the human head. *Magnetic Resonance Imaging*, 20:413–424, 2002 DOI: [10.1016/s0730-725x\(02\)00507-6](https://doi.org/10.1016/s0730-725x(02)00507-6)

Colton CA, Gilbert DL (1987) Production of superoxide anions by a CNS macrophage, the microglia. *FEBS Lett* 223:284–288

Conde JR, Streit WJ (2006) Microglia in the aging brain. *J Neuropathol Exp Neurol* 65:199–203. <https://doi.org/10.1097/01.jnen.0000202887.22082.63>

Cosottini M, Frosini D, Pesaresi I et al (2014) MR imaging of the substantia nigra at 7 T enables diagnosis of Parkinson disease. *Radiology* 2014 271:831–838. <https://doi.org/10.1148/radiol.14131448>

Cosottini, M., Frosini, D., Pesaresi, I., et al (2015). Comparison of 3T and 7T susceptibility-weighted angiography of the substantia nigra in diagnosing Parkinson disease. *Am. J. Neuroradiol.* 36 (3), 461–466. <https://doi.org/10.3174/ajnr.A4158>.

Damier, P., Hirsch, et al (1999) E.C., Agid, Y., Graybiel, A.M., 1999 b. The substantia nigra of the human brain. II. Patterns of loss of dopamine-containing neurons in Parkinson's disease. *Brain* 122, 1437–1448

Darrel D.H et al, *NeuroImage: Clinical* 20 (2018) 365–373

de Rochefort L, Liu T, Kressler B, et al (2010). Quantitative susceptibility map reconstruction from MRphase data using bayesian regularization: validation and application to brain imaging. *Magn Reson Med.*; 63(1):194–206. doi: [10.1002/mrm.22187](https://doi.org/10.1002/mrm.22187)

Deistung A, Schweser F, Wiestler B, et al. (2013) Quantitative susceptibility mapping differentiates between blood depositions and calcifications in patients with glioblastoma. *PLoS One.* 2013; 8(3):e57924. doi: [10.1371/journal.pone.0057924](https://doi.org/10.1371/journal.pone.0057924)

Deistung A., Schweser R., and Reichenbach J.R. (2017) Overview of quantitative susceptibility mapping. *NMR in Biomedicine*, 30, DOI: [10.1002/nbm.3569](https://doi.org/10.1002/nbm.3569)

Devos D, Moreau C, Devedjian JC, Kluza J, Petrault M, Laloux C, Jonneaux A, Ryckewaert G et al , Garcon G, Rouaix N, Duhamel A, Jissendi P, Dujardin K, Auger F, Ravasi L, Hopes L, Grolez G, Firdaus W, Sablonniere B, Strubi-Vuillaume I, Zahr N, Destee A, Corvol JC, Poltl D, Leist M, Rose C, Defebvre L, Marchetti P, Cabantchik ZI, Bordet R. (2014) Targeting chelatable iron as a therapeutic modality in Parkinson's disease. *Antioxid. Redox Signal.*; 21: 195–210. doi: [10.1089/ars.2013.5593](https://doi.org/10.1089/ars.2013.5593)

Dexter DT, Wells FR, Lees AJ et al (1989) Increased nigral iron content and alterations in other metal ions occurring in brain in Parkinson's disease. *J Neurochem* 52:1830–1836. <https://doi.org/10.1111/j.1471-4159.1989.tb07264.x>

Dexter D T, Carayon A, Javoy Agid (1991) Alterations in the levels of iron, ferritin and other trace metals in Parkinson's disease and other neurodegenerative diseases affecting the basal ganglia *Brain* Aug;114 (Pt 4):1953-75. doi: [10.1093/brain/114.4.1953](https://doi.org/10.1093/brain/114.4.1953).

Dickson DW (2012) Parkinson's disease and parkinsonism: neuropathology. *Cold Spring Harb Perspect Med.* 2012 Aug 1;2(8):a009258. doi: [10.1101/cshperspect.a009258](https://doi.org/10.1101/cshperspect.a009258). PMID: 22908195

Dringen R, Bishop GM, Koeppe M, Dang TN, Robinson SR (2007). The pivotal role of astrocytes in the metabolism of iron in the brain. *Neurochem Res*; 32: 1884–90 DOI: [10.1007/s11064-007-9375-0](https://doi.org/10.1007/s11064-007-9375-0)

Du G, Liu T, Lewis MM, Kong L, Wang Y, Connor J, Mailman RB, Huang X (2016). Quantitative susceptibility mapping of the midbrain in Parkinson's disease. *Mov. Disord.*; 31: 317–324

Earle KM (1968) Studies on Parkinson's disease including x-ray fluorescent spectroscopy of formalin fixed brain tissue. *J Neuropathol Exp Neurol* 27:1–14. <https://doi.org/10.1097/00005072-196801000-00001>

Ekstein K, Dymerska B, Bachrata B. et al (2018) Computationally Efficient Combination of Multi-channel Phase Data From Multi-echo Acquisitions (ASPIRE) *Magn Reson Med* Jun;79(6):2996-3006. doi: 10.1002/mrm.26963

Eskreis-Winkler S, Zhang Y, Zhang J et al. (2016) The clinical utility of QSM: disease diagnosis, medical management, and surgical planning *NMR in Biomedicine* *NMR Biomed* 2017 Apr;30(4). doi: 10.1002/nbm.3668. Epub 2016 Dec 1.

Eskreis-Winkler S, Deh K, Gupta A, Liu T, Wisnieff C, Jin M, Gauthier SA, Wang Y, Spincemaille P. (2015) Multiple sclerosis lesion geometry in quantitative susceptibility mapping (QSM) and phase imaging. *J. Magn. Reson. Imaging* 42: 224–229. doi: [10.1002/jmri.24745](https://doi.org/10.1002/jmri.24745)

Evens. L.C. *Partial Differential Equations*. American Mathematical Society: Providence, Rhode Island, 2nd edition, 2010.

Fan AP, Bilgic B, Gagnon L, Witzel T, Bhat H, Rosen BR, Adalsteinsson E. Quantitative oxygenation venography from MRI phase. *Magn. Reson. Med.* 2014; 72: 149–159.

Fanciulli A , Stankovic I, Krismer F et al. 2019 Multiple system atrophy *nt Rev Neurobiol* 2019;149:137-192. doi: 10.1016/bs.irn.2019.10.004.

Fearnley JM, Lees AJ (1991) Ageing and Parkinson's disease: substantia nigra regional selectivity. *Brain*. Oct;114 (Pt 5):2283-301. doi: 10.1093/brain/114.5.2283.

Fiscione C Testa C Evangelisti F, Bianchini C , Bartiromo F, , Lodi R, Tonon C, Nigrosome-1 Detection in Quantitative Susceptibility Mapping: Contrast Optimization with 64-channel Coil Poster Congresso RIN 8-9 luglio 2020

Friedrich I., Reimann K., Jankuhn S et al (2021) Cell specific quantitative iron mapping on brain slices by immuno- μ PIXE in healthy elderly and Parkinson's disease *Acta neuropathol commun* 9:47 <https://doi.org/10.1186/s40478-021-01145-2>

Frosini D, Ceravolo R, Tosetti et al (2016) Nigral involvement in atypical parkinsonisms: evidence from a pilot study with ultra field MRI *J. Neural Transm (Vienna)*. 2016 May;123(5):509-13. doi: 10.1007/s00702-016-1529-2.

Wenning, G.K, Colosimo C, Geser, W. Poewe, Multiple system atrophy, *Lancet Neurol.* 3 (2004) 93–103

Galazka-Friedman J, Bauminger ER, Friedman A et al (1996) Iron in parkinsonian and control substantia nigra—a Mössbauer spectroscopy study. *Mov Disord* 11:8–16. <https://doi.org/10.1002/mds.870110104>
Gelb DJ, Oliver E, Gilman S. (1999) Diagnostic criteria for Parkinson disease. *Arch Neurol.*;56:33–39 DOI: [10.1001/archneur.56.1.33](https://doi.org/10.1001/archneur.56.1.33) doi: 10.1212/01.wnl.0000324625.00404.15.

Gerlach M et al 2010 Ben-Shachar D, Riederer P et al (1994) Altered brain metabolism of iron as a cause of neurodegenerative diseases? *J Neurochem* 63:793–807. <https://doi.org/10.1046/j.1471-4159.1994.63030793>.

Gilman S, Wenning GK, Low PA, et al (2008) Second consensus statement on the diagnosis of multiple system atrophy. *Neurology*;71:670–676

Gross RE, Krack P, Rodriguez-Oroz MC, Rezai AR, Benabid AL. (2006) Electrophysiological mapping for the implantation of deep brain stimulators for Parkinson's disease and tremor. *Mov. Disord.*; 21(Suppl. 14): S259–S283 DOI: [10.1002/mds.20960](https://doi.org/10.1002/mds.20960)

Gupta D, Saini J, Kesavadas C, et al. Utility of susceptibility weighted MRI in differentiating

Haacke EM, Liu S, Buch S, Zheng W, Wu D, Ye Y. (2015) Quantitative susceptibility mapping: current status and future directions. *Magnetic resonance imaging*; 33(1):1–25

Haacke EM, Makki M, Ge Y, Maheshwari M, Sehgal V, Hu J, Selvan M, Wu Z, Latif Z, Xuan Y, Khan O, Garbern J, Grossman RI (2009) Characterizing iron deposition in multiple sclerosis lesions using susceptibility weighted imaging. *J. Magn. Reson. Imaging* 2009; 29: 537–544. doi: [10.1002/jmri.21676](https://doi.org/10.1002/jmri.21676)

Haacke EM, Tang J, Neelavalli J, Cheng YCN (2010) Susceptibility mapping as a means to visualize veins and quantify oxygen saturation. *J. Magn. Reson. Imaging*; 32: 663–676. doi: [10.1002/jmri.22276](https://doi.org/10.1002/jmri.22276)

Haacke, E.M. Xu Y., Cheng Y.N, and Reichenbach R. (2004). Susceptibility Weighted Imaging (SWI). *Magnetic Resonance in Medicine*, 52:612–618. DOI: [10.1002/mrm.20198](https://doi.org/10.1002/mrm.20198)

Haacke, EM., Reichenbach, JrR (2011). Susceptibility weighted imaging in MRI : basic concepts and clinical applications. Vol. xvi. Hoboken, N.J: Wiley-Blackwell;. p. 743

Halliday G, Holtin J L et al., (2011) Neuropathology underlying clinical variability in patients with synucleinopathies *Acta Neuropathol* Aug;122(2):187-204. doi: [10.1007/s00401-011-0852-9](https://doi.org/10.1007/s00401-011-0852-9).

Hametner S, Wimmer I, Haider L, Pfeifenbring S, Brück W, Lassmann H (2013) Iron and neurodegeneration in the multiple sclerosis brain. *Ann. Neurol*; 74: 848–861
doi: [10.1002/ana.23974](https://doi.org/10.1002/ana.23974)

Harder SL, Hopp KM, Ward H, Neglio H, Gitlin J, Kido D (2008) Mineralization of the deep gray matter with age: a retrospective review with susceptibility-weighted MR imaging. *AJNR* 29:176–183
doi: [10.3174/ajnr.A0770](https://doi.org/10.3174/ajnr.A0770)

Hare D, Ayton S, Bush A et al (2013) A delicate balance: Iron metabolism and diseases of the brain. *Front Aging Neurosci* 5:34. <https://doi.org/10.3389/fnagi.2013.00034>

Harrison TR, Hauser SL, Josephson SA. *Harrison's Neurology in Clinical Medicine*. McGraw-Hill: New York, 2010.

He N, et Ling H, Ding B, et al.(2015) Region-specific disturbed iron distribution in early idiopathic Parkinson's disease measured by quantitative susceptibility mapping. *Hum Brain Mapp*. 2015; 36(11):4407–4420.

Hentze MW, Muckenthaler MU, Galy B, Camaschella C (2010) Two to tango: regulation of Mammalian iron metabolism. *Cell*; 142: 24–38. doi: [10.1016/j.cell.2010.06.028](https://doi.org/10.1016/j.cell.2010.06.028)

Hirsch EC, Brandel JP, Galle P et al (1991) Iron and aluminum increase in the substantia nigra of patients with Parkinson's disease: an X-ray microanalysis. *J Neurochem* 56:446–451. <https://doi.org/10.1111/j.1471-4159.1991.tb08170.x>

J Neural Transm Suppl 20:145–155. https://doi.org/10.1007/978-3-7091-0643-3_8

Huang E, Ong WY, Go ML, Connor JR (2006). Upregulation of iron regulatory proteins and divalent metal transporter-1 isoforms in the rat hippocampus after kainate induced neuronal injury. *Exp Brain Res*; 170: 376–86.

Jahanshad N, Rajagopalan P, Thompson PM (2013) Neuroimaging, nutrition, and iron-related genes. *Cell Mol Life Sci* 70:4449–4461. <https://doi.org/10.1007/s00018-013-1369-2>

Jellinger K, Paulus W, Grundke-Iqbal I et al (1990) Brain iron and ferritin in Parkinson's and Alzheimer's diseases. *J Neural Transm Park Dis Dement Sect* 2:327–340. <https://doi.org/10.1007/BF02252926>

Jeong SY, David S. (2003) Glycosylphosphatidylinositol-anchored ceruloplasmin is required for iron efflux from cells in the central nervous system. *J Biol Chem*; 278: 27144–48. doi: [10.1074/jbc.M301988200](https://doi.org/10.1074/jbc.M301988200)

Jin L, Wang J, Wang C, et al.(2019) Combined visualization of nigrosome-1 and neuromelanin in the substantia nigra using 3T MRI for the differential diagnosis of essential tremor and de novo Parkinson's disease. *Front Neurol*;10:100. doi: [10.3389/fneur.2019.00100](https://doi.org/10.3389/fneur.2019.00100)

Jomova K, Vondrakova D, Lawson M et al (2010) Metals, oxidative stress and neurodegenerative disorders. *Mol Cell Biochem* 345:91–104. <https://doi.org/10.1007/s11010-010-0563-x>

Kanda T, Osawa M, Oba H, Toyoda K, Kotoku J, Haruyama T, Takeshita K, Furui S. (2015) High signal intensity in dentate nucleus on unenhanced T1-weighted MR images: association with linear versus macrocyclic gadolinium chelate administration. *Radiology*; 275(3): 40364. doi: [10.1148/radiol.14140364](https://doi.org/10.1148/radiol.14140364)

Ke Y, Qian ZM (2007) Brain iron metabolism: neurobiology and neurochemistry. *Prog Neurobiol*; 83: 149–73. doi: [10.1016/j.pneurobio.2007.07.009](https://doi.org/10.1016/j.pneurobio.2007.07.009)

Koga S, Aoki N, Uitti RJ, et al. (2015) When DLB, PD, and PSP masquerade as MSA: an autopsy study of 134 patients. *Neurology* ; 85:404–412. DOI: [10.1212/WNL.0000000000001807](https://doi.org/10.1212/WNL.0000000000001807)

Konno T, Deuschlander A, Heckman MG et al., (2018) Comparison of clinical features among Parkinson's disease subtypes: A large retrospective study in a single center *J Neurol Sci* Mar 15;386:39-45. doi: [10.1016/j.jns.2018.01.013](https://doi.org/10.1016/j.jns.2018.01.013)

Kraft E, Trenkwalder C, Auer PD (2002) T2*-weighted MRI differentiates multiple system atrophy from Parkinson's disease. *Neurology* 59:1265–1267

Kutzelnigg A, Lassmann H. (2014) Pathology of multiple sclerosis and related inflammatory demyelinating diseases. *Handb. Clin. Neurol*; 122: 15–58. doi: [10.1016/B978-0-444-52001-2.00002-9](https://doi.org/10.1016/B978-0-444-52001-2.00002-9)

Kwon D-H, Kim J-M, Oh S-H et al (2012) Seven-Tesla magnetic resonance images of the substantia nigra in Parkinson disease. *Ann Neurol* 71:267–277. <https://doi.org/10.1002/ana.22592>

Langkammer C, Pirpamer L, Seiler S, et al (2016). Quantitative Susceptibility Mapping in Parkinson's Disease. *PLoS One*. 2016; 11(9):e0162460. DOI: [10.1371/journal.pone.0162460](https://doi.org/10.1371/journal.pone.0162460)

Lassmann H. (2011) Pathophysiology of inflammation and tissue injury in multiple sclerosis: what are the targets for therapy. *J. Neurol. Sci*; 306: 167–169. doi: [10.1016/j.jns.2010.07.023](https://doi.org/10.1016/j.jns.2010.07.023)

C. Laule, I.M. Vavasour, S.H. Kolind, D.K.B. Li, T.L. Traboulsee, G.R.W. Moore, and A.L. MacKey. Magnetic Resonance Imaging of Myelin. *Neurotherapeutics*, 4(3):460–484, 2007.

Lee SH, Ryu WS, Roh JK. (2009) Cerebral microbleeds are a risk factor for warfarin-related intracerebral hemorrhage. *Neurology* ; 72(2):171–176. doi: [10.1212/01.wnl.0000339060.11702.dd](https://doi.org/10.1212/01.wnl.0000339060.11702.dd)

Leitner DF, Connor JR. Functional roles of transferrin in the brain. *Biochim Biophys*

Acta 2012; 1820: 393–402. doi: [10.1016/j.bbagen.2011.10.016](https://doi.org/10.1016/j.bbagen.2011.10.016)

Li J, Chang S, Liu T et al (2015) Phase-corrected bipolar gradients in multi-echo gradient-echo sequences for quantitative susceptibility mapping *MAGMA* 2015 Aug;28(4):347-55. doi: [10.1007/s10334-014-0470-3](https://doi.org/10.1007/s10334-014-0470-3).

Li X, Allen RP, Earley CJ, et al. Brain iron deficiency in idiopathic restless legs syndrome measured by quantitative magnetic susceptibility at 7 Tesla. *Sleep Med.* 2016; 22:75–82. doi [10.1016/j.sleep.2016.05.001](https://doi.org/10.1016/j.sleep.2016.05.001)

Li X, Vikram DS, Lim IA, Jones CK, Farrell JA, van Zijl PC (2012) Mapping magnetic susceptibility anisotropies of white matter in vivo in the human brain at 7 T. *NeuroImage*; 62: 314–330.doi: [10.1016/j.neuroimage.2012.04.042](https://doi.org/10.1016/j.neuroimage.2012.04.042)

Liu C, W. Li, K.A. Tong, K.W. Yeom, and S. Kuzminski (2015). Susceptibility-Weighted Imaging and Quantitative Susceptibility Mapping in the Brain. *Journal of Magnetic Resonance Imaging*, 42:23–41. doi: [10.1002/jmri.24768](https://doi.org/10.1002/jmri.24768)

Liu T, Eskreis-Winkler S, Schweitzer AD, Chen WW, Kaplitt MG, Tsiouris AJ, Wang Y. Improved subthalamic nucleus depiction with quantitative susceptibility mapping. *Radiology* 2013; 269: 216–223.

Liu T, Khalidov I., L. de Rochefort, P. Spincemaille, J. Liu, A.J. Tsiouris, and Y. Wang (2011). A novel background field removal method for MRI using projection onto dipole fields. *NMR in Biomedicine*, 24:1129–1136, 2011. doi: [10.1002/nbm.1670](https://doi.org/10.1002/nbm.1670)

Liu T, Surapaneni K, Lou M, Cheng L, Spincemaille P, Wang Y (2012) Cerebral microbleeds: burden assessment by using quantitative susceptibility mapping. *Radiology*; 262(1):269–278. doi: [10.1148/radiol.11110251](https://doi.org/10.1148/radiol.11110251)

Liu T., Spincemaille P. , L. de Rochefort, Kressler B, and Wang y . Calculation of Susceptibility Through Multiple Orientation Sampling (COSMOS): A Method for Conditioning the Inverse Problem From Measured Magnetic Field Map to Susceptibility Source Image in MRI. *Magnetic Resonance in Medicine*, 61:196–204, 2009.

Liu W, Soderlund K, Senseney JS, et al. (2016) Imaging Cerebral Microhemorrhages in Military Service Members with Chronic Traumatic Brain Injury. *Radiology*. 2016; 278(2):536–545. doi: [10.1148/radiol.2015150160](https://doi.org/10.1148/radiol.2015150160)

Liu X, Wang N, Chen C, Wu PY, Piao S, et al (2020) Swallow tail sign on susceptibility map-weighted imaging (SMWI) for disease diagnosing and severity evaluating in parkinsonism.

doi [10.1177/0284185120920793](https://doi.org/10.1177/0284185120920793)

Liu X, Wang N, Chen C, Wu PY, Piao S, et al (2021) Swallow tail sign on susceptibility map-weighted imaging (SMWI) for disease diagnosing and severity evaluating in parkinsonism. *Acta Radiol* Feb;62(2):234-242. doi: 10.1177/0284185120920793. Epub 2020 May 7. PMID: 32380911

Lo CP, Kao HW, Chen SY, Chu CM, Hsu CC, Chen YC, Lin WC, Liu DW, Hsu WL (2014). Comparison of diffusion-weighted imaging and contrast-enhanced T1-weighted imaging on a single baseline MRI for demonstrating dissemination in time in multiple sclerosis. *BMC Neurol*. 2014; 14: 100. doi [10.1186/1471-2377-14-100](https://doi.org/10.1186/1471-2377-14-100)

Lu W, Wu B, and Liu C (2012) Quantitative susceptibility mapping of human brain reflects spatial variations in tissue composition. *Neuroimage*, 59:2625–2635, 2012.

doi: [10.1016/j.neuroimage.2011.08.077](https://doi.org/10.1016/j.neuroimage.2011.08.077)

Mann VM, Cooper JM, Daniel SE et al (1994) Complex I, iron, and ferritin in Parkinson's disease substantia nigra. *Ann Neurol* 36:876–881. <https://doi.org/10.1002/ana.410360612>

Massey L.A et al 2017 9.4 T MR microscopy of the substantia nigra with pathological validation in controls and disease *NeuroImage: Clinical* 13 (2017) 154–163). doi: [10.1016/j.nicl.2016.11.015](https://doi.org/10.1016/j.nicl.2016.11.015)

Massey L.A et al., 2012 Conventional magnetic resonance imaging in confirmed progressive supranuclear palsy and multiple system atrophy *Mov Disord* 2012

Dec;27(14):1754-62. doi: [10.1002/mds.24968](https://doi.org/10.1002/mds.24968)..

Mastroberardino PG, Hoffman EK, Horowitz MP et al (2009) A novel transferrin/TfR2-mediated mitochondrial iron transport system is disrupted in Parkinson's disease. *Neurobiol Dis* 34:417–431. <https://doi.org/10.1016/j.nbd.2009.02.009>

Mehlhase J, Gieche J, Widmer R et al (2006) Ferritin levels in microglia depend upon activation: modulation by reactive oxygen species. *Biochim Biophys Acta* 1763:854–859. <https://doi.org/10.1016/j.bbamcr.2006.04.012>

Mehlhase J, Sandig G, Pantopoulos K et al (2005) Oxidation-induced ferritin turnover in microglial cells: role of proteasome. *Free Radic Biol Med* 38:276–285. <https://doi.org/10.1016/j.freeradbiomed.2004.10.025>

Mehta V, Pei W, Yang G, Li S, Swamy E, Boster A, Schmalbrock P, Pitt D.(2013) Iron is a sensitive biomarker for inflammation in multiple sclerosis lesions. *PLoS ONE*; 8: 1–10.

Mejer FJA, van Rumund A, Fasen ABA et al.(2015) Susceptibility-weighted imaging improves the diagnostic accuracy of 3T brain MRI in the work-up of parkinsonism *AJNR Am J Neuroradiol Mar*; 36(3):454-60. doi [10.3174/ajnr.A4140](https://doi.org/10.3174/ajnr.A4140)

Michel JB, Virmani R, et al Arbustini E, Pasterkamp G. Intraplaque haemorrhages as the trigger of plaque vulnerability. *Eur Heart J*. 2011; 32(16):1977–1985. 1985a, 1985b, 1985c. doi: [10.1093/eurheartj/ehr054](https://doi.org/10.1093/eurheartj/ehr054)

Miki Y, Foti SC, Asi YT, et al. Improving diagnostic accuracy of multiple system atrophy: a clinico-pathological study. *Brain* 2019; 142:2813–2827. doi: [10.1093/brain/awz189](https://doi.org/10.1093/brain/awz189)

Mills E, Dong XP, Wang F, Xu H. (2010) Mechanisms of brain iron transport: insight into neurodegeneration and CNS disorders. *Future Med Chem*; 2: 51–64. doi: [10.4155/fmc.09.140](https://doi.org/10.4155/fmc.09.140)

Möller HE, Bossoni L, Connor JR et al (2019) Iron, Myelin, and the Brain: Neuroimaging Meets Neurobiology. *Trends Neurosci* 42:384–401. <https://doi.org/10.1016/j.tins.2019.03.009>

Moon T.K. and Stirling W.C. (2000) Pseudoinverses and the SVD. *Mathematical Methods and Algorithms for Signal Processing*. Prentice Hall: Upper Saddle River, New Jersey, pp. 116-117

Moos T, Morgan EH. (2000) Transferrin and transferrin receptor function in brain barrier systems. *Cell Mol Neurobiol*; 20: 77–95. doi: [10.1023/a:1006948027674](https://doi.org/10.1023/a:1006948027674)

Moos T, Rosengren Nielsen T, Skjørringe T, Morgan EH (2007) Iron trafficking inside the brain. *J Neurochem* 2007; 103: 1730–40. DOI: [10.1111/j.1471-4159.2007.04976.x](https://doi.org/10.1111/j.1471-4159.2007.04976.x)

Murakami Y, Kakeda S, Watanabe K, Ueda I, Ogasawara A, Moriya J, Ide S, Futatsuya K, Sato T, Okada K, Uozumi T, Tsuji S, Liu T, Wang Y, Korogi Y.(2015)

Usefulness of quantitative susceptibility mapping for the diagnosis of Parkinson disease.

Am. J. Neuroradiol; 36: 1102–1108. doi: [10.3174/ajnr.A4260](https://doi.org/10.3174/ajnr.A4260)

Nandigam RN, Viswanathan A, Delgado P, et al. (2009) MR imaging detection of cerebral microbleeds: effect of susceptibility-weighted imaging, section thickness, and field strength. AJNR Am J Neuroradiol;30:338–43

Naying H, Pei H et al Dentate nucleus iron deposition is a potential biomarker for tremor-dominant Parkinson's disease NMR Biomed. 2017 April ; 30(4): . doi:10.1002/nbm.3554.

Nijeholt GJ, van Walderveen MA, Castelijns JA, van Waesberghe JH, Polman C, Scheltens P, Rosier PF, Jongen PJ, Barkhof F. (1998) Brain and spinal cord abnormalities in multiple sclerosis. Correlation between MRI parameters, clinical subtypes and symptoms. Brain ; 121 (4): 687–697. doi: [10.1093/brain/121.4.687](https://doi.org/10.1093/brain/121.4.687)

Persson NN, Wu J, Zhang Q et al.(2015) Age and sex related differences in subcortical brain iron concentrations among healthy adults Neuroimage Nov 15;122:385-98.doi: 10.1016/j.neuroimage.2015.07.050. Epub 2015 Jul 26.

Pivina L, Semenova Y, Doşa MD et al (2019) Iron Deficiency, Cognitive Functions, and Neurobehavioral Disorders in Children. J Mol Neurosci 68:1–10. <https://doi.org/10.1007/s12031-019-01276-1>

Plantinga BR, Temel Y, Roebroek A, Uludag K, Ivanov D, Kuijf ML, Ter Haar Romeeho BM. Ultra-high field magnetic resonance imaging of the basal ganglia and related structures. Front. Hum. Neurosci. 2014; 8: 876.

Qian Z et al (1997) Brain iron and neurological disorders. Chin Med J (Engl) 110:455–458 Thompson KJ,

Shoham S, Connor JR (2001) Iron and neurodegenerative disorders. Brain Res Bull 55:155–164. [https://doi.org/10.1016/s0361-9230\(01\)00510-x](https://doi.org/10.1016/s0361-9230(01)00510-x)

Quattrone A , Nicoletti G., Messina D et al Radiology (2008) MR imaging index for differentiation of progressive supranuclear palsy from Parkinson disease and the Parkinson variant of multiple system atrophy Radiology Jan;246(1):214-21. doi: 10.1148/radiol.2453061703.

Radbruch A, Weberling LD, Kieslich PJ, Eidel O, Burth S, Kickingereder P, Heiland S, Wick W, Schlemmer HP, Bendszus M (2015) Gadolinium retention in the dentate nucleus and globus pallidus is dependent on the class of contrast agent. *Radiology*; 275 (3): 150337. doi: [10.1148/radiol.2015150337](https://doi.org/10.1148/radiol.2015150337)

Ramos P; Santos A.Pinto NR et al (2014) **Iron** levels in the human brain: a post-mortem study of anatomical region differences and age-related changes. *J Trace Elem Med Biol.* Jan;28(1):13-7. doi: [10.1016/j.jtemb.2013.08.001](https://doi.org/10.1016/j.jtemb.2013.08.001).

Reichenbach JR, Schweser F, Serres B, Deistung A. (2015) Quantitative Susceptibility Mapping: Concepts and Applications. *Clin Neuroradiol.*; 25(2):225–230. doi [10.1007/s00062-015-0432-9](https://doi.org/10.1007/s00062-015-0432-9)

Reinert A, Morawski M, Seeger J et al (2019) Iron concentrations in neurons and glial cells with estimates on ferritin concentrations. *BMC Neurosci* 20:25. <https://doi.org/10.1186/s12868-019-0507-7>

Reinert T, Andrea T, Barapatre N et al (2011) Biomedical research at LIPSION – Present state and future developments. *Nucl Instrum Methods Phys Res, Sect B* 269:2254–2259. <https://doi.org/10.1016/j.nimb.2011.02.071>

Reiter E, Mueller C, Pinter B, et al. (2015) Dorsolateral nigral hyperintensity on 3.0T susceptibility-weighted imaging in neurodegenerative Parkinsonism. *Mov Disord* ;30:1068–1076. doi : [10.1002/mds.26171](https://doi.org/10.1002/mds.26171)

Richter EO, Hoque T, Halliday W, Lozano AM, Saint-Cyr JA. (2004) Determining the position and size of the subthalamic nucleus based on magnetic resonance imaging results in patients with advanced Parkinson disease. *J. Neurosurg.*; 100: 541–546 doi: [10.3171/jns.2004.100.3.0541](https://doi.org/10.3171/jns.2004.100.3.0541)

Riederer P, Sofic E, Rausch WD et al (1989) Transition metals, ferritin, glutathione, and ascorbic acid in parkinsonian brains. *J Neurochem* 52:515–520. <https://doi.org/10.1111/j.1471-4159.1989.tb09150.x>
Robinson DS, Bredies K, Khapipova D et al., (2017) An illustrated comparison of processing methods for MR phase imaging and QSM: combining array coil signals and phase unwrapping *NMR Biomed* Apr;30(4):e3601 doi: [10.1002/nbm.3601](https://doi.org/10.1002/nbm.3601)

Roccatagliata L, Vuolo L, Bonzano L, Pichiecchio A, Mancardi GL. (2009) Multiple sclerosis: hyperintense dentate nucleus on unenhanced T1-weighted MR images is associated with the secondary progressive subtype. *Radiology* 2009; 251: 503–510. doi: [10.1148/radiol.2511081269](https://doi.org/10.1148/radiol.2511081269)

Rudko DA, Solovey I, Gati JS, Kremenutzky M, Menon RS. Multiple sclerosis: improved identification of disease-relevant changes in gray and white matter by using susceptibility-based MR imaging. *Radiology* 2014; 272: 851–864. doi: [10.1148/radiol.14132475](https://doi.org/10.1148/radiol.14132475)

Wharton S. and Bowtell R. (2010) Whole-brain susceptibility mapping at high field: A comparison of multiple- and single-orientation methods. *NeuroImage*, 53:515–525
doi: [10.1016/j.neuroimage.2010.06.070](https://doi.org/10.1016/j.neuroimage.2010.06.070)

Sanchis-Segura C et al. (2019) Sex differences in gray matter volume: how many and how large are they really?, *Biology of Sex Differences* 10-32

Schaefer A, Forstmann BU, Neumann J, Wharton S, Mietke A, Bowtell R, Turner R.(2012) Direct visualization of the subthalamic nucleus and its iron distribution using high-resolution susceptibility mapping. *Hum. Brain Mapp.*; 33: 2831–2842

Schenck F. Safety of Strong, Static Magnetic Fields. (2000) *Journal of Magnetic Resonance Imaging*, 12:2–19. doi: [10.1002/1522-2586\(200007\)12:1<2::aid-jmri2>3.0.co;2-v](https://doi.org/10.1002/1522-2586(200007)12:1<2::aid-jmri2>3.0.co;2-v)

Schofield M and Zhu Y (2003) Fast phase unwrapping algorithm for interferometric applications. *Optics Letters*, 28:1194–1196
doi: [10.1364/ol.28.001194](https://doi.org/10.1364/ol.28.001194)

Schweser F, Deistung A, Lehr BW, Reichenbach JR. (2010) Differentiation between diamagnetic and paramagnetic cerebral lesions based on magnetic susceptibility mapping. *Med. Phys.* 2010; 37: 5165–5178.
doi: [10.1118/1.3481505](https://doi.org/10.1118/1.3481505)

Seteja M 2014 *International Classification of Sleep Disorders (3rd Edition) (ICSD-3)*

Shafir T, Angulo-Barroso R, Jing Y et al (2008) Iron deficiency and infant motor development. *Early Hum Dev* 84:479–485.
<https://doi.org/10.1016/j.earlhumdev.2007.12.009>

Shinohara RT, Goldsmith J, Mateen FJ, Crainiceanu C, Reich DS (2012) Predicting breakdown of the blood–brain barrier in multiple sclerosis without contrast agents. *Am. J. Neuroradiol*; 33: 1586–1590.doi: [10.3174/ajnr.A2997](https://doi.org/10.3174/ajnr.A2997)

Sjostrom et al 2019 The current trend in research is to move away from the arbitrary signal intensities on standard SWI to phase-based QSM, which provides a quantitative estimate of tissue susceptibility levels by deconvoluting the tissue phase with a dipole kernel

Sofic E, Riederer P, Heinsen H et al (1988) Increased iron (III) and total iron content in post mortem substantia nigra of parkinsonian brain. *J Neural Transm* 74:199–205. <https://doi.org/10.1007/BF01244786>

Stezin A, Naduthota RM, Botta R, et al. Clinical utility of visualisation of nigrosome-1 in patients with Parkinson’s disease. *Eur Radiol* 2018;28:718–726.

Sun H, Kate M, Gioia LC, Emery DJ, Butcher K, Wilman AH (2016) Quantitative susceptibility mapping using a superposed dipole inversion method: Application to intracranial hemorrhage. *Magn Reson Med*. 2016; 76(3):781–791. [doi: 10.1002/mrm.25919](https://doi.org/10.1002/mrm.25919)

Sun H. and Wilman A.H.. Background Field Removal Using Spherical Mean Value Filtering and Tikhonov Regularization. *Magnetic Resonance in Medicine*, 71:1151–1157, 2014.

Sung YH, Lee J, Nam J et al (2018) Differential Involvement of Nigral Subregions in Idiopathic Parkinson’s Disease Young Hee Sung Human Brain Mapping 39:542–553 *Hum Brain Mapp* Jan;39(1):542-553.doi: [10.1002/hbm.23863](https://doi.org/10.1002/hbm.23863).

Tan H, Zhang L, Mikati AG, et al. Quantitative Susceptibility Mapping in Cerebral Cavernous Malformations: Clinical Correlations. *AJNR American journal of neuroradiology*. 2016; 37(7): 1209–1215
doi: [10.3174/ajnr.A4724](https://doi.org/10.3174/ajnr.A4724)

Thompson KJ, Shoham S, Connor JR (2001) Iron and neurodegenerative disorders. *Brain Res Bull* 55:155–164. [https://doi.org/10.1016/s0361-9230\(01\)00510-x](https://doi.org/10.1016/s0361-9230(01)00510-x)

Thomsen MS, Andersen MV, Christoffersen PR et al (2015) Neurodegeneration with inflammation is accompanied by accumulation of iron

and ferritin in microglia and neurons. *Neurobiol Dis* 81:108–118. <https://doi.org/10.1016/j.nbd.2015.03.013>

Tong K.A, K.W. Yeom, and S. Kuzminski. Susceptibility-Weighted Imaging and Quantitative Susceptibility Mapping in the Brain. *Journal of Magnetic Resonance Imaging*, 42:23–41, 2015.

Treaba CA, Balasa R, Podeanu DM, Simu IP, Buruian MM (2014) Cerebral lesions of multiple sclerosis: is gadolinium always irreplaceable in assessing lesion activity? *Diagn. Interv. Radiol.* 2014; 20: 178–184. doi: [10.5152/dir.2013.13313](https://doi.org/10.5152/dir.2013.13313)

Uitti RJ, Rajput AH, Rozdilsky B et al (1989) Regional metal concentrations in Parkinson's disease, other chronic neurological diseases, and control brains. *Can J Neurol Sci* 16:310–314. <https://doi.org/10.1017/s0317167100029140>
Valencia Garcia, S., Brischoux, F., Clement, O., et al., 2018. Ventromedial medulla inhibitory neuron inactivation induces REM sleep without atonia and REM sleep behavior disorder. *Nat. Commun.* 9, 504

Vega RA, Holloway KL, Larson PS. (2014) Image-guided deep brain stimulation. *Neurosurg. Clin. N. Am.*; 25: 159–172
DOI: [10.1016/j.nec.2013.08.008](https://doi.org/10.1016/j.nec.2013.08.008)

Von Lewinski F, Werner C, Jörn T, Mohr A, Sixel-Döring F, Trenkwalder C et al (2007) T2*-weighted MRI in diagnosis of multiple system atrophy. *J Neurol* 254:1184–1188

W. Lu, B. Wu, and C. Liu. Quantitative susceptibility mapping of human brain reflects spatial variations in tissue composition. *Neuroimage*, 59:2625–2635, 2012.

Wahlund Lo, Barkhof F, Fazekas F et. al (2001) A new rating scale for age-related white matter changes applicable to MRI and CT *Stroke Jun*;32(6):1318-22 doi: [10.1161/01.str.32.6.1318](https://doi.org/10.1161/01.str.32.6.1318).

D O Walsh¹, A F Gmitro, M W Marcellin

Walsh DO, Gmitro AF Marcellin MW (2000) Adaptive reconstruction of phased array MR imagery *Magn Reson Med May*;43(5):682-90. doi: [10.1002/\(sici\)1522-2594\(200005\)43:5](https://doi.org/10.1002/(sici)1522-2594(200005)43:5)

Wang S, Lou M, Liu T, Cui D, Chen X, Wang Y (2013) Hematoma volume measurement in gradient echo MRI using quantitative susceptibility mapping. *Stroke*; 44(8):2315–2317. doi: [10.1161/STROKEAHA.113.001638](https://doi.org/10.1161/STROKEAHA.113.001638)

Wang Y, Butros SC, Shuai X, et al (2012). Different iron-deposition patterns of multiple system atrophy with predominant parkinsonism and idiopathic Parkinson diseases demonstrated by phase-corrected susceptibility-weighted imaging. *AJNR Am J Neuroradiol*;33:266–73 doi: [10.3174/ajnr.A2765](https://doi.org/10.3174/ajnr.A2765)

Wang Y. and Liu T. (2015) Quantitative Susceptibility Mapping (QSM): Decoding MRI Data for a Tissue Magnetic Biomarker. *Magnetic Resonance in Medicine*, 73:82–101. doi: [10.1002/mrm.25358](https://doi.org/10.1002/mrm.25358)

Wang Yi, et al (2017) Clinical Quantitative Susceptibility Mapping (QSM) – Biometal Imaging and its Emerging Roles in Patient Care *J Magn Reson Imaging*. 2017 October ; 46(4): 951–971. doi:10.1002/jmri.25693

Ward RJ, Zucca FA, Duyn JH et al (2014) The role of iron in brain ageing and neurodegenerative disorders. *The Lancet Neurology* 13:1045–1060. [https://doi.org/10.1016/S1474-4422\(14\)70117-6](https://doi.org/10.1016/S1474-4422(14)70117-6)

Wardlaw JM, Brindle W, Casado AM, et al (2012) A systematic review of the utility of 1.5 versus 3 Tesla magnetic resonance brain imaging in clinical practice and research. *Eur Radiol*;22:2295–303+

Weber, F., Chung, S., Beier, K.T., Xu, M., Luo, L., Dan, Y., 2015. Control of REM sleep by ventral medulla GABAergic neurons. *Nature* 526, 435–438.

Wehrli FW, Fan AP, Rodgers ZB, Englund EK, Langham MC. Susceptibility-based time-resolved whole-organ and regional tissue oximetry. *Am. J. Neuroradiol*. 2016. doi: [10.1002/nbm.3495](https://doi.org/10.1002/nbm.3495)

Wei H, Dibb R, Zhou Y, et al. (2015) Streaking artifact reduction for quantitative susceptibility mapping of sources with large dynamic range. *NMR Biomed*. 2015; 28(10):1294–1303. doi: [10.1002/nbm.3383](https://doi.org/10.1002/nbm.3383)

Wilms H, Rosenstiel P, Sievers J et al (2003) Activation of microglia by human neuromelanin is NF-kappaB dependent and involves p38 mitogen-activated protein kinase: implications for Parkinson's disease. *FASEB J* 17:500–502. <https://doi.org/10.1096/fj.02-0314fje>

Wisnieff C, Ramanan S, Olesik J, Gauthier S, Wang Y, Pitt D (2015) Quantitative susceptibility mapping (QSM) of white matter multiple sclerosis lesions: interpreting positive susceptibility and the presence of iron. *Magn. Reson. Med*; 74: 564–570. DOI: [10.1002/mrm.25420](https://doi.org/10.1002/mrm.25420)

Wu B, Pei X, Li ZY. (2014) How does calcification influence plaque vulnerability? Insights from fatigue analysis. *Scientific World Journal*; 2014:417324. doi: [10.1155/2014/417324](https://doi.org/10.1155/2014/417324)

Wurzinger B, König P (2016) Eisenmangel, Müdigkeit und Restless- Legs- Syndrom (Iron deficiency, Fatigue and Restless-Legs-Syndrome) Wien Med Wochenschr 166:447–452. <https://doi.org/10.1007/s10354-016-0497-3>.

Xu B, Liu T et al (2014) **Flow compensated quantitative susceptibility mapping for venous oxygenation imaging**. Magn Reson Med. 2014 Aug;72(2):438-45. doi: 10.1002/mrm.24937. Epub 2013 Sep 4. PMID: 24006187

Wang Yi, et al (2017) Clinical Quantitative Susceptibility Mapping (QSM) – Biometal Imaging and its Emerging Roles in Patient Care J Magn Reson Imaging. October ; 46(4): 951–971. doi:10.1002/jmri.25693

Zecca L, Stroppolo A, Gatti A et al (2004) The role of iron and copper molecules in the neuronal vulnerability of locus coeruleus and substantia nigra during aging. Proc Natl Acad Sci U S A 101:9843–9848. <https://doi.org/10.1073/pnas.0403495101>

Zecca L, Zucca FA, Costi P et al (2003) The neuromelanin of human substantia nigra: structure, synthesis and molecular behaviour. J Neural Transm Suppl 20:145–155. https://doi.org/10.1007/978-3-7091-0643-3_8

Zhang Y, Ren R, Sanford Ld et al. (2020) Sleep in Parkinson's disease: A systematic review and meta-analysis of polysomnographic findings. Sleep Med Rev Jun;51:101281. doi: 10.1016/j.smrv.2020.101281.

Zhang W, Phillips K, Wielgus AR et al (2011) Neuromelanin activates microglia and induces degeneration of dopaminergic neurons: implications for progression of Parkinson's disease. Neurotox Res 19:63–72. <https://doi.org/10.1007/s12640-009-9140-z>

Zhang X, Surguladze N, Slagle-Webb B et al (2006) Cellular iron status influences the functional relationship between microglia and oligodendrocytes. Glia 54:795–804. <https://doi.org/10.1002/glia.20416>

Zhang Y, Gauthier SA, Gupta A, Chen W, Comunale J, Chiang GC, Zhou D, Askin G,

Zhu W, Pitt D, Wang Y. (2016) Quantitative susceptibility mapping and R2* measured changes during white matter lesion development in multiple sclerosis: myelin breakdown, myelin debris degradation and removal, and iron

accumulation. Am. J. Neuroradiol.; 37(9): 1629–1635. DOI: [10.3174/ajnr.A4825](https://doi.org/10.3174/ajnr.A4825)

Zhang Y, Gauthier SA, Gupta A, Comunale J, Chia-Yi Chiang G, Zhou D, Chen W, Giambone AE,

Zhu W, Wang Y (2016) .Longitudinal change in magnetic susceptibility of new enhanced multiple sclerosis (MS) lesions measured on serial quantitative susceptibility mapping (QSM).J Magn Reson Imaging.

2016 Aug;44(2):426-32.

doi: [10.1002/jmri.25144](https://doi.org/10.1002/jmri.25144).

Zhou D, Liu T, P. Spincemille, and Y. Wang (2014) Background field removal by solving Laplacian

boundary value problem. NMR in Biomedicine, 27:312–319.

doi: [10.1002/nbm.3064](https://doi.org/10.1002/nbm.3064)

Zucca FA, Segura-Aguilar J, Ferrari E et al (2017) Interactions of iron, dopamine and neuromelanin pathways in brain aging and Parkinson's disease. Prog Neurobiol 155:96–119. <https://doi.org/10.1016/j.pneurobio.2015.09.012>